Polarimetric Feature Analysis of Multi-Class Vehicles Using PARSAX Full Polarimetric FMCW Radar Data

MSc Thesis

Qing Zhang

Delft University of Technology

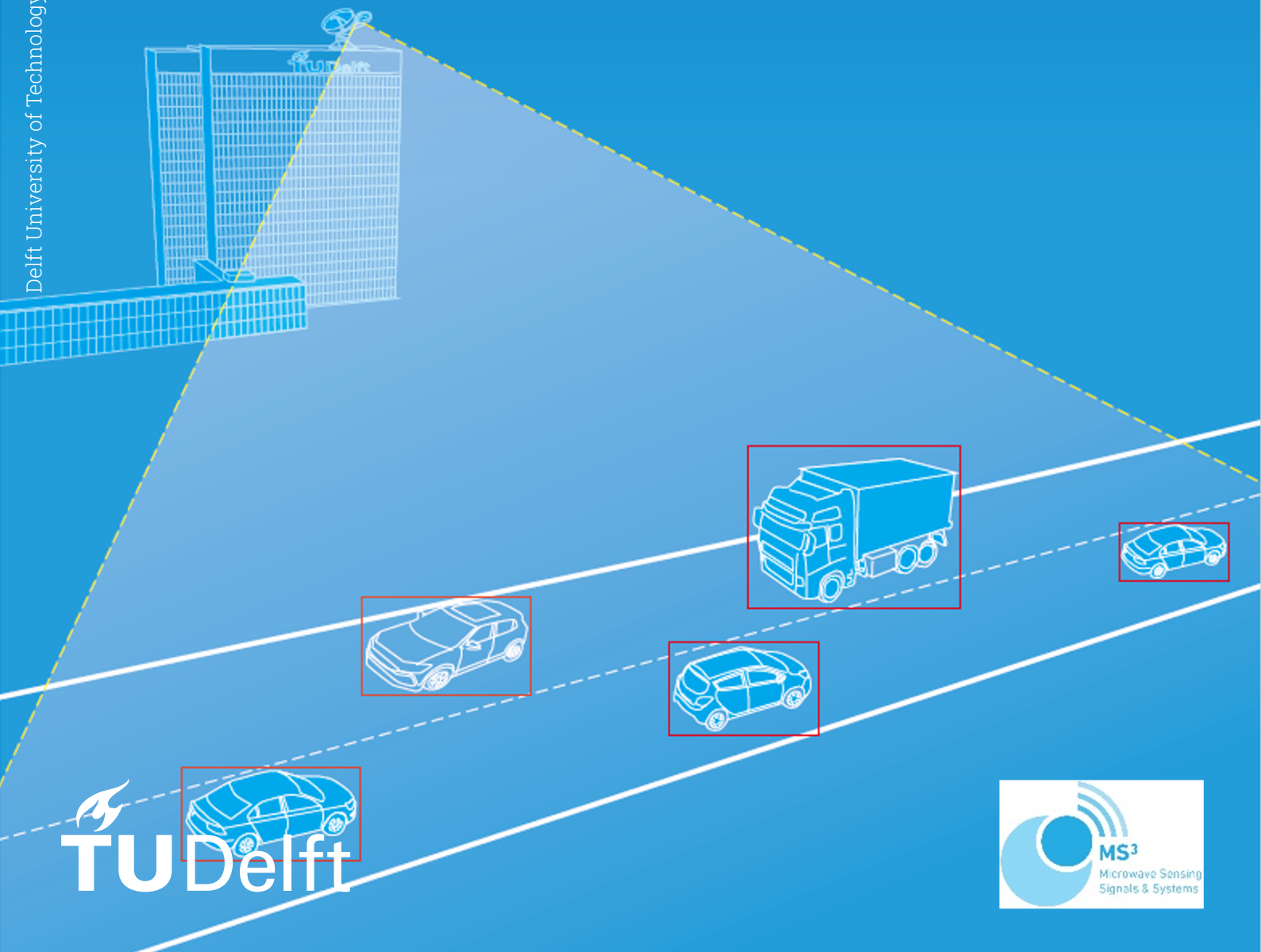

TU Delft

MS³ Microwave Sensing Signals & Systems

Polarimetric Feature Analysis of Multi-Class Vehicles Using PARSAX Full Polarimetric FMCW Radar Data

MSc Thesis

by

Qing Zhang

to obtain the degree of Master of Science
at the Delft University of Technology,
to be defended publicly on Tuesday August 22, 2023 at 13:00 PM.

Student number:	5402700	
Project duration:	November 21, 2022 – August 22, 2023	
Thesis committee:	Dr. O. A. Krasnov,	TU Delft, supervisor
	Prof. dr. A. Yarovoy,	TU Delft
	Dr. ir. J. Dauwels,	TU Delft

This thesis is confidential and cannot be made public until December 31, 2024.

Cover: Measurements of multi-class vehicles on a street-way by the PARSAX full polarimetric FMCW radar

An electronic version of this thesis is available at `http://repository.tudelft.nl/`.

TU Delft

Abstract

Nowadays, accurate vehicle classification plays a critical role in Advanced Driver Assistant Systems (ADASs), autonomous driving systems, and traffic monitoring systems. The benefits of utilizing additional polarimetric information in road target classification have been revealed in the literature. This thesis investigates the polarimetric characteristics of multi-class vehicles and explores new features contributing to vehicle classification, using a labeled street-way database extracted from the PARSAX S-band polarimetric Frequency Modulated Continuous Wave (FMCW) radar. The vehicle classes involved in this thesis are sedan, sedan with extended luggage bin, mini-van, small truck, and large truck.

Three calibration algorithms are proposed and validated for calibrating the labeled street-way database to ensure feature quality. The first channel calibration algorithm removes the channel-specific amplification factors and biases due to the non-ideal and non-identical electronic devices in the four polarimetric channels of the PARSAX radar. The second phase compensation algorithm compensates the phase difference between the H- and V-polarized channels, which is caused by the time shift between the transmitted H- and V-polarized signals. The last antenna pattern compensation algorithm resolves the power degradation in the measurements due to the PARSAX radar beam width limitation.

Based on the calibrated labeled street-way database, multiple polarimetric features are extracted from the Polarization Scattering Matrices (PSMs), coherency and covariance matrices using the eigenvalues/eigenvectors decomposition methods. These matrices represent either the central bodies or the whole bodies of the vehicles. In each case, the eigenvalues and eigenvectors are analyzed to indicate the vehicles' reflection amplitudes/power and polarization basis. Furthermore, these features are evaluated, and most of the amplitudes/power-based features show great classification capabilities. However, all vehicles have a similar polarization basis, which does not have a contribution to vehicle classification. In addition, the target length and eigenvalues of the covariance matrix of detection cells are also extracted as potential features. The feature evaluation results show that the target length and the first eigenvalue of the covariance matrix of detection cells have classification capabilities, while the second eigenvalue does not contribute to vehicle classification.

Preface

The past nine-month thesis was really meaningful and unforgettable to me. I have gained a lot of new knowledge and skills during this process, and I have gained a deeper understanding of the whole picture of radar polarimetry. Although the research work was full of challenges, I enjoyed it and was so happy that I could consolidate my knowledge when seeking solutions.

Hereby, I would like to show my great gratitude to my supervisor, Dr. O.A. Krasnov. Thanks for always being so patient and supportive to guide me through the whole thesis and help me with any problems. I really benefited from the advice during the weekly meetings and all the small discussions. I do appreciate his encouragement during the whole process, not only in the thesis but also in my course studies. I feel so lucky that I could work on this project and achieve a lot of nice results together with him. I also would like to express my great appreciation to Prof. Dr. A. Yarovoy. Thanks for patiently helping me find a thesis that best fits me. Thanks for arranging many helpful seminars, so we could get to know other projects in the group and learn presentation skills. I did learn a lot from the last meeting on report writing skills. Finally, I would like to thank my families and friends. Every result I have achieved is inseparable from their support and encouragement.

Qing Zhang
Delft, August 2023

Contents

Abbreviations

Abbreviations

Abbreviation	Definition
ADAS(s)	Advanced Driver Assistant System(s)
ASC	Attributed Scattering Center
CA	Constant Acceleration
DAC(s)	Digital to Analog Converter(s)
DBSCAN	Density-Based Spatial Clustering of Applications with Noise
EM	Electromagnetic
FFT	Fast Fourier Transform
FMCW	Frequency Modulated Continuous Wave
FPGA(s)	Field Programmable Gate Array(s)
GNN	Global Nearest Neighbor
HPF	High Pass Filter
LFM	Linear Frequency Modulated
MIMO	Multiple-Input Multiple-Output
MMW	Millimeter Wave
MTT	Multi-Target Tracking
OS-CFAR	Ordered Statistics-Constant False Alarm Rate
PCM	Pulse-code Modulation
PMSD	Polarimetric Maximization Synthesis Detector
PSM	Polarization Scattering Matrix
PSMs	Polarization Scattering Matrices
RCS	Radar Cross Section

1 Introduction

1.1. Motivation and Goals

Radar system plays a crucial role in Advanced Driver Assistant Systems (ADASs), benefiting from its accurate and instantaneous estimations of target range and relative radial velocity. Compared with other complementary sensing technologies, such as lidar and camera, radar can provide robust measurements even under extreme weather and light conditions. In the current ADASs, radar is used in adaptive cruise control, forward collision avoidance, lane-change assist, and evasion assist, significantly enhancing road safety and increasing driving convenience [1]. Leading by the rapid development in computation and communication technologies in recent years, autonomous driving is drawing intensive attention. To support and realize autonomous driving, utilizing radar systems to reliably detect and identify all surrounding targets in a complicated driving environment has become highly important [2, 3]. In addition, the same demand is required in traffic monitoring systems, where accurate vehicle classification is an important task [4].

The major researches focus on classification methods based on feature extraction of the road targets using the automotive Millimeter Wave (MMW) radar. Some commonly used features in this field are point cloud, range-Doppler, Radar Cross Section (RCS), and micro-Doppler features [4]. Furthermore, with the newly available automotive polarimetric radar, more research is concentrated on the distribution of the target's polarimetric information in the road target classification. The polarimetric information describes the orientations of the Electromagnetic (EM) waves that interact with the targets. Compared with conventional linear polarized automotive radar, automotive polarimetric radar could capture additional information on the shapes and orientations of the targets, which has the capability to improve classification performance [5]. Thus, analyzing the polarimetric characteristics of different sub-classes of vehicles and exploring more polarimetric features have become essential research directions in road user classification, which are exactly the main topics in this project.

In this project, to support the vehicles' polarimetric information analysis and feature exploration, the TU Delft's PARSAX radar will be used to provide real-world measurements, as shown in Figure 1.1. The PARSAX radar is an S-band high-resolution Doppler polarimetric Frequency Modulated Continuous Wave (FMCW) radar, which measures all four elements of the Polarization Scattering Matrix (PSM) during one sweep, indicating amplitude, phase, and polarimetric information of the targets [6]. As shown in Figure 1.2, the PARSAX radar measures vehicles driving on Highway A13, providing the data sets to be processed and analyzed. To realize the feature extraction from the highway vehicles, a signal and data processing chain has been developed in [7], in which a non-labeled feature database has been established, and the $H/A/\alpha$ decomposition-based features are found to be especially informative in distinguishing moving vehicles and static clutters even if their velocities are unknown. However, due to a lack of labels, proceeding with the polarimetric characteristics analysis of different classes of vehicles is infeasible, and no feature has been found to help vehicle classification yet.

Figure 1.1: PARSAX full polarimetric S-band FMCW radar [7]

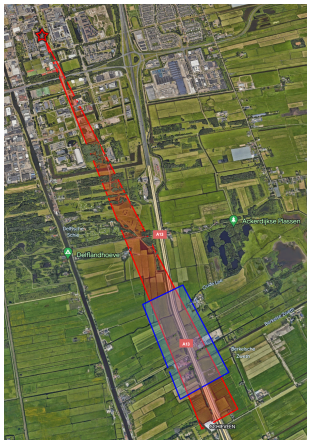

Figure 1.2: Measuring highway vehicles on A13 using PARSAX radar

To deal with the problem that highway vehicles cannot be labeled due to the dense traffic, and the extracted features cannot be interpreted, another measuring scenario is proposed. The PARSAX radar measures vehicles driving on the street-way (Schoemakerstraat), as shown in Figure 1.3, where the sequentially observed vehicles can be labeled using parallel video records. Figure 1.4 gives one of the frames of the parallel video records, showing that the classes of vehicles are visible. The processing and labeling of the street-way measurements have been done in [8]. This thesis will mainly focus on vehicle polarimetric characteristics analysis and feature exploration using the labeled street-way database.

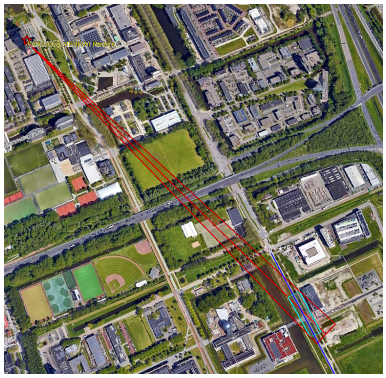

Figure 1.3: Measuring street-way vehicles on Schoemakerstraat using PARSAX radar

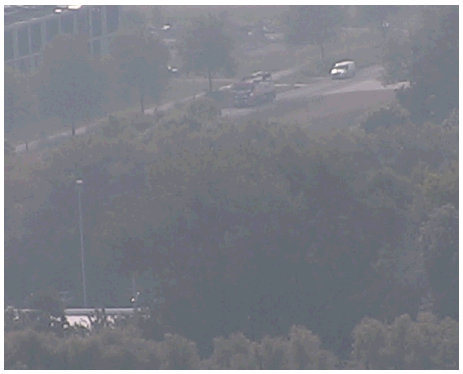

Figure 1.4: One of the frames in the parallel video records

Based on the introduced research interests and the previous work in this project, the main goal of this thesis is to analyze the polarimetric characteristics of multi-class vehicles and explore more features that could contribute to vehicle classification, using the labeled street-way database extracted from the real-world measurements of the PARSAX radar. The main goal can be decomposed into the following sub-goals:

1. To calibrate the labeled street-way database to ensure the feature quality.
2. To extract new features from the calibrated labeled street-way database.
3. To investigate the polarimetric characteristics of the multi-class vehicles from the features.
4. To analyze the contributions of the extended new features in the vehicle classification.

1.2. Research Problem Definition

As previously introduced in Section 1.1, the features derived in the previous work of this project do not perform well in defining the sub-classes of the vehicles [7]. To continue the feature exploration,

calibration algorithms are required on the labeled street-way database to guarantee the feature quality. Three issues need to be taken into account. The first one is the channel-specific amplification factor and bias caused by the non-ideal and non-identical characteristics of electronic devices in the four polarimetric channels. The second problem is caused by the time shift between the transmitted H- and V-polarized signals, which leads to a phase difference between the H- and V-polarized channels when measuring moving targets. The close observation range of the street-way vehicles causes the third problem. The azimuth angle range of the observed area is larger than the PARSAX antenna beam width, which leads to power degradation in the measurements. The proposed calibration algorithms should be able to deal with all these problems caused by the PARSAX radar's hardware characteristics and measurement settings.

After calibrating the database, different polarimetric decomposition methods could be applied to the calibrated database to explore new polarimetric features. The previously used polarimetric decomposition methods in this project are mainly focused on coherent decomposition methods (e.g., Pauli decomposition and Krogager decomposition), which do not lead to satisfactory results [7]. Thus this thesis will focus on more essential polarimetric decomposition methods (i.e., eigenvalues/eigenvectors decomposition methods).

Additionally, more features unrelated to the polarimetric information can also be extracted and evaluated (e.g., vehicle's length).

In summary, the research problem can be defined as several sub-problems:

1. What calibration algorithms can be developed to deal with the problems caused by the PARSAX radar's hardware characteristics and measurement settings?
2. What polarimetric features can be extended using the eigenvalues/eigenvectors decomposition methods?
3. What are the polarimetric characteristics of the multi-class vehicles indicated by the extracted polarimetric features?
4. What other features, unrelated to the target polarimetric information, can contribute to vehicle classification?
5. What are the classification performances of the extended new features?

1.3. Overview of State-of-the-Art

In recent decades, much research has indicated the possibilities and benefits of using polarimetric radars in vehicle classification. This section will give an overview of the state-of-the-art, starting with an introduction to the increasing applications of full polarimetric radars in driving systems. Then the research on the polarimetric features of different types of vehicles will be summarized. The progress in measuring RCS will be presented first, which is one of the commonly used features. Then the features related to PSM decomposition methods will be elaborated, where the main idea is to interpret different vehicle segments as simple scattering mechanisms. Finally, the potential capability of the eigenvalues/eigenvectors decomposition methods in vehicle classification will be demonstrated by reviewing the related feature applications in other fields.

Since the 1990s, due to the decreasing prices of MMW components and the incredible ability of MMW radars to detect obstacles under extreme weather conditions and poor visibility, the MMW radar has become a popular sensor solution in driver assistance systems, intelligent cruise control systems, and collision avoidance systems. Regarding the additional polarization state information of EM waves provided by polarimetric radars, researchers and engineers in car manufacturers have made great efforts on applying full polarimetric MMW radars to improve system performance. Measurements and experiments with a full polarimetric MMW radar operating at 77 GHz were investigated in real road traffic environments to validate the automatic interpretation of the perceived data, which indicates the possibility of using polarimetric radar in vehicle classification [9].

In the past ten years, more research on the polarimetric features of different types of vehicles has been carried out. One of the main research topics is the polarimetric RCS measurements of different types of vehicles, which aims to enhance vehicle model simulations in automotive radar system developments. In [10], the RCS values of different automotive targets (bike, scooter, compact class car, estate wagon, van) are measured in the frequency range of 23–27 GHz in an anechoic chamber. For every measured object, a monostatic 180° azimuth scan is performed from the front to the rear of

the object. The measurement results indicate that the reflections of co-polarized (HH and VV) configurations are higher than the cross-polarized (HV and VH) ones. The bicycle's and the scooter's RCS of HH-polarization is higher than that of VV-polarization. In addition, measured four-wheeled vehicles with comparable sizes (a VW Golf V, an Audi A4 estate, a VW Beatle, and a Fiat Ducato van) have similar RCS values. Similar RCS measurements of a sedan, truck, and van are performed in [11]. The vehicles are also measured in an anechoic chamber, with a wider measuring frequency from 22 to 29 GHz. Then the measurements are further extended with a frequency range from 76 to 81 GHz in [12], and a pedestrian, motorcycle, and bicycle are added as targets. Moreover, [13] provides the polarimetric RCS measurements of four types of two-wheeled vehicles (an off-road enduro motorcycle, a pedelec, a child bike, and a trekking bike), using a polarimetric Multiple-Input Multiple-Output (MIMO) FMCW radar operating at 77 GHz. The measurements are implemented in an anechoic chamber as well. In addition, it mentions that the RCS signatures provide the possibility to decompose the PSM into canonical scattering mechanisms, such as even-bounce, odd-bounce, and cross-polar scattering, which helps to achieve a robust vehicle classification.

This paragraph will further explain several examples of PSM decompositions to interpret different vehicle segments as simple scattering mechanisms. In [14], Saville et al. summarize the progress in linking the scattering behavior of a set of civilian vehicles (mainly categorized as sedan class and SUV class) to Attributed Scattering Center (ASC) models, which represent scattering mechanisms by singly reflecting (spheres, cylinders, plates, and edges) or retro-reflecting (dihedral, trihedral, and top hat) components. This work is based on a set of simulated X-band (8-12 GHz) scattering data for civilian vehicles. The simulation results indicate the obvious differences between the sedan and SUV classes. At a low elevation angle ($30°$), the sedan class is dominated by the scattering mechanisms of cylinders, horizontal edges, and horizontal dihedrals. However, the SUV class has the dominant scatterers of horizontal cylinders and horizontal edges. In the case of a high elevation angle ($60°$), the two classes have the same dominant scattering mechanisms. In addition, a Pauli basis decomposition is applied to the simulated data of a Toyota Camry to illustrate its potential physical scattering mechanisms. Using RGB color mapping, a 3D image is reconstructed as shown in Figure 1.5. The Pauli decomposition method interprets the different vehicle segments as dominant single bounce, double bounce, or cross-polar scattering mechanisms. Another widely known PSM decomposition method named Krogager decomposition is used in [15] to represent the underlying physical scattering mechanisms of a passenger car (an E-class W213 limousine). The polarimetric information is captured by a polarimetric FMCW MIMO radar at 77 GHz. The Krogager decomposition method decomposes PSM into three components, a sphere, a dipole, and a helix. Analyzing the decomposed simple scattering mechanisms reveals the possibilities of identifying different vehicle segments. The benefits of using polarimetric information to estimate the orientation and extent of vehicles in road traffic are also illustrated.

Figure 1.5: A reconstructed 3D image (in Pauli basis) of a Toyota Camry using RGB color mapping, interpreting different vehicle segments as simple mechanisms [14]

Although in literature, the eigenvalues/eigenvectors decomposition methods have not been applied in vehicle classification, they are widely used in other fields, especially in terrain classification, land use, soil moisture, and ground cover classification. The eigenvalue spectrum gains insight into scattering entropy, anisotropy, and span (i.e., total power). The eigenvectors can be evaluated for interpreting geophysical properties, segmenting and classifying ground cover and terrain types [16]. Another application of the eigenvalues/eigenvectors decomposition methods is the discrimination of spheroid pure targets in distributed targets by calculating entropy from the eigenvalues [17]. Apart from the classifica-

tion capability of random targets, the eigenvalues/eigenvectors decomposition methods also contribute to classifying distributed man-made targets. In [18], an orientation-invariant feature vector extracted using the eigenvalues/eigenvectors decomposition method is validated on two classification scenarios for man-made targets. The experimental data set in the first scenario is collected in an anechoic chamber, using a full polarimetric radar at 10 GHz to measure eight simple reflectors, including dihedrals, trihedrals, and flat planes. The second data set consists of polarimetric synthetic aperture images of eight ships acquired under 5.3 GHz in a real-world scenario. Classification results in both measurement scenarios demonstrate the ability of the proposed orientation-invariant feature vector to classify man-made objects.

All introduced related research in the state-of-the-art is summarized as follows in Table 1.1:

Table 1.1: Summary of the state-of-the-art

Reference	Author	Radar center frequency	Related work	Measuring scenario(s)
[9]	Wanielik et al.	77 GHz	Use polarimetric radar in real road traffic environments	Read-world scenario
[10]	Schipper et al.	23-27 GHz	RCS measurements of bike, scooter, compact class car, estate wagon, and van	Anechoic chamber
[11]	Geary et al.	22-29 GHz	RCS measurements of sedan, truck, and van	Anechoic chamber
[12]	Geary et al.	76-81 GHz	RCS measurements of sedan, truck, van, pedestrian, motorcycle, and bicycle	Anechoic chamber
[13]	Visentin et al.	77 GHz	RCS measurements of four types of two-wheeled vehicles	Anechoic chamber
[14]	Saville et al.	8-12 GHz	Interpreting different segments of a set of civilian vehicles as dominant simple scattering mechanisms	Air Force Research Laboratory civilian vehicle data dome
[15]	Tilly et al.	77 GHz	Interpreting different segments of a passenger car as dominant simple scattering mechanisms	Read-world scenario
[16]	Ainsworth et al.	4-8 GHz	Application of eigenvalues/eigenvectors decomposition methods in terrain classification, land use, soil moisture, and ground cover classification	Read-world scenario
[17]	Zakeri et al.	/	Application of eigenvalues/eigenvectors decomposition methods in discrimination of spheroid pure targets in distributed targets	Simulated data set
[18]	Paladini et al.	5.3 GHz and 10 GHz	Application of eigenvalues/eigenvectors decomposition methods in classifying man-made targets (simple reflectors and ships)	Anechoic chamber and real-world scenario

1.4. Research Novelty

According to the preceding thesis introduction and the state-of-the-art, this thesis incorporates numerous research novelties. First of all, the normally used radar in road traffic environment is automotive MMW radar, which has a commonly used operating frequency of 77 GHz. However, the center frequency of the PARSAX radar used in this project is only 3.315 GHz. The huge difference between the radar frequencies will significantly affect the vehicles' polarimetric characteristics. Instead of regarding the vehicles as extended targets, in this project, the vehicles are distributed targets with comparable sizes to the range resolution. The feature analysis results of different vehicle types in the state-of-the-art may not be adequate for the PARSAX radar data. In addition, the PARSAX radar's frequency is smaller than all of the frequencies in the state-of-the-art. Thus, a completely new sight of vehicles' polarimetric features can be accomplished in this thesis.

Secondly, this project proposes the idea of interpreting the features of different classes of vehicles using street-way measurements and parallel video records. The labeled street-way database includes more than 150 vehicles with varying velocities. For the literature that focuses on feature studies of different classes of vehicles, the data is normally measured in an anechoic chamber, and there is only one measuring target for each class. Although some of them use vehicles in real-world scenarios, the numbers of targets are still relatively small. The large number of targets in this thesis will lead to more convincing and general results. Additionally, compared with the static vehicles in the anechoic chamber, the vehicles with dynamic velocities could inspire interesting dynamic polarimetric information analysis in this thesis.

Thirdly, novel calibration algorithms will be proposed and implemented to guarantee the feature quality. As mentioned in the research problem definition in Section 1.2, the calibration algorithms are necessary for dealing with the three issues caused by the PARSAX radar's hardware characteristics and measurement settings.

Finally, to the best of the author's knowledge, no research has worked on the application of eigenvalues/eigenvectors decomposition methods in vehicle classification, although there are some applications in other fields. This is the first time investigating the contribution of polarimetric features extracted using eigenvalues/eigenvectors decomposition methods in vehicle classification.

1.5. Thesis Structure

This thesis focuses on investigating the polarimetric characteristics of multi-class vehicles and exploring features contributing to vehicle classification. The subsequent chapters are organized as follows: Chapter 2 introduces the basic principles of radar polarimetry and PARSAX radar as the whole background of this thesis. The creation of the labeled street-way database is also introduced, which is important for understanding further work in this thesis. Then in Chapter 3, three algorithms for calibrating the labeled street-way database to ensure feature quality are proposed, validated, and implemented. Subsequently, Chapter 4 presents the feature extractions and analysis to indicate the multi-class vehicles' polarimetric characteristics and figure out features contributing to vehicle classification. Finally, this thesis is concluded in Chapter 5. The results of this thesis are discussed, and recommendations are given as well.

2

Background and Related Work

This chapter introduces the background knowledge of radar polarimetry and previous work in this project. Firstly, the basic principles of radar polarimetry are elaborated through the definitions of EM wave polarization and PSM. The polarization responses of several canonical scattering mechanisms are presented. Then the PARSAX full polarimetric FMCW radar is introduced in detail, including its measuring principle, hardware design, and main characteristics. Finally, the creation of the labeled street-way database is presented. The algorithms used in the signal and data processing chain are generally introduced, and the defined vehicle classes in the database are explained.

2.1. Basic Principles of Radar Polarimetry

In a radar system, information on objects is obtained based on the interaction of EM waves with the objects. The information could be carried in the frequency, magnitude, and polarization of the EM waves [19]. The utilization of radar polarimetry has indicated that polarization states of EM waves provide additional information for improving target detection, identification, and parameter estimation [20]. In this section, firstly, the basic definition of EM wave polarization will be introduced. Then the concept of PSM will be elaborated, followed by the polarization response of several canonical scattering mechanisms.

2.1.1. Polarization of Electromagnetic Waves

As illustrated in Figure 2.1, an EM wave consists of a coupled, orthogonal electric field ($\overrightarrow{E}$) and magnetic field ($\overrightarrow{H}$), which oscillate perpendicular to the wave propagation direction (Z-direction). The polarization of the EM wave is defined as the oscillation direction of the electric field, which is the Y-direction in this figure. By using two orthogonal basis vectors, the electric field could be described as a two-dimensional complex vector:

$$\overrightarrow{E} = a_h e^{i\delta_h}\hat{h} + a_v e^{i\delta_v}\hat{v}, \tag{2.1}$$

where $\hat{h}$ denotes the horizontal basis vector, and $\hat{v}$ denotes the vertical one. Horizontal polarization refers to the state where the electric field is perpendicular to the plane of incidence. When the electric field is in the plane of incidence, the EM wave has vertical polarization. In addition, a_h, a_v, δ_h and δ_v in Equation (2.1) represent the amplitudes and relative phases respectively, which are all real numbers.

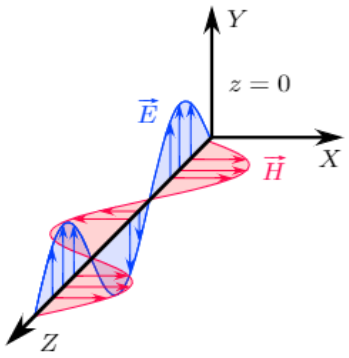

Figure 2.1: Transverse EM wave propagating in Z-direction with polarization in Y-direction [21]

In the general case, EM waves are elliptically polarized, which means the tip of the electric field is tracing an ellipse when the wave is propagating. The following expression of an ellipse is satisfied by the electric field:

$$(\frac{E_h}{a_h})^2 + (\frac{E_v}{a_v})^2 - 2\frac{E_h}{a_h}\frac{E_v}{a_v}cos(\delta_h - \delta_v) = sin^2(\delta_h - \delta_v), \tag{2.2}$$

with:

$$E_h = a_h cos\delta_h; \tag{2.3}$$

$$E_v = a_v cos\delta_v. \tag{2.4}$$

Figure 2.2 shows the graphical explanation of the polarization ellipse. The angles ψ ($0 \leq \psi \leq \pi$) and χ ($-\frac{\pi}{4} \leq \chi \leq \frac{\pi}{4}$) refer to the ellipse orientation angle and the ellipticity angle, which could characterize the ellipse. These two angles could be calculated as follows:

$$tan2\psi = \frac{2a_h a_v}{a_h^2 - a_v^2}cos(\delta_h - \delta_v); \tag{2.5}$$

$$sin2\chi = \frac{2a_h a_v}{a_h^2 + a_v^2}sin(\delta_h - \delta_v). \tag{2.6}$$

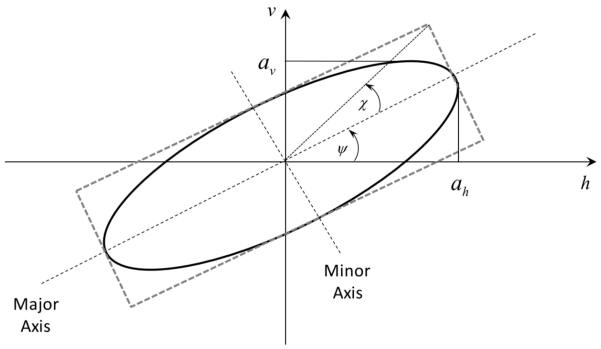

Figure 2.2: A EM wave polarization ellipse [19]

When tracing the ellipse, the tip of the electric field could rotate clockwise or counterclockwise. When the direction is clockwise, and the wave is viewed receding from the observer, the wave is defined to have a right-handed polarization. Similarly, the wave is said to have a left-handed polarization with a counterclockwise rotation direction.

The special cases are linear polarization and circular polarization. When the wave is linearly polarized, the phase difference $\delta_h - \delta_v = n\pi$, with n to be any integer, and the ellipse collapses to a line ($\psi = 0$). As for the circular polarization, the amplitudes a_h and a_v are equal, and $\delta_h - \delta_v = \pm\frac{\pi}{2}$. As a result, the ellipse becomes a circle.

In Equation 2.1, the amplitudes and phases are assumed to be constant. However, these parameters might vary with time, which leads to a partially polarized wave. Instead of a smooth ellipse, the tip of the electric field will trace a noisy version of the ellipse. Only part of the energy has a deterministic polarization state. In addition, another case is called randomly polarized/unpolarized wave, which indicates the wave radiated from some sources without any clearly defined polarization. The Sun is a typical example.

2.1.2. Polarization Scattering Matrix

When the incident electric field is scattered by an object, the polarization of the wave will be changed. The PSM describes how the object modifies the incident electric field vector. For the linearly polarized waves, the modification is described as:

$$\mathbf{E^{sc}} = \begin{bmatrix} S_{HH} & S_{HV} \\ S_{VH} & S_{VV} \end{bmatrix} \mathbf{E^{tr}} = [\mathbf{S}]\mathbf{E^{tr}}, \tag{2.7}$$

where $[\mathbf{S}]$ denotes the PSM, which is a 2×2 matrix involving complex elements. The subscripts of the elements in $[\mathbf{S}]$ represent the horizontal and vertical polarization of the transmitted and received signals. In addition, $\mathbf{E^{sc}}$ is the scattered electric field received by the antenna, and $\mathbf{E^{tr}}$ is the transmitted electric field vector. The bold symbols stand for matrix representations.

2.1.3. Polarization Responses of Canonical Scattering Mechanisms

It is always difficult to directly interpret the PSM of a real target due to its complex geometrical structure. However, a complex polarization response can be interpreted as a combination of polarization responses from simple scattering mechanisms. This subsection describes the PSMs and polarization responses of some elementary targets presenting canonical scattering mechanisms [19, 22].

Sphere, Flat Plate, Trihedral

The PSM of a sphere/plane/trihedral (Figure 2.3) in the Cartesian polarization basis $(\hat{h}, \hat{v})$ is given by:

$$\mathbf{S} = \begin{bmatrix} 1 & 0 \\ 0 & 1 \end{bmatrix}, \tag{2.8}$$

which indicates that there is no cross-polarization component ($S_{HV} = S_{VH} = 0$), and the co-polarization components are identical ($S_{HH} = S_{VV}$).

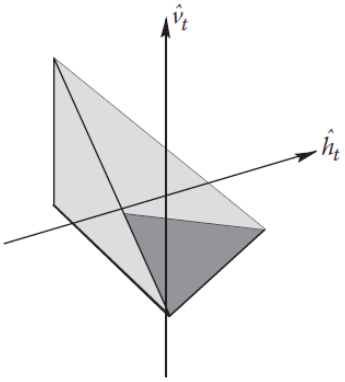

Figure 2.3: Trihedral [22]

The polarization response is visualized as a three-dimensional figure, and the transmitted and received polarizations are either the same (co-polarized response) or orthogonal (cross-polarized response). Figure 2.4 illustrates the co-polarized and cross-polarized responses of a sphere/plate/trihedral. It clearly shows that for the co-polarized response, the maximum power appears at $\chi = 0$

(linear polarizations), and the minimum power is found at $\chi = 45°$ (circular polarizations). While for the cross-polarized response, the locations of the maximum and minimum power are reversed.

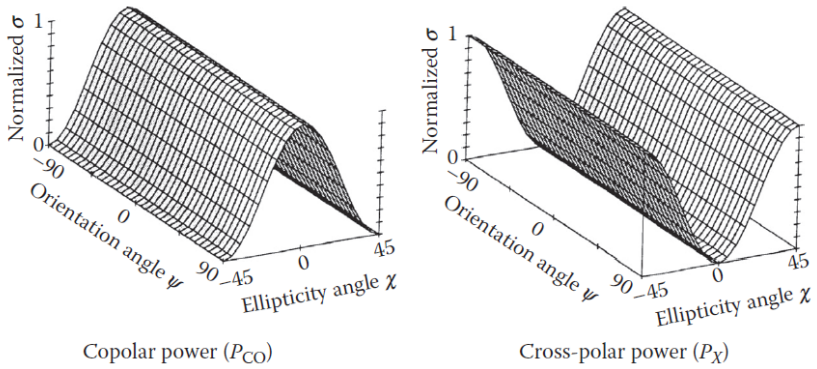

Figure 2.4: Co-polarized and cross-polarized response of a sphere/plate/trihedral [22]

Horizontal Dipole

The PSM of a horizontal dipole (Figure 2.5) in the Cartesian polarization basis $(\hat{h}, \hat{v})$ is given by:

$$\mathbf{S} = \begin{bmatrix} 1 & 0 \\ 0 & 0 \end{bmatrix}, \tag{2.9}$$

where only the horizontal co-polarized term is non-zero.

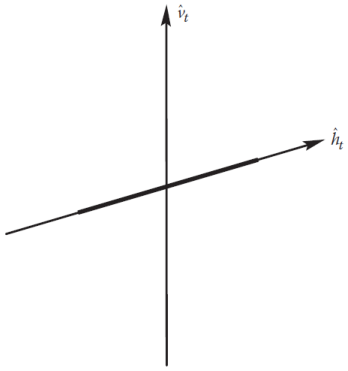

Figure 2.5: Horizontal dipole [22]

The corresponding polarization response is shown in Figure 2.6, where the maximum power only appears at HH-polarization.

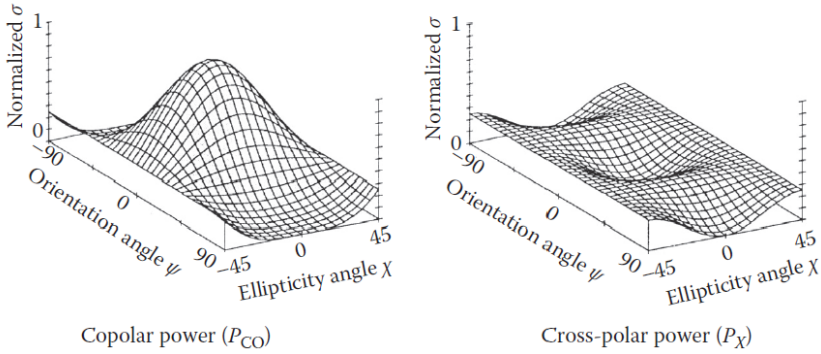

Figure 2.6: Co-polarized and cross-polarized response of a horizontal dipole [22]

Dihedral

The PSM of a horizontal dihedral (Figure 2.7) in the Cartesian polarization basis $(\hat{h}, \hat{v})$ is given by:

$$\mathbf{S} = \begin{bmatrix} 1 & 0 \\ 0 & -1 \end{bmatrix}, \tag{2.10}$$

which indicates that there is no cross-polarization component ($S_{HV} = S_{VH} = 0$), and the co-polarization components have the same amplitude and are out of phase ($S_{HH} = -S_{VV}$).

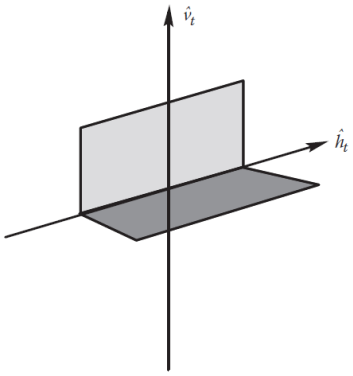

Figure 2.7: Dihedral [22]

The co-polarized and cross-polarized responses of a dihedral are presented in Figure 2.8. The minimum co-polarized power appears at $\psi = \pm 45°, \chi = 0$ ($\pm 45°$ oriented linear polarizations), and the maximum cross-polarized power is found at the same locations. Similarly, the maximum co-polarized and minimum cross-polarized power also have the same polarization.

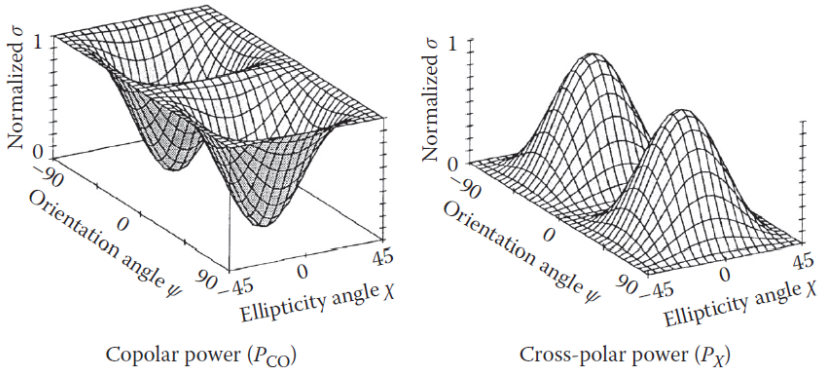

Figure 2.8: Co-polarized and cross-polarized response of a dihedral [22]

2.2. PARSAX Full Polarimetric FMCW Radar

This project uses TU Delft's PARSAX radar, which is an S-band high-resolution Doppler polarimetric FMCW radar [6]. It utilizes dual-orthogonal sounding signals, which measure all PSM elements simultaneously during one sweep. In Subsection 2.2.1, the measuring principle of PARSAX radar will be introduced in detail. Then the hardware design and main characteristics of PARSAX radar will be presented in Subsection 2.2.2.

2.2.1. Measuring Principle of PARSAX Radar

In radar systems with polarimetric capabilities, the non-simultaneous measurements of the PSM elements lead to serious limitations [20]. Instead of separating the two orthogonally polarized transmitted

signals in time or frequency as proposed in [23, 24, 6, 25], the PARSAX radar utilizes sounding signals with dual-orthogonality, which has been proposed in [26, 27, 20, 28]. The simultaneously transmitted H-polarized and V-polarized signals are orthogonal in both polarimetric and time-frequency spaces. The dual-orthogonality requires that the complex envelopes of the transmitted signals satisfy the following condition:

$$U = \int \dot{E}_{HT}(t) \cdot E^*_{VT}(t) \cdot dt \equiv 0. \tag{2.11}$$

A more strict condition needs to be satisfied for measuring the PSM of moving targets:

$$U(\tau, \omega_d) = \int \dot{E}_{iT}(t) \cdot \dot{E}^*_{jR}(t - \tau, \omega_d) \cdot dt \cong 0, \tag{2.12}$$

where $i,\ j = H,\ V$; $i \neq j$; τ is the time delay of the signal, which is related to the target's range; ω_d is the Doppler frequency shift.

The most widely used examples of such dual-orthogonal signals are: A pair of Linear Frequency Modulated (LFM) signals with positive and negative frequency slopes; A pair of LFM signals with the same frequency slope but delayed in time over an interval less than the sweep time; A pair of signals that are phase modulated by orthogonal codes [6].

By transmitting the dual-orthogonal signals, the non-simultaneous measurements of the PSM elements could be resolved. All elements are measured simultaneously and in the same frequency band.

2.2.2. PARSAX Radar Design and Main Characteristics

As elaborated in Subsection 2.2.1, the PARSAX radar developed at TU Delft is a full-polarimetric S-band radar, which is capable of simultaneously measuring all elements of the PSM of objects during one sweep. The dual-orthogonal sounding signals are generated digitally by 16-bit Digital to Analog Converters (DACs) with sampling frequencies up to 500 MHz [6]. The reception of the scattered signals has a high-dynamic range with advanced digital processing on intermediate frequency, which is supported by *Xilinx* Field Programmable Gate Arrays (FPGAs). The hardware design of the PARSAX radar provides real flexibility for generating different types of dual-orthogonal waveforms and implementing the corresponding processing algorithms.

Figure 2.9 presents the simplified block diagram of the PARSAX radar, which generally shows the hardware design. The main characteristics of the PARSAX radar are summarized in Table 2.1, where specific parameters are presented. More design details of the PARSAX radar can be found in [25, 29].

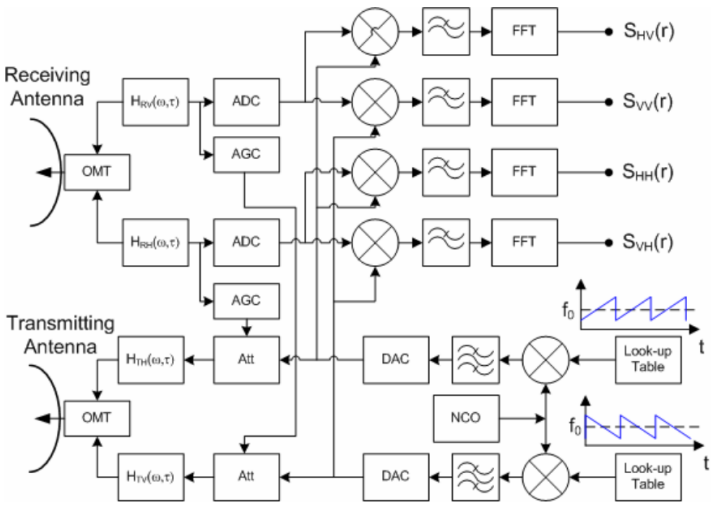

Figure 2.9: Simplified block-diagram of the PARSAX radar [6]

Table 2.1: Main characteristics of the PARSAX radar [6]

Components	Characteristics
S-band	Central frequency: 3.315 GHz Modulation bandwidth: 2 - 50 MHz Resolution: 75 - 3 m Sweep time: 1 ms
Antennas	Two parabolic reflectors Isolation receiver-transmitter: HH=-100 dB, VV=-85 dB
Receiver Antenna	Diameter: 2.12 m Beam width: 4.6° Gain: 32.8 dB
Transmitter Antenna	Diameter: 4.28 m Beam width: 1.8° Gain: 40.0 dB
Transmitter	Solid state power amplifiers 100 Watt max per channel 80 dB attenuators (8 bits control bus)
Receiver	Dynamic range: better 70 dB (spur-free dynamic range) 1 stage down conversion ADC at Intermediate Frequency (125 MHz, sampling 400 MHz, 14 bits) 4 channels FPGA-based digital processor
Waveforms	4-channel arbitrary waveform generator (sampling up to 1.2 GHz, 16 bits) Linear frequency modulation Pulse-code Modulation (PCM) with orthogonal codes

2.3. Labeled Street-Way Database Creation

The street-way database is created based on the signal and data processing chain proposed in [7], with the algorithms adjustments proposed in [8] to dedicate the signal and data processing chain for the street-way measurements. After establishing the database, the parallel video records are processed to label the database, resulting in six vehicle classes. In this section, the algorithms used in the signal and data processing chain will be generally introduced, and the defined six vehicle classes will be explained.

2.3.1. Signal and Data Processing Chain

The signal and data processing chain consists of four blocks: radar signal processing, target detection, target tracking, and target feature extraction, as shown in Figure 2.10.

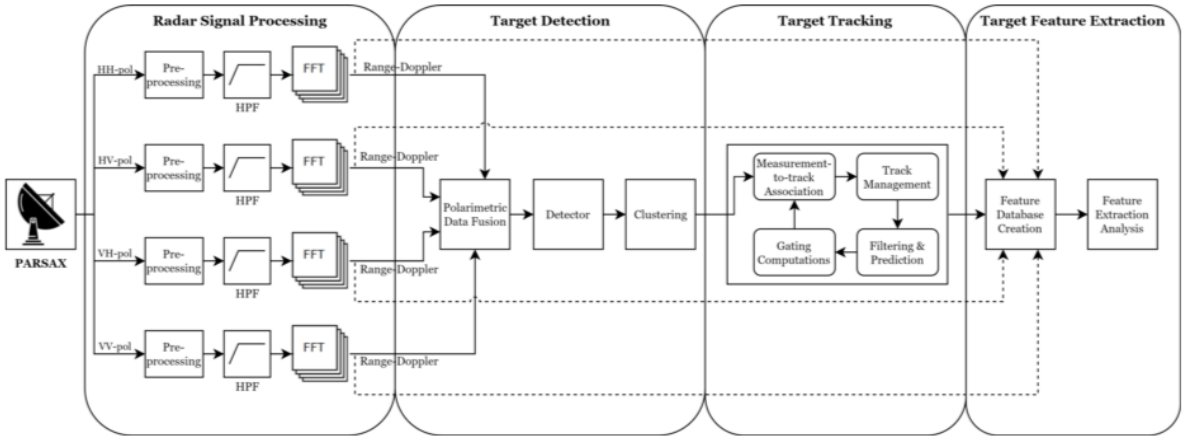

Figure 2.10: Signal and data processing chain for creating the labeled street-way database [7]

As indicated in the first block of Figure 2.10, the radar signal processing algorithms (Doppler processing) perform on the raw data to achieve range-Doppler maps from the four polarimetric channels. Firstly in the pre-processing of the raw data, a first Fast Fourier Transform (FFT) is applied to compute the range. Then a High Pass Filter (HPF) is used to filter out the static clutter and indicate only the moving targets in the filtered data. A 6th-order Butterworth-filter with a steeper slope is used as the HPF in this processing chain. After then, an 80 dB-Chebyshev window function is performed, followed by a second FFT. The window function aims to reduce the sidelobe levels and spectral leakage, and the second FFT computes the Doppler frequency (Doppler velocity).

Next, target detection algorithms are realized in the range-Doppler domain, as shown in the second block of Figure 2.10. Firstly, the four range-Doppler maps corresponding to the four PSM elements are integrated into a single range-Doppler map at each time frame, utilizing a data fusion method based on the Polarimetric Maximization Synthesis Detector (PMSD). Then an Ordered Statistics-Constant False Alarm Rate (OS-CFAR) detector is implemented to decide the target presence in each range-Doppler bin, resulting in a binary detection map at each time frame. A morphological filter then compensates for the imperfections and distortions of the binary detection maps. Besides, an additional HPF is applied to discard detection cells with low Doppler velocities. Subsequently, the Density-Based Spatial Clustering of Applications with Noise (DBSCAN) algorithm is implemented to group a set of detection cells as a single target. Furthermore, specifically for the street-way measurements, not only the central bodies of the vehicles are detected, but the micro-Doppler signatures also appear as clustered single targets. Thus the central bodies are further clustered with their micro-Doppler signatures. Figure 2.11 gives an example of the resulting detected vehicles in the range-Doppler domain. The red blocks indicate the boundaries of the clusters, and the black geometries inside the red blocks represent the clustered detection cells.

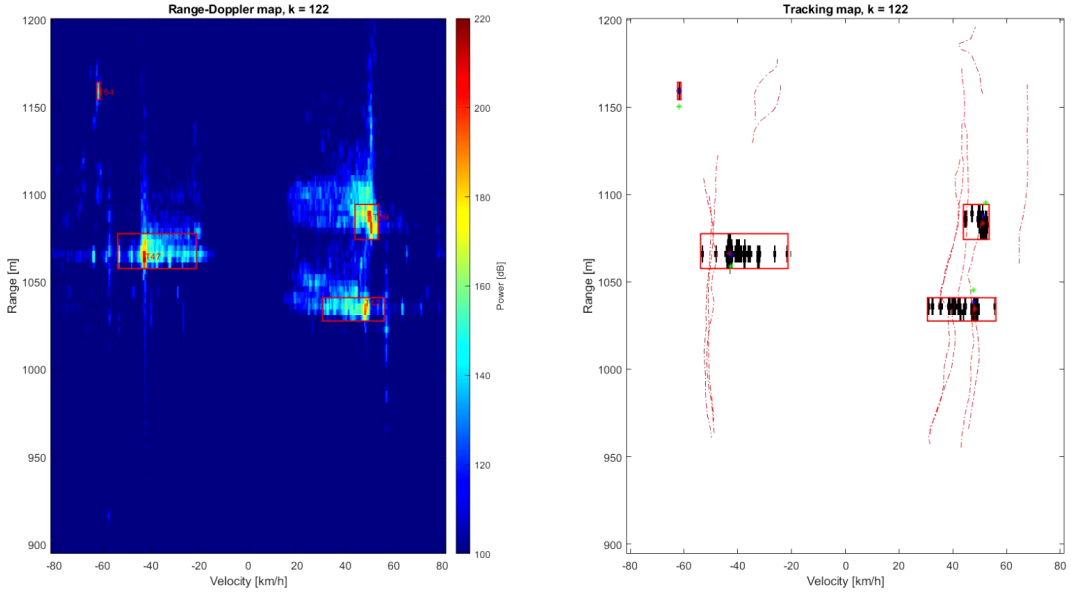

Figure 2.11: Range-Doppler map and tracking map at an example time frame [8]

The third block of the signal and data processing chain is to track multiple targets from frame to frame, applying a Multi-Target Tracking (MTT) algorithm. The classical Kalman filter is used to update and predict each cluster's state (range and velocity), applying the Constant Acceleration (CA) state dynamics model. To associate each cluster to a certain track, the Global Nearest Neighbor (GNN) method is implemented, with applying a hyperellipsoid gate to simplify the data association problem. For the track management problem, the M/N logic test method is implemented to initialize all unassigned clusters as new tracks and to delete all tracks that are not associated with any clusters. The red dash lines in Figure 2.11 indicate the resulting tracks at the example time frame. Each track represents the trajectory of one vehicle in the range-Doppler domain.

Finally, the target feature extraction is focused on extracting the PSMs of all time frames for each track. As presented in the target detection block, the range and Doppler indexes of the detection cells for

each cluster are known. Therefore, the elements of PSMs could be extracted from the range-Doppler maps of the four polarimetric channels. So far, a database including the PSMs of all vehicles over time frames has been achieved with undefined vehicle classes.

2.3.2. Database Labeling

The parallel video records are processed manually to assign the vehicles appearing in the videos to the tracks in the database. The vehicles are classified into six classes: sedan, sedan with extended luggage bin, sedan (with extended luggage bin), mini-van, small truck, and large truck, as shown in Figure 2.12. Note that the class of sedan (with extended luggage bin) stands for those sedans whose video records are not clear enough to define the possessions of extended luggage bins. Until now, a labeled street-way database has been achieved to support further analysis in this thesis.

(a) Sedan **(b)** Sedan with extended luggage bin **(c)** Sedan (with extended luggage bin)

(d) Mini-van **(e)** Small truck **(f)** Large truck

Figure 2.12: Six vehicle classes defined in the labeled street-way database

2.4. Summary

This chapter first introduces the basic principles of radar polarimetry, starting with elaborating on the polarization of EM waves. In a polarimetric radar system, the information of objects is not only carried in the frequency and magnitude but also in the polarization of EM waves. The EM wave polarization is defined as the oscillation direction of the electric field. The electric field could be described as a two-dimensional complex vector, using the orthogonal basis vectors $\hat{h}$ (horizontal basis vector) and $\hat{v}$ (vertical basis vector). In the general case, EM waves are elliptically polarized, which can be characterized by ellipse orientation and ellipticity angles. Special ellipticity angles $\psi = 0\ and\ 45°$ correspond to linear and circular polarizations, respectively. Afterward, the definition of PSM is presented. The PSM is a 2×2 matrix involving complex elements: S_{HH}, S_{HV}, S_{VH}, and S_{VV}, which describes how the object modifies the incident electric field vector. Furthermore, the polarization responses of some canonical scattering mechanisms (i.e., sphere, plane, trihedral, dipole, dihedral) are illustrated to interpret a complex PSM from a real target potentially.

Then the TU Delft's PARSAX radar is introduced in detail, including its measuring principle, hardware design, and main characteristics. The PARSAX radar is an S-band high-resolution Doppler polarimetric FMCW radar. It can transmit dual-orthogonal sounding signals to measure all elements of the PSM simultaneously during one sweep. The real flexibility the PARSAX radar provides to generate different types of dual-orthogonal waveforms and implement a high-dynamic signal reception range relies on the 16-bit DACs and Xilinx FPGAs. The main characteristics of the PARSAX radar are summarized from the perspectives of operating frequency, transmitter and receiver (antennas), and waveforms.

This chapter's last section focuses on the previous work on creating the labeled street-way database. The algorithms used in the signal and data processing chain to extract PSMs of the vehicles are generally introduced. The signal and data processing chain consists of four blocks: radar signal processing, target detection, target tracking, and target feature extraction. The first block performs Doppler pro-

cessing on the radar raw data to achieve range-Doppler maps of the four polarimetric channels. Then the four range-Doppler maps are fused to a single range-Doppler map in the second block to realize cell detection and clustering, and each cluster represents a target. In the third block, the clusters are associated with the tracks, which realizes the multi-target tracking over time frames. Finally, in the fourth block, the PSMs of all time frames for each track are extracted to form an unlabeled database. To label this database, the parallel video records are processed manually to assign the vehicles appearing in the videos to the tracks in the database. As a result, a labeled street-way database is achieved, with defined six classes of vehicles: sedan, sedan with extended luggage bin, sedan (with extended luggage bin), mini-van, small truck, and large truck.

3

Database Calibration Algorithms

The entire signal and data processing chain has been introduced in Subsection 2.3.1 for creating a database of the vehicles. However, according to the results in the previous work of this project, there is no informative feature being found that could contribute to vehicle classification [7]. To continue with the feature exploration, it is necessary to figure out database calibration algorithms that could improve the feature quality. In this chapter, three calibration algorithms are proposed and validated. The first is a channel calibration algorithm, which aims to remove the channel-specific amplification factor and bias caused by the non-ideal electronic devices in the four polarimetric channels. The second algorithm is a phase compensation algorithm, which deals with the phase difference of the polarimetric channels leading by a time shift between the transmitted H- and V-polarized signals. The last algorithm is an antenna pattern compensation algorithm, which resolves the power degradation due to antenna beam width limitation. All the algorithms will be demonstrated in detail in the following three sub-sections.

3.1. Channel Calibration

Considering the non-ideal and non-identical characteristics of the electronic devices in the four polarimetric channels of PARSAX radar, the measured output signals from the four channels have different amplification factors and biases. This project applies a noise-based polarimetric radar calibration algorithm proposed in [30] to calibrate the signals. In this section, the algorithm is introduced in detail first. Then the algorithm validation is presented. Finally, the integration of the algorithm in the signal and data processing chain is demonstrated.

3.1.1. Noise-Based Polarimetric Radar Calibration Algorithm

For the introduced PARSAX full polarimetric FMCW radar, the polarimetric signal at the output of each receiver channel can be formulated as follows:

$$y_{i,j}(r,t) = x_{i,j}(r,t) + n_{i,j}(r,t), \tag{3.1}$$

where $x_{i,j}(r,t)$ is the time- and range-dependent complex scattered signal, and $n_{i,j}(r,t)$ is the complex white Gaussian noise with zero mean and variance of σ_0^2 [30]. The indexes $i,\ j$ refer to the transmitted and received polarizations (H or V), respectively.

However, considering the independence of the four receiver channels, in which the electronic devices have non-ideal and non-identical characteristics, each channel has a specific amplification factor and a bias on the received polarimetric signal $y_{i,j}(r,t)$. Thus, the physically measured output signal at each receiver channel turns into the following:

$$V_{i,j}(r,t) = a_{i,j}(r) \cdot y_{i,j}(r,t) + b_{i,j}(r), \tag{3.2}$$

where $a_{i,j}(r)$ is the channel-specific amplification factor, and $b_{i,j}(r)$ is the channel-specific bias. Both parameters are considered to be only range-related in a short-term measurement.

To calibrate the signals in the four channels to achieve the true received polarimetric signal $y_{i,j}(r,t)$, the channel-specific $a_{i,j}(r)$ and $b_{i,j}(r)$ need to be estimated, which can be realized by utilizing the mean and variance specifications of white Gaussian noise. The noise signals can be measured by blanking the transmitters' power amplifiers. The noise signal at the output of each receiver channel is:

$$N_{i,j}(r,t) = a_{i,j}(r) \cdot n_{i,j}(r,t) + b_{i,j}(r). \tag{3.3}$$

Then according to the white Gaussian noise characteristics:

$$mean(n_{i,j}(r,t)) = 0; \tag{3.4}$$

$$var(n_{i,j}(r,t)) = \sigma_0^2, \tag{3.5}$$

the following formulas are satisfied, in which $a_{i,j}(r)$ and $b_{i,j}(r)$ can be estimated:

$$mean(N_{i,j}(r,t)) = b_{i,j}(r); \tag{3.6}$$

$$var(N_{i,j}(r,t)) = (a_{i,j}(r))^2 \cdot \sigma_0^2. \tag{3.7}$$

Utilizing the estimated $a_{i,j}(r)$ and $b_{i,j}(r)$, the signals at the four receiver channels could be calibrated as:

$$\begin{aligned} y\prime_{i,j}(r,t) &= \frac{V_{i,j}(r,t) - mean(N_{i,j}(r,t))}{\sqrt{var(N_{i,j}(r,t))}} \\ &= \frac{y_{i,j}(r,t)}{\sqrt{\sigma_0^2}} \\ &= \frac{x_{i,j}(r,t) + n_{i,j}(r,t)}{\sqrt{\sigma_0^2}}. \end{aligned} \tag{3.8}$$

3.1.2. Algorithm Validation

The proposed noise-based polarimetric radar calibration algorithm needs to be validated before being applied to the signal calibration. Considering all radar channels are physically located in the same environment, with the same electronic design and system temperature, the calibrated noise signals in all channels should be the same [30]. So the algorithm can be performed on the noise data to validate its feasibility.

For each channel, the noise data is calibrated according to Equation 3.8. Figure 3.1 presents the histograms of the non-calibrated and calibrated noise signals (real part) from the four polarimetric channels. Comparing the non-calibrated noise signals from the different channels in Sub-figure 3.1(a), the x-axes indicate that the noise signals have varying distribution ranges in the four channels, resulting from the channel-specific amplification factors. However, the bias is not obvious in the different channels. Then with the calibration algorithm, the calibrated noise signals of the four channels have the same distribution ranges, as shown in Sub-figure 3.1(b), indicating that the channel-specific amplification factors are removed. The same results could be observed from the imaginary parts of the noise signals. The histograms of the non-calibrated and calibrated noise signals (imaginary part) from the four polarimetric channels can be found in Appendix A.1.

To further validate the performance of the calibration algorithm, the covariance matrices of the non-calibrated and calibrated noise signals are calculated as C_N and C_n, which are respectively shown in Equation 3.9 and Equation 3.10. According to the independence of the white Gaussian noise signals in the four channels, the non-diagonal elements in C_n should be 0. In addition, Equation 3.8 has indicated that the calibrated noise signal should have a variance of 1, so the diagonal elements of C_n should be 1. The elements in Equation 3.10 sufficiently meet the expectations.

$$\begin{aligned} C_N &= \begin{bmatrix} var(N_{HH}) & cov(N_{HH},N_{HV}) & cov(N_{HH},N_{VH}) & cov(N_{HH},N_{VV}) \\ cov(N_{HV},N_{HH}) & var(N_{HV}) & cov(N_{HV},N_{VH}) & cov(N_{HV},N_{VV}) \\ cov(N_{VH},N_{HH}) & cov(N_{VH},N_{HV}) & var(N_{VH}) & cov(N_{VH},N_{VV}) \\ cov(N_{VV},N_{HH}) & cov(N_{VV},N_{HV}) & cov(N_{VV},N_{VH}) & var(N_{VV}) \end{bmatrix} \\ &= \begin{bmatrix} 1.33\times10^6 & 9.66\times10^3 - 1.22\times10^4 j & -4.87\times10^3 + 1.12\times10^4 j & -1.17\times10^4 + 4.53\times10^3 j \\ 9.66\times10^3 + 1.22\times10^4 j & 5.47\times10^6 & 1.95\times10^4 + 1.83\times10^4 j & 2.28\times10^4 + 1.11\times10^4 j \\ -4.87\times10^3 - 1.12\times10^4 j & 1.95\times10^4 - 1.83\times10^4 j & 2.32\times10^6 & -2.65\times10^3 + 2.69\times10^4 j \\ -1.17\times10^4 - 4.53\times10^3 j & 2.28\times10^4 - 1.11\times10^4 j & -2.65\times10^3 - 2.69\times10^4 j & 4.96\times10^6 \end{bmatrix} \end{aligned} \tag{3.9}$$

$$
\begin{aligned}
C_n &= \begin{bmatrix} var(n_{HH}) & cov(n_{HH}, n_{HV}) & cov(n_{HH}, n_{VH}) & cov(n_{HH}, n_{VV}) \\ cov(n_{HV}, n_{HH}) & var(n_{HV}) & cov(n_{HV}, n_{VH}) & cov(n_{HV}, n_{VV}) \\ cov(n_{VH}, n_{HH}) & cov(n_{VH}, n_{HV}) & var(n_{VH}) & cov(n_{VH}, n_{VV}) \\ cov(n_{VV}, n_{HH}) & cov(n_{VV}, n_{HV}) & cov(n_{VV}, n_{VH}) & var(n_{VV}) \end{bmatrix} \\
&= \begin{bmatrix} 1 & 0.0036 - 0.0045j & -0.0028 + 0.0064j & -0.0045 + 0.0018j \\ 0.0036 + 0.0045j & 1 & 0.0055 + 0.0052j & 0.0044 + 0.0021j \\ -0.0028 - 0.0064j & 0.0055 - 0.0052j & 1 & -0.0008 + 0.0079j \\ -0.0045 - 0.0018j & 0.0044 - 0.0021j & -0.0008 - 0.0079j & 1 \end{bmatrix}
\end{aligned} \tag{3.10}
$$

In conclusion, the noise-based polarimetric radar calibration algorithm works well on the noise signals from the four receiver channels, resulting in perfectly performed independent white Gaussian noise signals. The channel-specific amplification factor and bias are removed. Consequently, the same calibration algorithm can be applied to the signal data to determine the truly received signals.

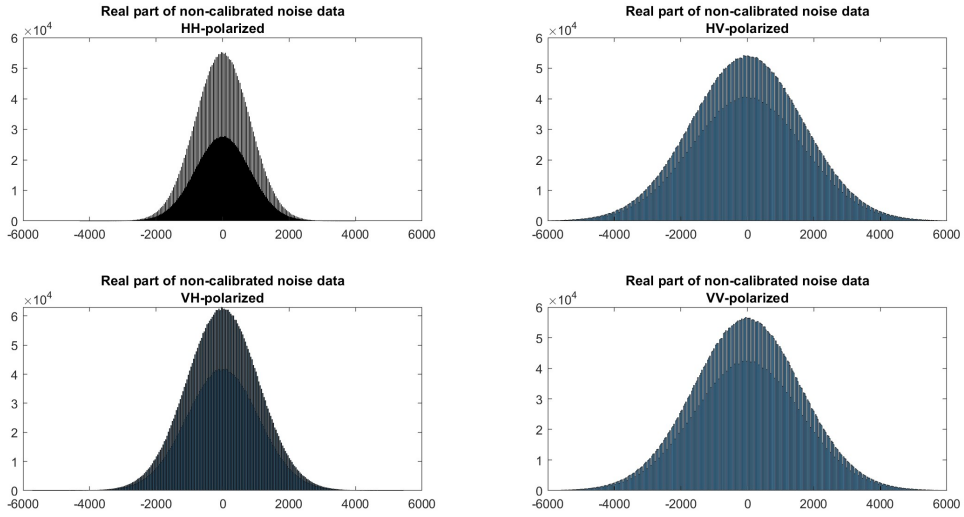

(a)

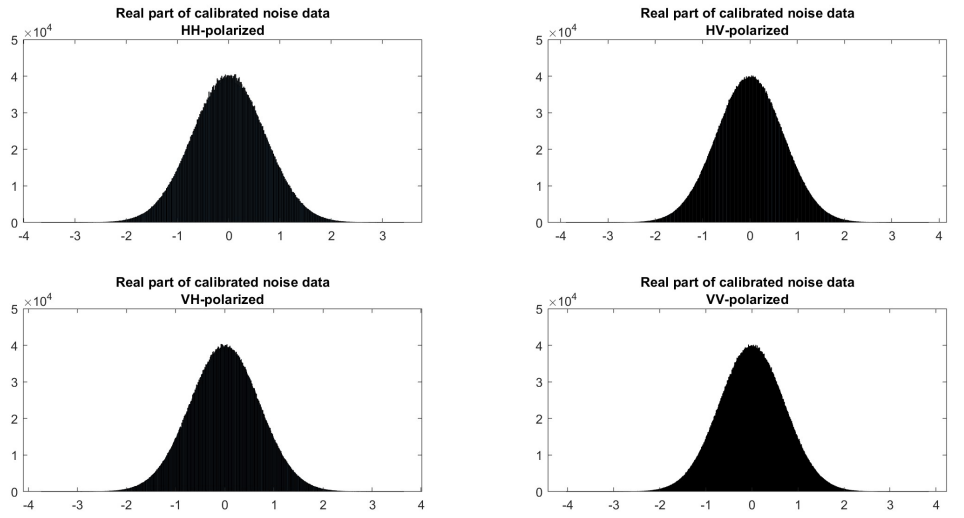

(b)

Figure 3.1: Histograms of (a) non-calibrated noise data (real part) and (b) calibrated noise data (real part) of the four polarimetric channels, indicating that the channel-specific amplification factors are removed

3.1.3. Algorithm Integration into the Processing Chain

Knowing that the noise-based polarimetric radar calibration algorithm can be used to calibrate signals, it needs to be integrated into the signal and data processing chain introduced in Subsection 2.3.1. There are two optional positions to integrate the calibration algorithm. The first option is calibrating the raw data, which can be regarded as a part of the signal pre-processing. The other option is executing the calibration algorithm in the range-Doppler domain. In this case, the calibration can focus on the pixels where the targets are detected instead of the whole data set. Based on the linearity of Doppler processing, these two options should lead to equivalent results. This section will first discuss the equivalence of calibration on raw data and calibration after Doppler processing. Then, additional studies on the noise variance used in the calibration after Doppler processing will be presented. Finally, the choice of calibration option in the signal and data processing chain is elaborated.

Equivalence of Calibration on Raw Data and Calibration after Doppler Processing

Assuming $f(x)$, $g(x)$, and $h(x)$ are integrable functions, and the Fourier transforms of these functions are denoted as $\hat{f}(\xi)$, $\hat{g}(\xi)$, $\hat{h}(\xi)$. Linearity of the Fourier transform elaborates that for any complex numbers a and b, if $h(x) = af(x) + bg(x)$, then $\hat{h}(\xi) = a\hat{f}(\xi) + b\hat{g}(\xi)$ [31]. In addition, the HPF and window function introduced in the signal and data processing chain are also linear operators. Consequently, the Doppler processing has a linear property. The linearity ensures that calibration on raw data and calibration after Doppler processing would have equivalent results, which can also be elaborated by the following equation, the operator DP refers to the Doppler processing:

$$\begin{aligned} DP(y_{i,j}(r,t)) &= DP(\frac{V_{i,j}(r,t) - mean(N_{i,j}(r,t))}{\sqrt{var(N_{i,j}(r,t))}}) \\ &= \frac{DP(V_{i,j}(r,t)) - mean(DP(N_{i,j}(r,t)))}{\sqrt{var(N_{i,j}(r,t))}} \end{aligned} \tag{3.11}$$

Figure 3.2 presents the validating process of the equivalence, which will be realized by comparing the range-Doppler frames with the same frame number achieved from the two calibration options. For the calibration on raw data, after loading noise and signal data, the mean and variance of the noise are calculated over the slow-time dimension to get the range-related values. Then the signal data is calibrated according to Equation 3.8. After then, Doppler processing is performed on the calibrated data to get range-Doppler frames. Finally, one of the range-Doppler frames is selected to be compared. Similar operations are done in the calibration after Doppler processing. The noise and signal data are loaded first, followed by calculating the noise variance over the slow-time dimension. In this case, Doppler processing is also required for the noise data to achieve the noise range-Doppler frames. Then the noise range-Doppler frames are averaged to get the mean frame, which is used to calibrate the signal range-Doppler frames. Finally, the two frames with the same frame number resulting from the two calibration options are compared, and the results are shown in Figure 3.3. The perfect linearity ranging from -20 dB to 40 dB verifies the equivalence of the two calibration options. The non-linearity appearing below -20 dB could be ignored, resulting from bad noise data.

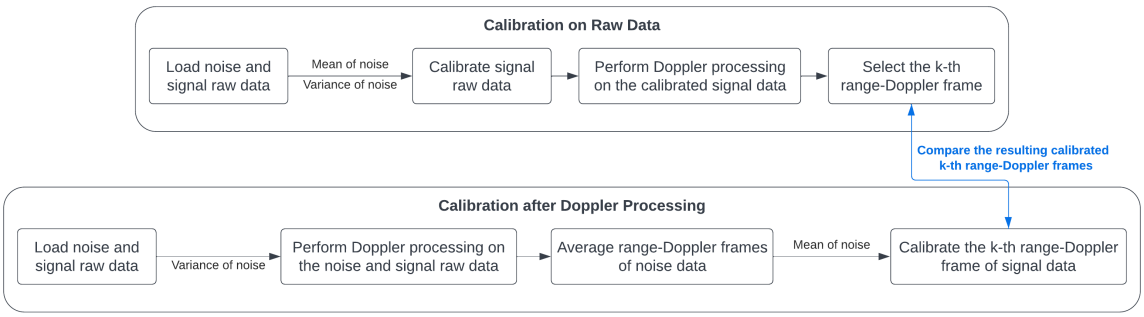

Figure 3.2: Equivalence validation process of calibration on raw data and calibration after Doppler processing

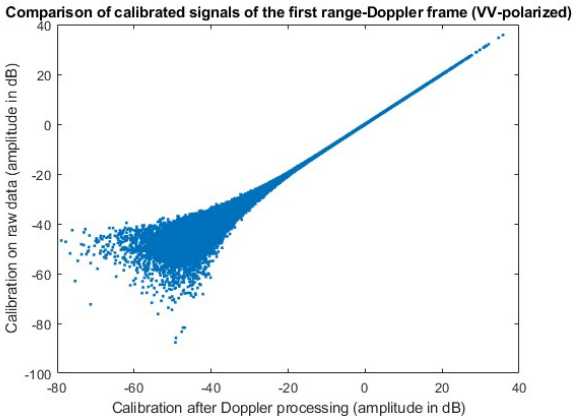

Figure 3.3: Comparison of calibration on raw data and calibration after Doppler processing indicating their equivalence

Noise Variance Used in Calibration after Doppler Processing

The previous sub-subsection has elaborated that in the option of calibration after Doppler processing, the noise variance is calculated from the noise raw data. In this sub-subsection, the feasibility of using the noise variance calculated from the noise range-Doppler frames will be discussed.

The Chebyshev window function used in the Doppler processing can change the noise variance. In addition, if there is a normalization coefficient in the FFT, the noise variance also needs to be compensated. The compensation considering the window function and the FFT normalization coefficient can be realized as follows:

$$var(N_{i,j}(r,t)) = \frac{var(DP(N_{i,j}(r,t))) \times N_{FFT}^2}{sum(w^2)}, \tag{3.12}$$

where N_{FFT} represents the normalization coefficient in the FFT, and w stands for the window function.

In this case, Equation 3.11 becomes to:

$$DP(y_{i,j}(r,t)) = \frac{DP(V_{i,j}(r,t)) - mean(DP(N_{i,j}(r,t)))}{\sqrt{\frac{var(DP(N_{i,j}(r,t))) \times N_{FFT}^2}{sum(w^2)}}}. \tag{3.13}$$

This is validated by a similar process as in Figure 3.2, and the comparison result is shown in Figure 3.4. Again, in the range of -20 dB to 40 dB, the two calibration options are well linearly related, although it is not as good as the result in Figure 3.3. The potential reason could be that when using the noise variance calculated from the noise raw data, the variance is calculated from a massive noise data set, with 63488 variables in this validation process. However, there are only 31 noise range-Doppler frames. The resulting noise variance calculated from the range-Doppler frames would be less stable.

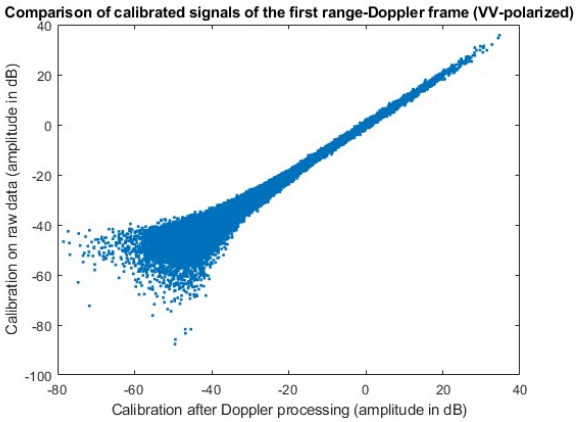

Figure 3.4: Comparison of calibration on raw data and calibration after Doppler processing using noise variance calculated from noise range-Doppler frames

Choice of Calibration Option in the Signal and Data Processing Chain

In the previous two sub-subsections, it has been validated that either calibrating the raw data or calibrating the signal range-Doppler frames will lead to the same result. Besides, when calibrating in the range-Doppler domain, the noise variance can be calculated from the noise raw data or the noise range-Doppler frames. Using the former noise variance will lead to a more stable result.

A final option needs to be chosen in the whole signal and data processing chain, and trade-offs need to be done for the street-way measurements. On the one hand, the interactions between the calibration algorithm and the other algorithms in the processing chain need to be taken into account. For example, even calibration on raw data and calibration after Doppler processing could lead to almost the same result in the range-Doppler frame. The fused results might be different when applying the polarimetric data fusion algorithm to fuse the range-Doppler frames from the four polarimetric channels. Consequently, the target detection results could be different. Therefore, calibration on raw data seems more promising, which is performed before all the other processing algorithms. On the other hand, the workload can be increased by calibrating the raw data and redoing the whole processing chain, since the labels are already added manually in the street-way database as introduced in Subsection 2.3.2. Finally, considering the algorithms' interactions and workload, the street-way measurements are calibrated in the range-Doppler domain. In addition, as mentioned in the thesis introduction (Section 1.1), the previous work in this project focuses on highway measurements. For potential future work in the highway case, calibration on raw data is preferred.

3.2. Phase Compensation

In the polarimetric radar system, a time shift between the transmitted H- and V-polarized signals would lead to a phase difference between the polarimetric channels for moving target detection. The phase difference has to be calibrated to make the polarimetric information of the same scattering mechanism as stable as possible over the target's velocity. In this section, the time shift and the resulting phase difference between the polarimetric channels will be elaborated in detail. Then a phase compensation algorithm proposed in [32] is introduced for compensating the street-way measurements. This compensation algorithm can be used only in the unambiguous Doppler range of the radar system. However, as introduced in Section 1.1, the previous work in this project focuses on highway measurements. For the potential future work on highway measurements, where most of the targets have a folded velocity, the operational domain of this phase compensation algorithm is extended to both ambiguous and unambiguous Doppler velocities.

3.2.1. Phase Difference Between the Polarimetric Channels

In this project, the H-polarized signal and V-polarized signal are transmitted with a time shift of $\triangle t = \frac{PRI}{2} = 0.5\ ms$, as shown in Figure 3.5.

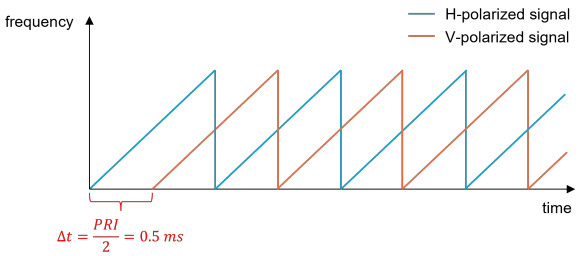

Figure 3.5: Time shift between the H- and V-polarized transmitted signals

For a moving target with a velocity of v, this time shift will lead to a measuring range difference between the H- and V-polarized channels as:

$$\triangle R = 2v \times \triangle t, \tag{3.14}$$

where coefficient 2 stands for the two-way propagation (i.e., EM wave approaches to target and is

scattered back to the radar). Then the phase difference could be calculated as follows:

$$\triangle\phi = \frac{2\pi \times \triangle R}{\lambda} = \frac{4\pi v \times \triangle t}{\lambda}. \tag{3.15}$$

An alternative expression of $\triangle\phi$ can be derived using:

$$\lambda = \frac{4v_{max}}{PRF}, \tag{3.16}$$

and

$$\triangle t = \frac{PRI}{2} = \frac{1}{2PRF}, \tag{3.17}$$

where v_{max} is the positive maximum unambiguous velocity, PRF is the pulse repetition frequency. The resulting $\triangle\phi$ is:

$$\triangle\phi = \frac{\pi v}{2v_{max}}. \tag{3.18}$$

To indicate the linear dependence between the phase difference and the Doppler velocity as in Equations 3.15 and 3.18, one street-way data set and one highway data set are used to plot Figure 3.6. The moving targets' centroid values are used, representing the reflection characteristics of the targets' central bodies. Sub-figure 3.6(a) shows that most targets have a phase difference of around $\pm 1\ rad$ in the street-way case. However, in Sub-figure 3.6(b), only a small part of the targets concentrate around $\triangle\phi$ of $\pm 1\ rad$ in the highway case. Most targets have a phase difference of around $\pm 2\ rad$. The reason for the difference between the two cases is that most targets on the highway exceed the maximum unambiguous velocity. Thus, the measured velocity is folded. The folded velocity leads to another phase difference of π between the H- and V-polarized channels. Consequently, Equations 3.15 and 3.18 can be extended by considering if the velocity is folded or not, as shown below:

$$\triangle\phi = \begin{cases} \frac{4\pi v_{true} \times \triangle t}{\lambda} = \frac{\pi v_{true}}{2v_{max}} & True\ velocity \\ \frac{4\pi v_{folded} \times \triangle t}{\lambda} + \pi = \frac{\pi v_{folded}}{2v_{max}} + \pi & Folded\ velocity \end{cases} \tag{3.19}$$

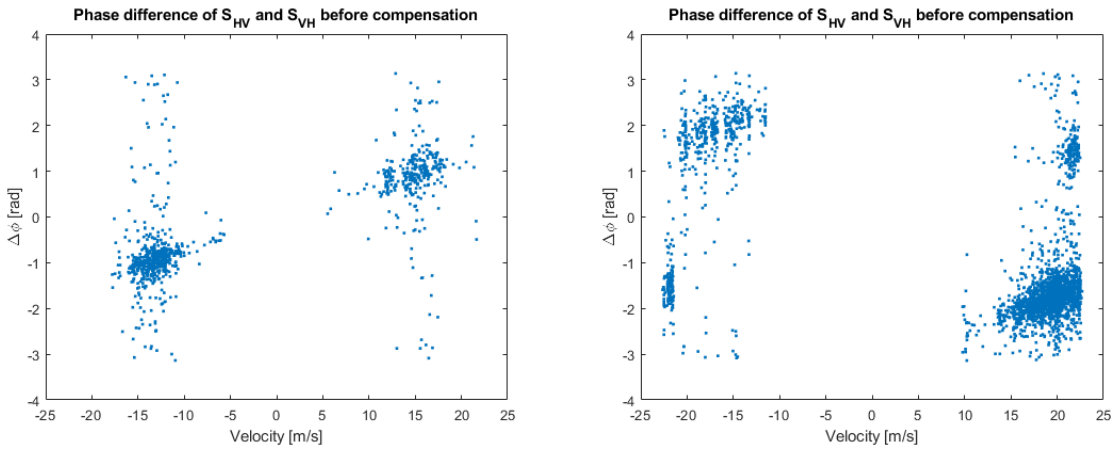

Figure 3.6: Phase difference of S_{HV} and S_{VH} in the (a) street-way and (b) highway cases, with a linear dependence on the Doppler velocity

Using the derived phase difference $\triangle\phi$ for the targets with true velocities and folded velocities, phase compensation algorithms can be developed for the street-way and highway measurements. The detailed algorithms and results will be presented in the next two sub-sections.

3.2.2. Phase Compensation in the Street-Way Measurements

In the street-way case, all targets are measured with the true velocities, where the velocity folding does not need to be considered. Therefore, the phase of S_{VH} and S_{VV} can be compensated using the following algorithm:

$$S'_{VH} = S_{VH} \times e^{j\triangle\phi} = S_{VH} \times e^{j\frac{4\pi v_{true} \times \triangle t}{\lambda}} = S_{VH} \times e^{j\frac{\pi v_{true}}{2v_{max}}}; \tag{3.20}$$

$$S'_{VV} = S_{VV} \times e^{j\triangle\phi} = S_{VV} \times e^{j\frac{4\pi v_{true} \times \triangle t}{\lambda}} = S_{VV} \times e^{j\frac{\pi v_{true}}{2v_{max}}}, \tag{3.21}$$

where S'_{VH} and S'_{VV} stand for the compensated data.

The reciprocity theorem is used to validate the algorithm. The phase difference of S_{HV} and S'_{VH} should concentrate around $0\ rad$, which is verified in Sub-figure 3.7(a). It also shows that the linear dependence between the phase difference and the target's velocity is removed.

Although most of the compensated data meets the reciprocity theorem, there are still some points having a non-zero phase difference in Sub-figure 3.7(a). To explain where the non-zero phase difference comes from, the compensated phase difference with respect to the signal amplitude ($|S_{HV}|$) is plotted in Sub-figure 3.7(b). It could be observed that $\triangle\phi$ has a wider distribution when the signal amplitude is smaller. Thus, it could be concluded that the non-zero phase difference comes from the noisy data.

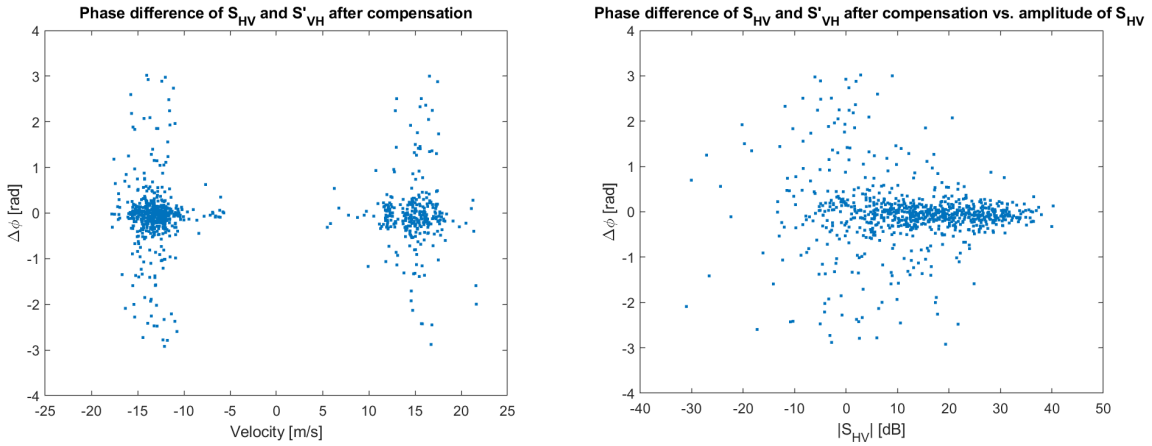

Figure 3.7: Compensation results on the phase difference of S_{HV} and S'_{VH} in the street-way case: (a) compensated phase difference; (b) compensated phase difference w.r.t signal amplitude

In addition, the compensation results for S_{VV} are shown in Appendix B.1. In contrast to the compensation results of S_{VH}, the compensated S'_{VV} does not need to follow the reciprocity theorem, thus the phase difference of S_{HH} and S'_{VV} has a wider distribution.

3.2.3. Phase Compensation in the Highway Measurements

The phase compensation algorithm is extended to the ambiguous case for highway measurements. Utilizing $\triangle\phi$ in Equation 3.19, the phase compensation algorithm that works for both ambiguous and unambiguous targets is as follows:

$$S'_{VH} = \begin{cases} S_{VH} \times e^{j\triangle\phi} = S_{VH} \times e^{j\frac{4\pi v_{true} \times \triangle t}{\lambda}} = S_{VH} \times e^{j\frac{\pi v_{true}}{2v_{max}}} & True\ velocity \\ S_{VH} \times e^{j\triangle\phi} = S_{VH} \times e^{j\frac{4\pi v_{folded} \times \triangle t}{\lambda}} = S_{VH} \times e^{j\frac{\pi v_{folded}}{2v_{max}}} & Folded\ velocity \end{cases}; \tag{3.22}$$

$$S'_{VV} = \begin{cases} S_{VV} \times e^{j\triangle\phi} = S_{VV} \times e^{j\frac{4\pi v_{true} \times \triangle t}{\lambda}} = S_{VV} \times e^{j\frac{\pi v_{true}}{2v_{max}}} & True\ velocity \\ S_{VV} \times e^{j\triangle\phi} = S_{VV} \times e^{j\frac{4\pi v_{folded} \times \triangle t}{\lambda}} = S_{VV} \times e^{j\frac{\pi v_{folded}}{2v_{max}}} & Folded\ velocity \end{cases}. \tag{3.23}$$

Similarly as in Sub-section 3.2.2, the compensated phase difference of S_{HV} and S'_{VH} is plotted versus the Doppler velocity and the signal amplitude ($|S_{HV}|$), which are respectively shown in Sub-figures 3.8(a) and 3.8(b). The compensated data stays around $\triangle\phi$ of $0\ rad$, which satisfies the reciprocity theorem. Additionally, the same conclusion as in the street-way case could be drawn: the compensated points with non-zero phase difference come from noisy data. Finally, the compensation results for S_{VV} are shown in Appendix B.2.

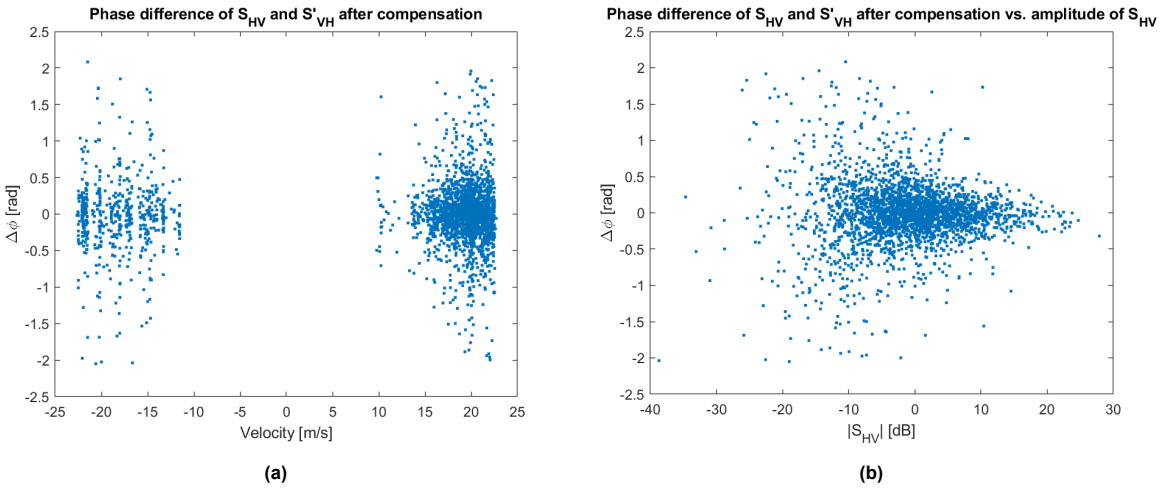

Figure 3.8: Compensation results on the phase difference of S_{HV} and S'_{VH} in the highway case: (a) compensated phase difference; (b) compensated phase difference w.r.t signal amplitude

3.3. Antenna Pattern Compensation

The street-way measurements in this project are affected by the antenna pattern due to the close target ranges. The measurements of vehicles driving on the ends of the street-way suffer from power degradation. In this section, the reasons for the power degradation in measurements will be explained first by presenting the measurement scenario. Then an antenna pattern compensation algorithm is proposed and developed to resolve the power degradation.

3.3.1. Power Degradation in the Measurements

In the street-way measuring scenario, the PARSAX radar observes the vehicles ranging from $1050\ m$ to $1320\ m$, as illustrated in Figure 3.9. The close observation ranges require an antenna beam width of $\theta_a = 25.5° - 20° = 5.5°$ to cover the observing area fully. However, as presented in Table 2.1, the beam widths of the PARSAX transmitter and receiver antennas are $1.8°$ and $4.6°$, respectively. The beam width limitation leads to power degradation in the measurements of the vehicles on both ends of the street-way. Figure 3.10 shows the power of all vehicles w.r.t. their varying ranges, where the antenna pattern is clearly observed. Therefore, an antenna pattern compensation algorithm is developed to resolve this power degradation.

3.3.2. Antenna Pattern Compensation Algorithm

To compensate for the power degradation, the power of all vehicles is averaged for each range step of $1\ m$, resulting in a mean power as a function of range, which is denoted as $\overline{P}(range)$. Then the power P is compensated as:

$$P_c = \frac{P}{\overline{P}(range)} \cdot \overline{P}_{max}(range), \tag{3.24}$$

where P_c denotes the compensated power, $\overline{P}_{max}(range)$ denotes the maximum value of the averaged power. Note that the multiplication of term $\overline{P}_{max}(range)$ aims to shift the compensated power to the

initial power level. The resulting compensated power of all vehicles is shown in Figure 3.11. It is obvious that the antenna pattern is removed.

Note that this power compensation is an example of explaining the antenna pattern compensation algorithm. The algorithm is applied after extracting features. The parameters in the algorithm can vary for different features. For example, amplitudes will replace all the power parameters for the features extracted from the PSMs. More details and the compensation results for each feature will be demonstrated later in Chapter 4.

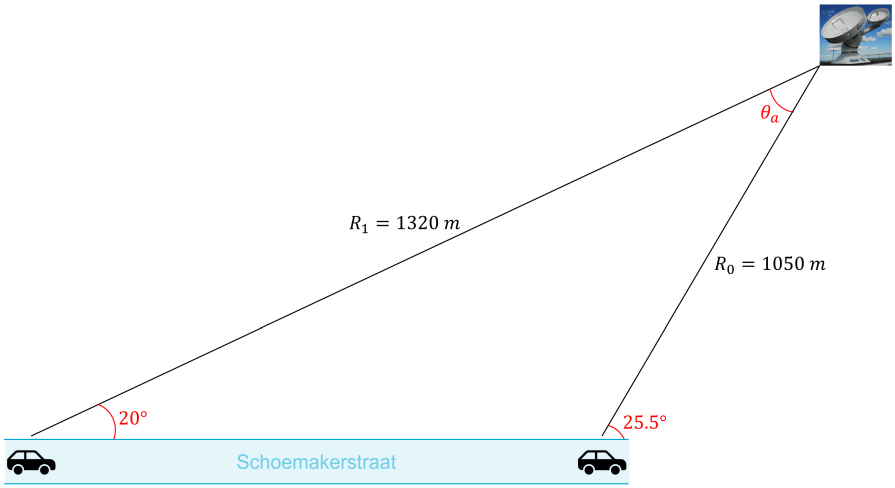

Figure 3.9: Geometrical interpretation of the street-way measuring scenario, indicating required $5.5°$ antenna beam width

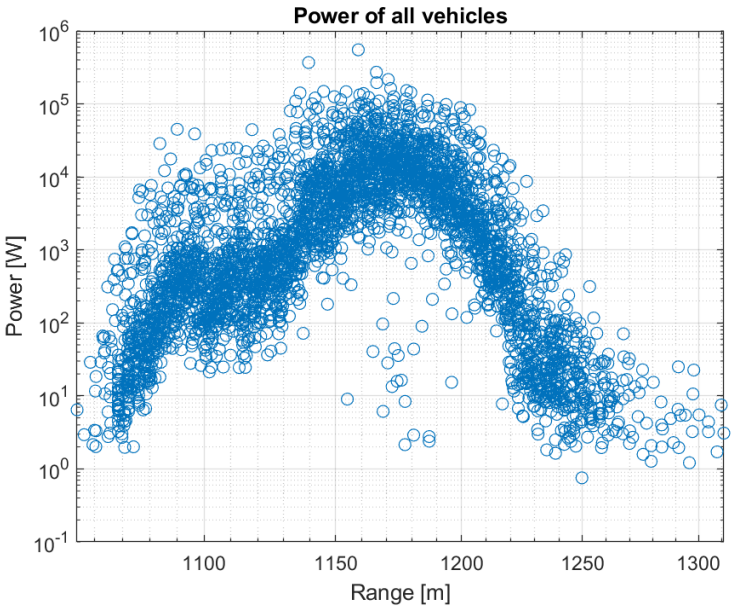

Figure 3.10: Power of all vehicles w.r.t. the varying ranges, indicating the antenna pattern effect

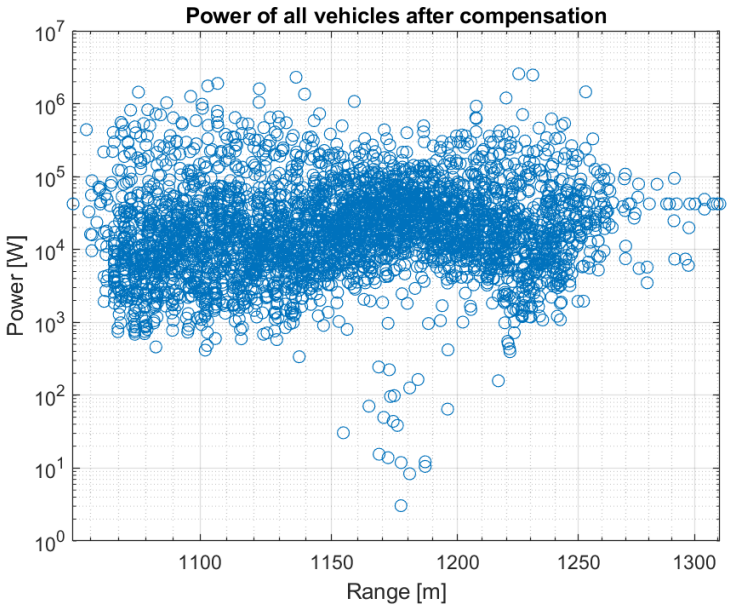

Figure 3.11: Power of all vehicles w.r.t. the varying ranges after antenna pattern compensation, indicating removal of the antenna pattern

3.4. Summary

This chapter proposes three database calibration algorithms to deal with the issues caused by the PARSAX radar's hardware characteristics and measurement settings, which improve feature quality for further analysis. The first algorithm, called the noise-based polarimetric radar calibration algorithm, aims to remove the channel-specific amplification factors and biases due to the non-ideal and non-identical characteristics of the electronic devices in the four polarimetric channels. The algorithm estimates the amplification factors and biases from the noise data, and it is validated utilizing the white Gaussian noise characteristics. The calibrated noise data in the four channels have the same distribution range and are perfectly independent, indicating the algorithm's feasibility. Then the positions of integrating the channel calibration algorithm into the signal and data processing chain are discussed. The equivalence of calibration on raw data and calibration after Doppler processing has been proven. Considering the street-way database has been labeled manually, it is calibrated in the range-Doppler domain to reduce workload.

The second calibration algorithm is developed to compensate for the phase difference between the polarimetric channels when measuring moving targets. Due to the time shift between the transmitted H- and V-polarized signals, a phase difference linearly dependent on the target's velocity appears between the H- and V-polarized channels. The phase compensation is required to make the polarimetric information of the same scattering mechanism as stable as possible over the target's velocity. Thus, a phase compensation algorithm proposed in [32] is applied to the street-way measurements. The phase of S_{VH} and S_{VV} components are compensated. The results indicate that the linear dependence between the phase difference and the target's velocity has been removed, and the reciprocity theorem has been satisfied. Furthermore, the phase compensation algorithm is extended to the ambiguous velocity case for the potential future analysis of the highway database.

The last calibration algorithm is to resolve the power degradation in the measurements of the vehicles driving on both ends of the street-way. Since the observation ranges are rather close in the street-way measurements, the antenna beam is not wide enough to fully cover the observing area. An antenna pattern compensation algorithm is proposed using the averaged power from all vehicles for every range step of $1\ m$. The compensated results demonstrate the removal of the antenna pattern effect. This algorithm will be applied after further feature extractions, leading to more compact results in the feature analysis.

4

Features

Applying the calibration algorithms in the previous chapter, a calibrated labeled street-way database has been achieved for further feature analysis. This chapter focuses on feature extraction and analysis for exploring the vehicles' polarimetric scattering characteristics. In addition, the extracted features will be evaluated for vehicle classification. All features will be extracted under the monostatic backscattering case. Section 4.1 will present the features based on the eigenvalues and eigenvectors (i.e., polarization angles) of the centroid PSMs, which represent the scattering characteristics of vehicles' central bodies. Afterward, in Section 4.2, considering the vehicles are located in a dynamically changing environment, where spatial and temporal variations are involved, the polarimetric coherency and covariance matrices are introduced to describe the space- and time-varying stochastic processes. The eigenvalues and polarization angles extracted from the non-averaged and spatial-averaged coherency and covariance matrices will be analyzed and evaluated. Finally, three features closely related to the vehicles' sizes will be proposed and evaluated in Section 4.3 and Section 4.4, which are target length and two eigenvalues of the covariance matrix of detection cells.

4.1. Eigenvalues/Eigenvectors Decomposition of Centroid PSM

This section focuses on the eigenvalues and eigenvectors (i.e., polarization angles) analysis of the centroid PSMs. The centroid PSM is defined from the detection cell with the largest reflection power ($Span = |S_{HH}|^2 + |S_{HV}|^2 + |S_{VH}|^2 + |S_{VV}|^2$) within the cluster, which represents the scattering characteristics of a vehicle's central body. The eigenvalues and polarization angles are derived through PSM diagonalization. Sub-section 4.1.1 will introduce the diagonalization method based on the Graves matrix. Then the derived eigenvalues and polarization angles will be analyzed in Sub-section 4.1.2 and Sub-section 4.1.3 to characterize the scattering of the vehicles' central bodies and explore potential features contributing to vehicle classification.

4.1.1. Diagonalization of PSM

There exist two methods to realize PSM diagonalization [22]. The first one is performing the standard eigen-decomposition procedure to calculate the eigenvalues and eigenvectors. However, the monostatic backscattering case is considered in this project, where the cross-polarized components (S_{HV} and S_{VH}) of PSM are replaced by their mean:

$$\mathbf{S} = \begin{bmatrix} S_{HH} & \frac{S_{HV}+S_{VH}}{2} \\ \frac{S_{HV}+S_{VH}}{2} & S_{VV} \end{bmatrix}. \tag{4.1}$$

Consequently, the diagonalization of the PSM has to be done by the pseudo eigen-decomposition [33, 34].

The other method is diagonalizing the PSM by deriving the eigenvectors of the Graves polarization coherent power scattering matrix [35], which is the diagonalization method used in this thesis. The Graves matrix is denoted as **G** and given by:

$$\mathbf{G} = \mathbf{S}^*\mathbf{S} = \begin{bmatrix} |S_{HH}|^2 + |S_{HV}|^2 & S_{HH}^* S_{HV} + S_{HV}^* S_{VV} \\ S_{HV}^* S_{HH} + S_{VV}^* S_{HV} & |S_{HV}|^2 + |S_{VV}|^2 \end{bmatrix}. \tag{4.2}$$

Note that the monostatic backscattering case is taken into account in Equation 4.2 as well, where the term S_{HV} has been replaced by the mean of the original S_{HV} and S_{VH}. The Graves **G** matrix is a Hermitian matrix with two real non-negative eigenvalues and orthogonal unit eigenvectors, which can be derived as:

$$\lambda_{1,2}^G = \frac{Tr(\mathbf{G}) \pm \sqrt{Tr(\mathbf{G})^2 - 4|\mathbf{G}|}}{2},\ \lambda_1^G \geq \lambda_2^G, \tag{4.3}$$

and

$$\vec{u}_{1,2} = \frac{e^{j\xi}}{\sqrt{1 + |\frac{\lambda_{1,2}^G - G_{11}}{G_{12}}|^2}} \begin{bmatrix} 1 \\ \frac{\lambda_{1,2}^G - G_{11}}{G_{12}} \end{bmatrix}, \tag{4.4}$$

where $Tr(\mathbf{G})$ equals the sum of diagonal terms of **G** matrix, $|\mathbf{G}|$ is the determinant of **G** matrix, and ξ stands for the target absolute phase. These two eigenvectors correspond to the polarization states that null the cross-polarized components [36]. Since the two polarization states are orthogonal, the eigenvectors can be formulated in a general way:

$$\begin{aligned} \vec{u}_1 &= \frac{e^{j\xi}}{\sqrt{1 + |\rho_1|^2}} \begin{bmatrix} 1 \\ \rho_1 \end{bmatrix} \\ &= \begin{bmatrix} cos\psi & -sin\psi \\ sin\psi & cos\psi \end{bmatrix} \begin{bmatrix} cos\tau_m & jsin\tau_m \\ jsin\tau_m & cos\tau_m \end{bmatrix} \begin{bmatrix} e^{+j\alpha} & 0 \\ 0 & e^{-j\alpha} \end{bmatrix} \hat{u}_1 \\ &= \mathbf{U}_2(\psi, \tau_m, \alpha)\hat{u}_1. \end{aligned} \tag{4.5}$$

The orientation angle ψ and ellipticity angle τ_m have the same meanings as explained in the EM wave polarization ellipse (Figure 2.2). These two angles are also assigned to the physical characteristics of the targets. ψ is related to the target orientation around the radar line-of-sight. τ_m corresponds to the maximum polarization $\vec{u}_1$, is often called the "helicity angle" that determines target symmetry ($\tau_m = 0$) or asymmetry ($\tau_m \neq 0$). Therefore, the Graves **G** matrix can be diagonalized as:

$$\mathbf{G}_D = \mathbf{U}_2(\psi, \tau_m, \alpha)^{-1}\mathbf{G}\mathbf{U}_2(\psi, \tau_m, \alpha). \tag{4.6}$$

Then according to:

$$\begin{aligned} \mathbf{G}_D &= \mathbf{S}_D^*\mathbf{S}_D \\ &= \mathbf{U}_2(\psi, \tau_m, \alpha)^{-1}\mathbf{S}^*\mathbf{S}\mathbf{U}_2(\psi, \tau_m, \alpha) \\ &= \mathbf{U}_2(\psi, \tau_m, \alpha)^{-1}\mathbf{S}^*\mathbf{U}_2(\psi, \tau_m, \alpha)^*\mathbf{U}_2(\psi, \tau_m, \alpha)^T\mathbf{S}\mathbf{U}_2(\psi, \tau_m, \alpha), \end{aligned} \tag{4.7}$$

the diagonalized PSM is given by:

$$\mathbf{S}_D = \mathbf{U}_2(\psi, \tau_m, \alpha)^T\mathbf{S}\mathbf{U}_2(\psi, \tau_m, \alpha). \tag{4.8}$$

Finally, knowing the diagonalized PSM, the eigenvalues of the PSM can be derived as:

$$\lambda_1 = \mathbf{S}_D^{11}; \tag{4.9}$$

$$\lambda_2 = \mathbf{S}_D^{22}, \tag{4.10}$$

where the superscripts denote the element indices of the matrix, and $\lambda_1 \geq \lambda_2$ by definition. The derived eigenvalues and polarization angles (i.e., orientation and ellipticity angles) will be analyzed in the following two sub-sections.

4.1.2. Eigenvalues Analysis

In this sub-section, the eigenvalues of the centroid PSMs of the multi-class vehicles at all time frames are analyzed. The antenna pattern compensation algorithm is first applied to the eigenvalues before the analysis. Then the compensated eigenvalues are specifically analyzed for the different classes of vehicles. Based on the analysis, eight features are extracted and evaluated for vehicle classification.

Antenna Pattern Compensation on Eigenvalues

Figure 4.1 (a) and (b) respectively show the first and second eigenvalues (absolute) of the six classes of vehicles at all time frames. To make the eigenvalues more compact in further analysis, the antenna pattern is removed first using the algorithm proposed in Section 3.3. The range-related mean eigenvalues are calculated for every range step of $1\ m$, then the eigenvalues are compensated as shown in Figure 4.2. It could be observed that the eigenvalues are related to the vehicles' sizes. Large vehicles (i.e., small trucks and large trucks) have larger eigenvalues than small ones (i.e., multi-class sedans and mini-vans). This observation is consistent with the theorem that the PSM's eigenvalues correspond to the targets' reflection amplitudes. The physical explanation is clear that the central bodies of larger vehicles should have stronger reflections.

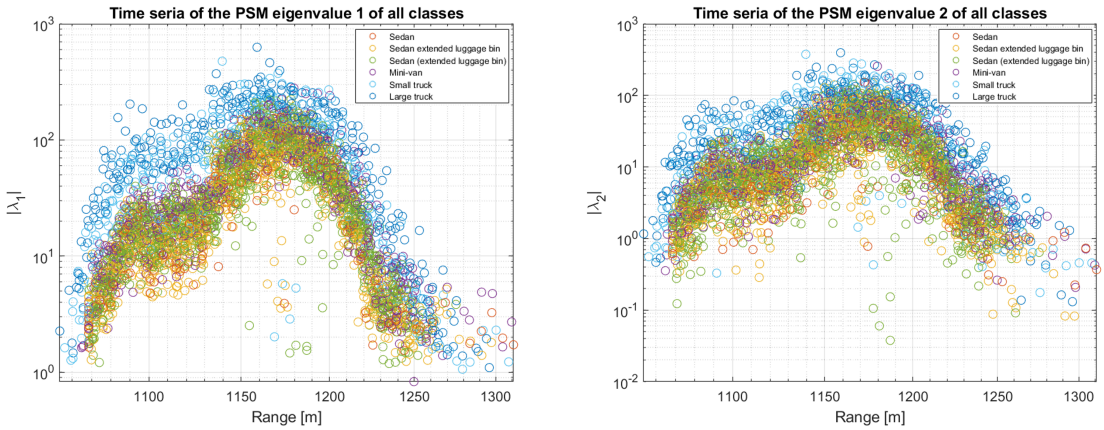

Figure 4.1: Eigenvalues (absolute) of the centroid PSMs of the multi-class vehicles at all time frames: (a) the first eigenvalues; (b) the second eigenvalues, where the antenna pattern effect needs to be removed before further analysis

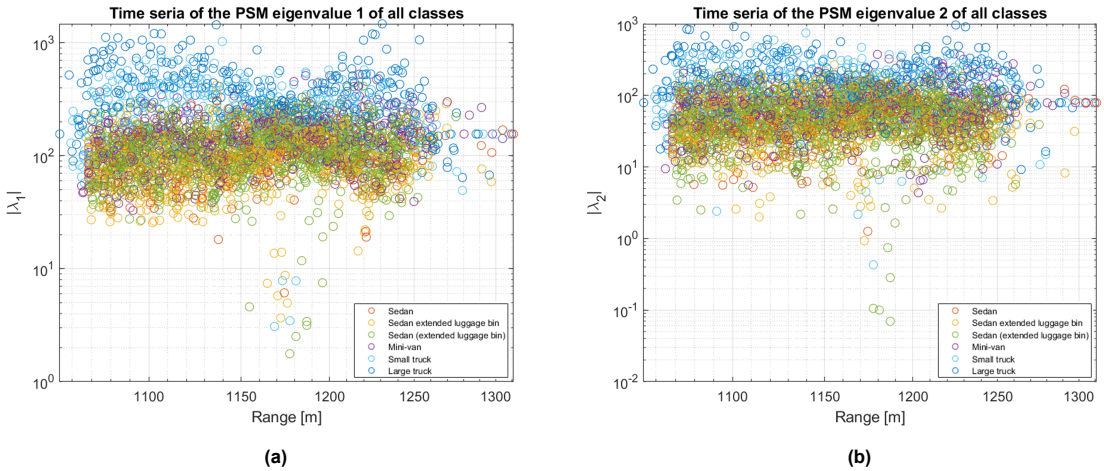

Figure 4.2: Eigenvalues (absolute) of the centroid PSMs of the multi-class vehicles at all time frames after antenna pattern compensation: (a) the first eigenvalues; (b) the second eigenvalues, which correspond to the reflection amplitudes of the vehicles' central bodies

Eigenvalues Analysis for Multi-Class Vehicles

To specifically analyze the eigenvalues of the different classes of vehicles, the eigenvalues (real and imaginary parts) are plotted in separate figures according to their classes. Figure 4.3, as one of the six figures, indicates the eigenvalues from sedans with extended luggage bins. The red points represent the first eigenvalues, and the blue ones represent the second. Both eigenvalues form Gaussian-like distributions with a mean close to zero. Similar Gaussian-like distributions with nearly zero mean can be found in other vehicle classes, and the figures are presented in Appendix C.1.

To statistically characterize the distributions of the eigenvalues, the moments, including mean, variance, skewness, and kurtosis, are calculated for the eigenvalues of the different vehicle classes. The results are illustrated in Table 4.1 and Table 4.2.

From the two tables, several conclusions could be drawn as follows:

1. For both λ_1 and λ_2, their absolute values have distinguishable mean values among the six vehicle classes. The mean values increase as the vehicles' sizes;
2. For both λ_1 and λ_2, their real and imaginary parts, as well as their absolute values, all have distinguishable variances among the six vehicle classes. The variances increase as the vehicles' sizes;
3. For both λ_1 and λ_2, their real and imaginary parts, as well as their absolute values, all have similar skewness and kurtosis among the six vehicle classes.

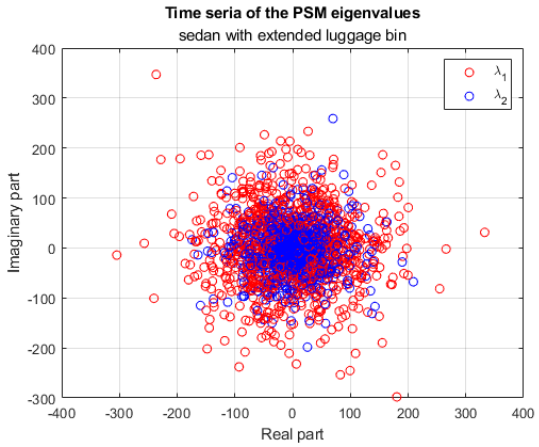

Figure 4.3: Eigenvalues (real and imaginary parts) of the centroid PSMs of sedans with extended luggage bins at all time frames, which form Gaussian-like distributions with a mean close to zero

Table 4.1: Moments of the first eigenvalues of centroid PSMs of the multi-class vehicles

			Real part of λ_1			
	Sedan	**Sedan with extended luggage bin**	**Sedan (with extended luggage bin)**	**Mini-van**	**Small truck**	**Large truck**
Mean	6.86	-2.31	3.59	0.56	6.61	34.23
Variance	5.5×10^3	6.75×10^3	8.84×10^3	1.36×10^4	4.91×10^4	1.07×10^5
Skewness	-0.002	0.06	0.01	0.18	-0.01	0.20
Kurtosis	2.54	3.18	3.19	3.25	4.03	4.16
			Imaginary part of λ_1			
	Sedan	**Sedan with extended luggage bin**	**Sedan (with extended luggage bin)**	**Mini-van**	**Small truck**	**Large truck**
Mean	-0.03	1.87	1.25	3.16	6.08	-3.85
Variance	6.57×10^3	6.71×10^3	8.62×10^3	1.37×10^4	4.8×10^4	1.31×10^5
Skewness	-0.12	-0.03	-0.005	-0.27	0.12	0.39
Kurtosis	3.15	3.38	2.78	3.67	3.10	4.07
			Absolute value of λ_1			
	Sedan	**Sedan with extended luggage bin**	**Sedan (with extended luggage bin)**	**Mini-van**	**Small truck**	**Large truck**
Mean	99.12	103.78	120.10	148.37	273.63	420.00
Variance	2.23×10^3	2.68×10^3	3.04×10^3	5.23×10^3	2.21×10^4	6.22×10^4
Skewness	0.79	1.18	0.91	1.51	1.16	1.41
Kurtosis	3.88	5.60	4.29	7.34	5.14	5.38

Table 4.2: Moments of the second eigenvalues of centroid PSMs of the multi-class vehicles

			Real part of λ_2			
	Sedan	**Sedan with extended luggage bin**	**Sedan (with extended luggage bin)**	**Mini-van**	**Small truck**	**Large truck**
Mean	3.13	-0.25	1.36	-1.53	0.68	2.01
Variance	1.79×10^3	2.18×10^3	2.53×10^3	4.08×10^3	1.62×10^4	3.74×10^4
Skewness	0.01	0.10	0.14	7.22×10^{-4}	0.10	-0.27
Kurtosis	4.67	4.63	4.24	4.55	5.45	6.83
			Imaginary part of λ_2			
	Sedan	**Sedan with extended luggage bin**	**Sedan (with extended luggage bin)**	**Mini-van**	**Small truck**	**Large truck**
Mean	-2.81	-3.04	0.51	3.12	10.47	6.14
Variance	1.79×10^3	2.01×10^3	2.34×10^3	4.48×10^3	1.52×10^4	3.55×10^4
Skewness	-0.38	0.13	0.10	-0.52	0.24	-0.24
Kurtosis	3.82	5.47	4.11	5.78	4.45	5.64
			Absolute value of λ_2			
	Sedan	**Sedan with extended luggage bin**	**Sedan (with extended luggage bin)**	**Mini-van**	**Small truck**	**Large truck**
Mean	49.21	53.21	58.39	76.54	142.54	218.71
Variance	1.16×10^3	1.36×10^3	1.45×10^3	2.71×10^3	1.11×10^4	2.49×10^4
Skewness	1.33	1.42	1.14	1.75	1.53	1.76
Kurtosis	5.23	5.75	4.45	7.86	6.66	7.39

The obvious differences in mean and variance between different vehicle classes are more intuitively reflected in Figure 4.4, which provides a comparison of the mean and standard deviation of the absolute eigenvalues among the six vehicle classes using the so-called errorbar plot. The asterisk indicates the mean value, and the bar length on each side of the asterisk equals the standard deviation. Note that the standard deviation is used instead of the variance to shorten the bar and make the results more observable.

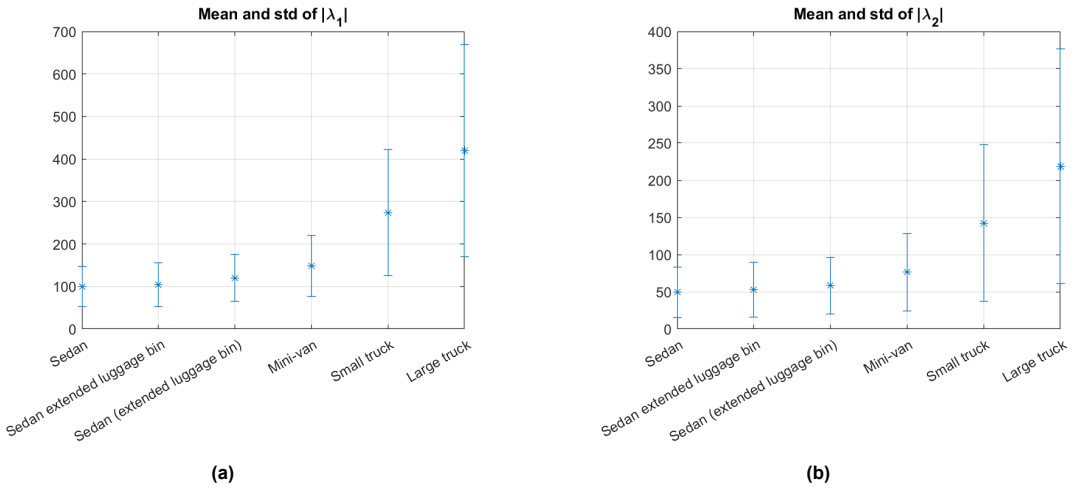

Figure 4.4: Obvious difference in mean (asterisk) and standard deviation (bar length on each side of the asterisk) of the eigenvalues (absolute) of the centroid PSMs between the six vehicle classes: (a) the first eigenvalues; (b) the second eigenvalues

Feature Evaluation

Based on the eigenvalues analysis results, the mean of absolute eigenvalues and the standard deviations of real, imaginary, and absolute eigenvalues can be regarded as potential features contributing to vehicle classification. To evaluate the classification performances of these features, the features are extracted for each vehicle, which means that each vehicle has its own mean and standard deviations calculated from the eigenvalues over its time frames. The eight features compose four similar feature spaces. Thus, only one of the feature spaces is shown here in Figure 4.5, and the others could be found in Appendix C.2. The feature spaces involve all vehicles, and each point represents one vehicle. The solid rectangles stand for the boundaries of the six vehicle classes, and the dashed rectangles illustrate the standard deviations of the clusters. These rectangles reflect the separability and compact-

ness of the six clusters, which reveals the features' classification performances to some extent. The feature spaces indicate that the large trucks can be easily distinguished from the multi-class sedans and mini-vans. The small trucks can be distinguished from the multi-class sedans as well. However, the small trucks are confused with the large trucks and mini-vans. In addition, it is hard to classify multi-class sedans and mini-vans.

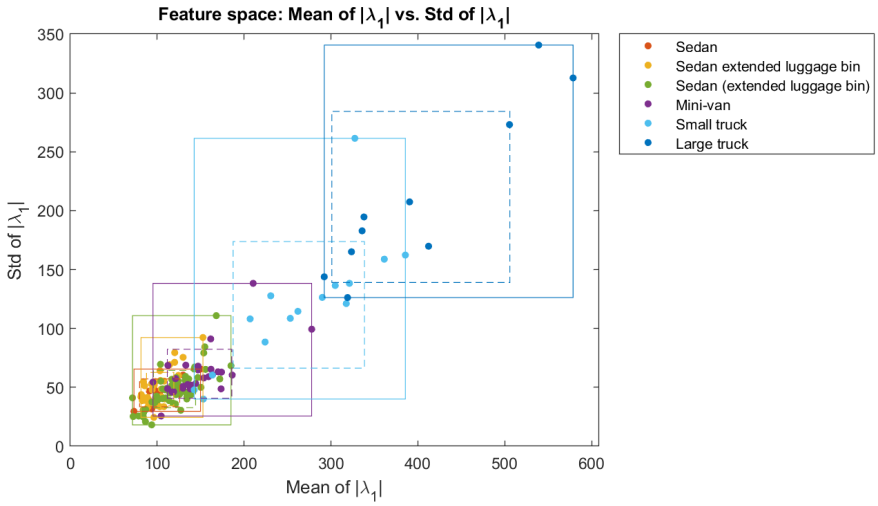

Figure 4.5: Feature space of mean of λ_1 (absolute) vs. standard deviation of λ_1 (absolute), where λ_1 is the first eigenvalue of the centroid PSM

Preliminary conclusions of the features' classification performances have been drawn from the feature spaces. Additionally, the Silhouette coefficient is selected to be the metric to quantify the clustering performances of the eight features among each class pair. The Silhouette metric evaluates the compactness of the cluster and the separability of the cluster w.r.t. the other one. It represents the difference between the average intra-class distance and the average inter-class distance, normalized by the maximum of these two average distances [37]. The derivation of the Silhouette coefficient for each data point in a cluster is given by:

$$s_i = \frac{b_i - a_i}{max\left\{a_i, b_i\right\}}, \; -1 \leq s_i \leq 1, \tag{4.11}$$

where a_i is the average inter-class distance, and b_i is the average intra-class distance. The Silhouette coefficients of all data points in each cluster are averaged for feature evaluations. A result close to 1 means the cluster is compact and separable from the other one [38]. The resulting Silhouette coefficients are presented in Figure 4.6, where x-labels list the eight features, and y-labels give all the vehicle class pairs. The Silhouette coefficients support the conclusions drawn from the previous feature spaces. The following conclusions are summarized by sequentially analyzing the class pairs from top to bottom in Figure 4.6:

1. The multi-class sedans cannot be classified using the proposed features. The maximum Silhouette coefficient achieved in the class pairs of sedans is only 0.6229.
2. It is possible to distinguish sedans from mini-vans using the standard deviation of the first eigenvalue (real part), with the Silhouette coefficient being 0.8405.
3. The Silhouette coefficients achieve high values among the sedan-small truck and sedan-large truck pairs. Only the standard deviation of the first eigenvalue (imaginary part) has a value lower than 0.9. The other features have values close to 1.
4. The sedans with extended luggage bins can be distinguished from mini-vans using the mean of the first eigenvalue (absolute). The Silhouette coefficient is 0.829.
5. The sedans with extended luggage bins can be easily distinguished from small and large trucks. All features achieve Silhouette coefficients close to 1.

6. The sedans (with extended luggage bins) can also be easily distinguished from small and large trucks. All features achieve Silhouette coefficients close to 1.
7. It is possible to distinguish mini-vans from small and large trucks. Most of the features achieve Silhouette coefficients over 0.8.
8. It is difficult to classify small and large trucks. The maximum Silhouette coefficient achieved is only 0.6713.

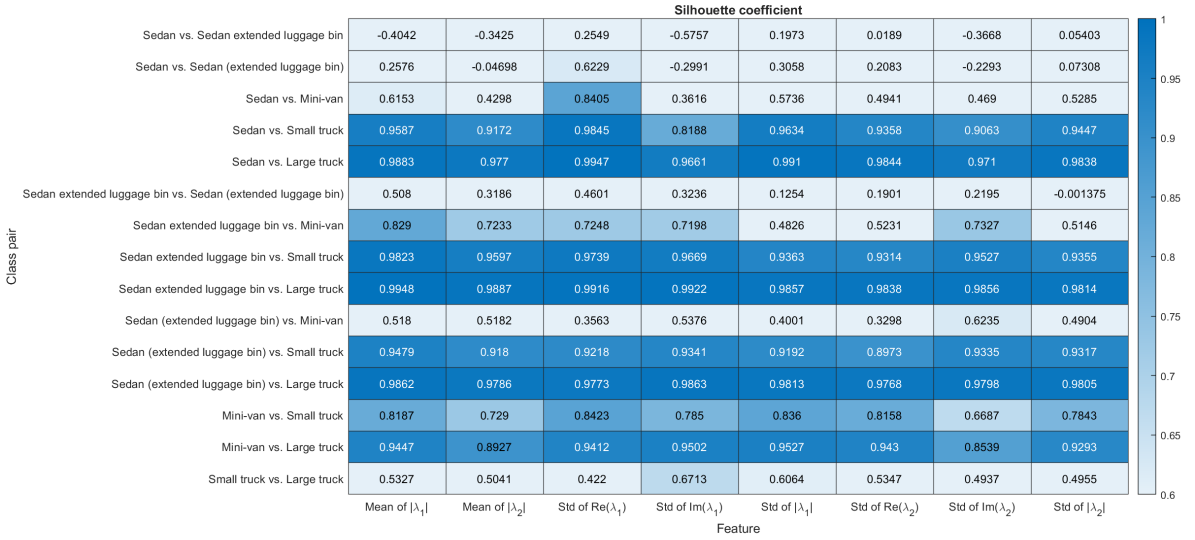

Figure 4.6: Silhouette coefficients achieved by the eight features among each class pair

4.1.3. Polarization Angles Analysis

In this sub-section, the polarization angles calculated from the centroid PSMs of the vehicles at all time frames are analyzed. Firstly, the antenna pattern effect is checked on the polarization angles. Then the polarization angles are analyzed for the multi-class vehicles to characterize the polarization basis of the vehicles' central bodies.

Antenna Pattern Effect on Polarization Angles

Before analyzing the polarization angles, the antenna pattern effect is checked to determine if the antenna pattern compensation algorithm is needed. Figure 4.7 shows the orientation angles and ellipticity angles calculated from the first eigenvectors of the six classes of vehicles at all time frames. Obviously, the polarization angles are not affected by the antenna pattern. The same results can be observed from the polarization angles of the second eigenvectors, which are presented in Appendix C.3.

Polarization Angles Analysis for Multi-Class Vehicles

Figure 4.7 has indicated similar behaviors of the polarization angles from different vehicle classes. To specifically analyze the polarization angles for different classes of vehicles, the polarization angles are plotted in separate figures according to their classes. Since the two eigenvectors are orthogonal, the analysis focuses only on the first eigenvector. Similar distributions are found for different classes of vehicles. Thus, only one of the figures is presented here, as shown in Figure 4.8, and the others can be found in Appendix C.4. Since all vehicles have similar distributions of polarization angles, the polarization angles from all the vehicles with different classes are plotted together in Figure 4.9, which is a two-dimensional histogram of the polarization angles. The orientation angles concentrate around 0° and $\pm 90^\circ$, which indicates that horizontal/vertical polarizations dominate the central bodies of the vehicles. The dominations can also be explained by the two eigenvalues in Figure 4.1. Since the two eigenvalues are comparable, the dominant polarization can either be HH or VV. Moreover, the

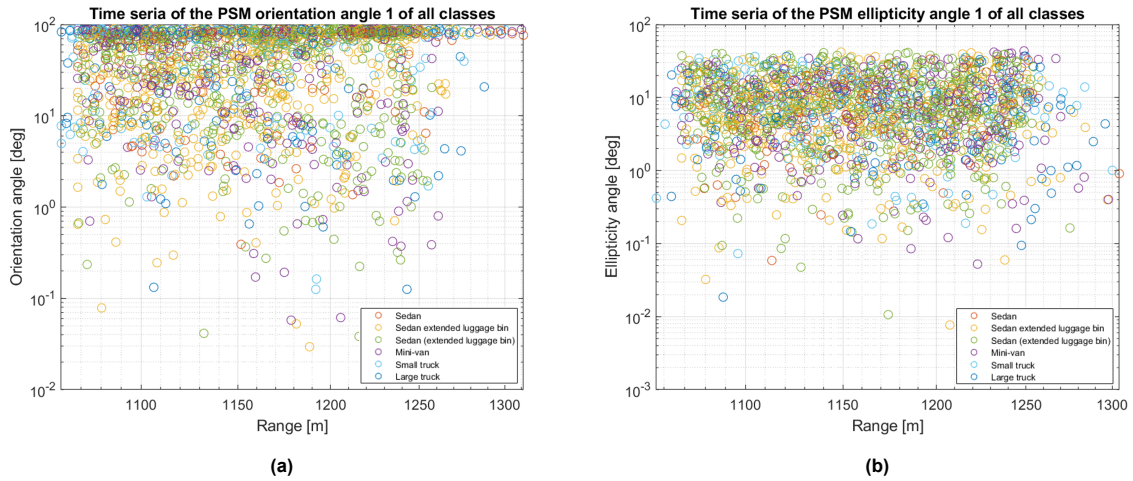

Figure 4.7: Polarization angles: (a) orientation angles of the first eigenvectors; (b) ellipticity angles of the first eigenvectors of the centroid PSMs of the multi-class vehicles at all time frames, which are not affected by the antenna pattern

small bias of the orientation angles against $0°$ and $\pm 90°$ can correspond to the polarization angle in the measurement setting, which is set to be $3.39°$ when measuring street-way vehicles. As for the ellipticity angles, they are concentrated around $0°$, which relates to linear polarizations. This is aligned with the theorem that man-made structures have zero ellipticity angles [22]. These scattering characteristics can be explained by the fact that all vehicle classes have flat planes as their central bodies. Furthermore, from the vehicle classification perspective, the conclusion is that polarization angles do not contribute to vehicle classification.

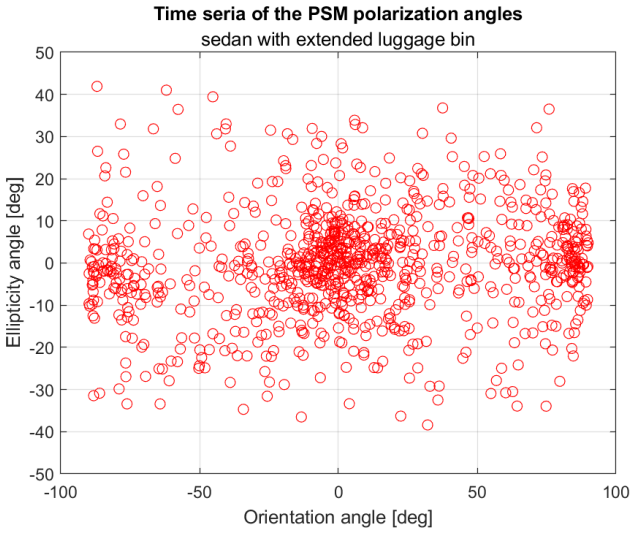

Figure 4.8: Polarization angles of the first eigenvectors of the centroid PSMs of sedans with extended luggage bins at all time frames

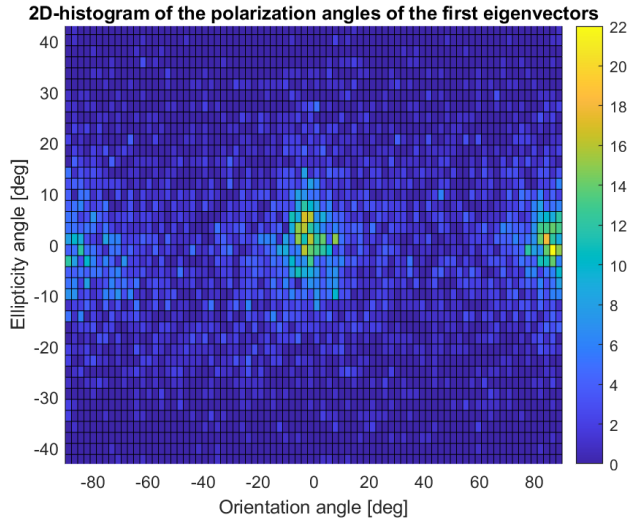

Figure 4.9: 2D-histogram of the polarization angles of the first eigenvectors of all vehicle classes at all time frames, indicating horizontal, vertical orientations and linear polarizations of the vehicles' central bodies

4.2. Eigenvalues/Eigenvectors Decomposition of Coherency and Covariance Matrices

In this section, the vehicle fluctuations due to spatial and temporal variations in the dynamically changing environment will be analyzed based on the polarimetric coherency and covariance matrices. The eigenvalues and polarization angles of the coherency and covariance matrices will be analyzed statistically. Firstly, the definitions of the coherency and covariance matrices in the monostatic backscattering case will be elaborated in Sub-section 4.2.1. Then the diagonalization of the coherency and covariance matrices will be introduced in Sub-section 4.2.2 to derive the eigenvalues and eigenvectors. Afterward, the eigenvector-based decomposition method will be presented in Sub-section 4.2.3 to extract polarization angles from the eigenvectors. The eigenvalues and polarization angles of non-averaged and spatial-averaged coherency and covariance matrices will be analyzed in Sub-section 4.2.4 and Sub-section 4.2.5, representing the scattering characteristics of the vehicles' central bodies and whole bodies, respectively. Finally, the reasons for not analyzing the temporal-averaged coherency/covariance matrix in this thesis will be explained in Sub-section 4.2.6.

4.2.1. Coherency/Covariance Matrix in Monostatic Backscattering Case

The physical information of the classical 2×2 coherent PSM is best extracted through the construction of system vectors [22]. The vectorization of PSM relies on different basis sets in the literature. The special set used to generate the coherency matrix is based on a linear combination arising from the Pauli matrix. The Pauli spin matrix basis set $\{\Phi_P\}$ in the monostatic backscattering case ($S_{HV} = S_{VH}$) is given by:

$$\{\Phi_P\} = \left\{ \sqrt{2} \begin{bmatrix} 1 & 0 \\ 0 & 1 \end{bmatrix} \; \sqrt{2} \begin{bmatrix} 1 & 0 \\ 0 & -1 \end{bmatrix} \; \sqrt{2} \begin{bmatrix} 0 & 1 \\ 1 & 0 \end{bmatrix} \right\}, \tag{4.12}$$

where the three Pauli basis matrices correspond to three canonical scattering mechanisms: the first being a plane surface, the second being a horizontal dihedral, and the third being a dihedral with a relative orientation of $45°$. Then the corresponding vector form of PSM is formulated as:

$$\vec{k} = \frac{1}{\sqrt{2}} \begin{bmatrix} S_{HH} + S_{VV} & S_{HH} - S_{VV} & 2S_{HV} \end{bmatrix}^T. \tag{4.13}$$

Instead of using the Pauli basis as in the coherency matrix, the basis set used to generate the covariance matrix is based on a linear combination arising from the Lexicographic matrix. The Lexicographic

matrix basis set $\{\Phi_L\}$ in the monostatic backscattering case ($S_{HV} = S_{VH}$) is given by:

$$\{\Phi_L\} = \left\{ 2\begin{bmatrix}1 & 0\\ 0 & 0\end{bmatrix}\ 2\sqrt{2}\begin{bmatrix}0 & 1\\ 0 & 0\end{bmatrix}\ 2\begin{bmatrix}0 & 0\\ 0 & 1\end{bmatrix}\right\}. \tag{4.14}$$

Then the corresponding vector form of PSM is formulated as:

$$\vec{\Omega} = \begin{bmatrix} S_{HH} & \sqrt{2}S_{HV} & S_{VV}\end{bmatrix}^T. \tag{4.15}$$

Note that the factor $\sqrt{2}$, 2 or $2\sqrt{2}$ in Equations 4.12 and 4.14 is to keep the invariance of the Span (i.e., total power) of PSM during the vectorization, such that:

$$\begin{aligned} Span(\mathbf{S}) &= |S_{HH}|^2 + 2|S_{HV}|^2 + |S_{VV}|^2 \\ &= \vec{k}^{*T}\cdot\vec{k} = |\vec{k}|^2 \\ &= \vec{\Omega}^{*T}\cdot\vec{\Omega} = |\vec{\Omega}|^2. \end{aligned} \tag{4.16}$$

From the vector forms of the PSM, the 3×3 coherency matrix (denoted as **T**) and covariance matrix (denoted as **C**) in the monostatic backscattering case are defined as:

$$\begin{aligned} \mathbf{T} &= \langle \vec{k}\cdot\vec{k}^{*T}\rangle = \langle \begin{bmatrix} |k_1|^2 & k_1k_2^* & k_1k_3^* \\ k_2k_1^* & |k_2|^2 & k_2k_3^* \\ k_3k_1^* & k_3k_2^* & |k_3|^2\end{bmatrix}\rangle \\ &= \frac{1}{2}\begin{bmatrix} \langle|S_{HH}+S_{VV}|^2\rangle & \langle(S_{HH}+S_{VV})(S_{HH}-S_{VV})^*\rangle & 2\langle(S_{HH}+S_{VV})S_{HV}^*\rangle \\ \langle(S_{HH}-S_{VV})(S_{HH}+S_{VV})^*\rangle & \langle|S_{HH}-S_{VV}|^2\rangle & 2\langle(S_{HH}-S_{VV})S_{HV}^*\rangle \\ 2\langle S_{HV}(S_{HH}+S_{VV})^*\rangle & 2\langle S_{HV}(S_{HH}-S_{VV})^*\rangle & 4\langle|S_{HV}|^2\rangle\end{bmatrix}; \end{aligned} \tag{4.17}$$

$$\begin{aligned} \mathbf{C} &= \langle\vec{\Omega}\cdot\vec{\Omega}^{*T}\rangle = \langle\begin{bmatrix} |\Omega_1|^2 & \Omega_1k_2^* & \Omega_1\Omega_3^* \\ \Omega_2\Omega_1^* & |\Omega_2|^2 & \Omega_2\Omega_3^* \\ \Omega_3\Omega_1^* & \Omega_3\Omega_2^* & |\Omega_3|^2\end{bmatrix}\rangle \\ &= \begin{bmatrix} \langle|S_{HH}|^2\rangle & \sqrt{2}\langle S_{HH}S_{HV}^*\rangle & \langle S_{HH}S_{VV}^*\rangle \\ \sqrt{2}\langle S_{HV}S_{HH}^*\rangle & 2\langle|S_{HV}|^2\rangle & \sqrt{2}\langle S_{HV}S_{VV}^*\rangle \\ \langle S_{VV}S_{HH}^*\rangle & \sqrt{2}\langle S_{VV}S_{HV}^*\rangle & \langle|S_{VV}|^2\rangle\end{bmatrix}. \end{aligned} \tag{4.18}$$

The operator $\langle ...\rangle$ indicates the temporal or spatial averaging, assuming homogeneity of the random medium. Note that by the definitions of the coherency **T** matrix and covariance **C** matrix, both matrices are Hermitian positive semi-definite matrices, which implies that the sum of diagonal elements of **T** or **C** matrix equals the Span, and both matrices have real non-negative eigenvalues and orthogonal eigenvectors.

4.2.2. Diagonalization of Coherency/Covariance Matrix

The eigenvalues and eigenvectors of the coherency **T** matrix and covariance **C** matrix can be achieved by diagonalizing the **T** and **C** matrices as:

$$\mathbf{T} = \mathbf{U}_T\mathbf{T}_D\mathbf{U}_T^{-1}; \tag{4.19}$$

$$\mathbf{C} = \mathbf{U}_C\mathbf{C}_D\mathbf{U}_C^{-1}, \tag{4.20}$$

with

$$\mathbf{T}_D = \mathbf{C}_D = \begin{bmatrix}\lambda_1 & 0 & 0\\ 0 & \lambda_2 & 0\\ 0 & 0 & \lambda_3\end{bmatrix},\ \lambda_1\geq\lambda_2\geq\lambda_3; \tag{4.21}$$

$$\mathbf{U}_T = \begin{bmatrix}\vec{u}_{T1} & \vec{u}_{T2} & \vec{u}_{T3}\end{bmatrix}; \tag{4.22}$$

$$\mathbf{U}_C = \begin{bmatrix}\vec{u}_{C1} & \vec{u}_{C2} & \vec{u}_{C3}\end{bmatrix}. \tag{4.23}$$

$\mathbf{T}_D$ and $\mathbf{C}_D$ are the diagonalized **T** and **C** matrices with three diagonal elements being non-negative real eigenvalues. The **T** and **C** matrices have the same eigenvalues by their definitions. The term $\mathbf{U}_T$ or $\mathbf{U}_C$ is the 3×3 unitary matrix consisting of the three unit orthogonal eigenvectors. Note that the derivations of $\mathbf{U}_T$, $\mathbf{U}_C$ and $\mathbf{T}_D$, $\mathbf{C}_D$ are firstly implemented by trying the analytical expressions formulated in [22]. However, the analytical expressions do not give correct results that satisfy Equations 4.19 and 4.20. Therefore, the Matlab function "eig" is used in this thesis [39], resulting in satisfactory eigenvalues and eigenvectors.

The physical meanings of the three eigenvalues are clear. They correspond to the vehicles' reflection power. The eigenvalues analysis can follow a similar procedure as that of the centroid PSM. Nevertheless, the eigenvectors do not have determined physical explanations. To analyze the polarization basis from the eigenvectors, the eigenvector-based decomposition method is introduced in the next subsection.

4.2.3. Eigenvector-Based Decomposition of Coherency/Covariance Matrix

As illustrated in the previous sub-section, the three eigenvectors of the **T** or **C** matrix are unit and orthogonal. Thus, three uncorrelated scattering mechanisms can be obtained from the three eigenvectors. The **T** or **C** matrix can be expanded into the sum of three independent sub-coherency matrices $\mathbf{T}_1$, $\mathbf{T}_2$, and $\mathbf{T}_3$, or sub-covariance matrices $\mathbf{C}_1$, $\mathbf{C}_2$, and $\mathbf{C}_3$. Each represents a deterministic scattering mechanism corresponding to a single equivalent PSM. The contributions of the three deterministic scattering mechanisms are specified by the eigenvalues derived in Equation 4.21, and the three eigenvectors determine the scattering types [22, 40]. This eigenvector-based decomposition is formulated as follows:

$$\mathbf{T} = \sum_{i=1}^{3} \lambda_i \vec{u}_{Ti} \cdot \vec{u}_{Ti}^{*T} = \mathbf{T}_1 + \mathbf{T}_2 + \mathbf{T}_3; \tag{4.24}$$

$$\mathbf{C} = \sum_{i=1}^{3} \lambda_i \vec{u}_{Ci} \cdot \vec{u}_{Ci}^{*T} = \mathbf{C}_1 + \mathbf{C}_2 + \mathbf{C}_3. \tag{4.25}$$

It is important to clarify that if only λ_1 is non-zero, then it means no spatial/temporal averaging is executed on the **T** or **C** matrix. In this case, the **T** or **C** matrix is related only to the first eigenvalue and the corresponding eigenvector as:

$$\mathbf{T} = \mathbf{T}_1 = \lambda_1 \vec{u}_{T1} \cdot \vec{u}_{T1}^{*T} = \vec{k}_1 \cdot \vec{k}_1^{*T}; \tag{4.26}$$

$$\mathbf{C} = \mathbf{C}_1 = \lambda_1 \vec{u}_{C1} \cdot \vec{u}_{C1}^{*T} = \vec{\Omega}_1 \cdot \vec{\Omega}_1^{*T}; \tag{4.27}$$

The **T** or **C** matrix corresponds to a "pure" target, and a single equivalent PSM is related to the **T** or **C** matrix.

However, when the spatial/temporal averaging is applied, the **T** or **C** matrix has three non-zero eigenvalues. If all eigenvalues are equal, then the **T** or **C** matrix can be interpreted as three orthogonal scattering mechanisms with equal distributions, and the target is said to be "random" without correlated polarized structures. On the other hand, if the **T** or **C** matrix has three non-zero and non-equal eigenvalues, then the **T** or **C** matrix corresponds to "partial targets". Three equivalent PSMs can be derived from $\vec{k}_i,\ i = 1, 2, 3$ in **T** matrix case:

$$\vec{k}_i = \sqrt{\lambda_i} \cdot \vec{u}_{Ti}; \tag{4.28}$$

$$S_i^{HH} = \frac{1}{\sqrt{2}}(\vec{k}_i^{11} + \vec{k}_i^{21}); \tag{4.29}$$

$$S_i^{VV} = \frac{1}{\sqrt{2}}(\vec{k}_i^{11} - \vec{k}_i^{21}); \tag{4.30}$$

$$S_i^{HV} = \frac{1}{\sqrt{2}}\vec{k}_i^{31}; \tag{4.31}$$

$$\mathbf{S}_i = \begin{bmatrix} S_i^{HH} & S_i^{HV} \\ S_i^{HV} & S_i^{VV} \end{bmatrix}, \tag{4.32}$$

or from $\vec{\Omega}_i,\ i = 1, 2, 3$ in **C** matrix case:

$$\vec{\Omega}_i = \sqrt{\lambda_i} \cdot \vec{u}_{Ci}; \tag{4.33}$$

$$S_i^{HH} = \vec{\Omega}_i^{11}; \tag{4.34}$$

$$S_i^{VV} = \vec{\Omega}_i^{31}; \tag{4.35}$$

$$S_i^{HV} = \frac{1}{\sqrt{2}}\vec{\Omega}_i^{21}; \tag{4.36}$$

$$\mathbf{S}_i = \begin{bmatrix} S_i^{HH} & S_i^{HV} \\ S_i^{HV} & S_i^{VV} \end{bmatrix}. \tag{4.37}$$

Note that the superscripts of $\vec{k}_i$ and $\vec{\Omega}_i$ represent the matrix indices. Consequently, three equivalent PSMs are achieved, then for each equivalent PSM, two polarization angles could be derived for polarization basis analysis.

This eigenvector-based decomposition of **T** or **C** matrix applies to most target representations. The target is represented by nine real elements: three non-negative real eigenvalues and a set of six polarization angles.

4.2.4. Analysis on Non-Averaged Coherency/Covariance Matrix

The **T** and **C** matrices are first analyzed without spatial/temporal averaging. The centroid PSMs of the vehicles at every time frame are used to generate the **T** and **C** matrices, following the calculations in Sub-section 4.2.1. Then the **T** and **C** matrices are diagonalized as in Sub-section 4.2.2 to derive the eigenvalues and eigenvectors. The eigenvalues will be analyzed in the first sub-subsection, involving antenna pattern compensation, multi-class vehicles' eigenvalues analysis, and potential feature evaluations. While the eigenvectors will not be analyzed in the non-spatial/temporal averaging case, the reasons will be explained in the second sub-subsection.

Eigenvalues Analysis

As demonstrated in the previous sub-section, only the first eigenvalue is non-zero for the case of non-spatial/temporal averaged **T** or **C** matrix. Thus, the other two eigenvalues will not be presented and analyzed here. Besides, the **T** and **C** matrices have the same eigenvalues. The following analysis will only present the results from the **T** matrix. The **C** matrix leads to exactly the same conclusions.

Figure 4.10 presents the first eigenvalues of **T** or **C** matrices. It could be observed that the first eigenvalues are squared of the PSM eigenvalues in Figure 4.1, which validates the theorem that the eigenvalues of the **T** or **C** matrix represent the reflection power of the scattering mechanisms.

The following eigenvalues analysis follows a similar procedure as in eigenvalues of centroid PSMs (Sub-section 4.1.2). Figure 4.11 presents the first eigenvalues after compensating the antenna pattern using the algorithm proposed in Section 3.3. Since the eigenvalues are related to the reflection power from the vehicles' central bodies, the eigenvalues are acting as expected that large vehicles (i.e., small and large trucks) have larger eigenvalues than small ones (i.e., multi-class sedans and mini-vans).

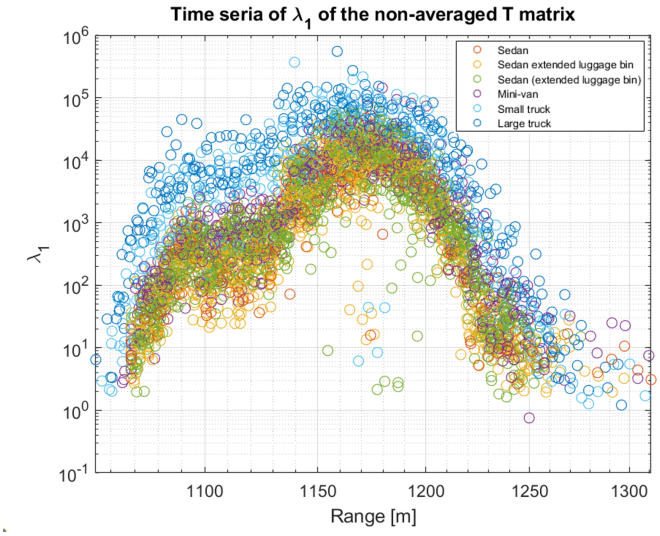

Figure 4.10: The first eigenvalues of the non-averaged coherency/covariance matrices of the multi-class vehicles at all time frames, where the antenna pattern effect needs to be removed before further analysis

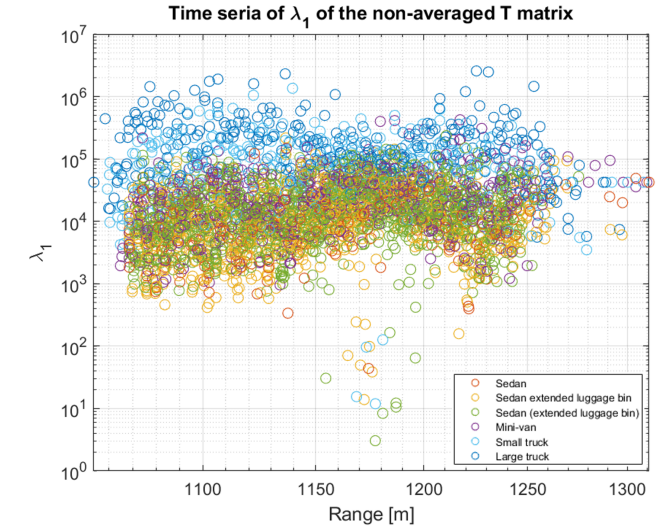

Figure 4.11: The first eigenvalues of the non-averaged coherency/covariance matrices of the multi-class vehicles at all time frames after antenna pattern compensation, which correspond to the reflection power of the vehicles' central bodies

Afterward, with the compensated eigenvalues, statistical analysis is done by calculating the moments of the eigenvalues for different vehicle classes. The moments including mean, variance, skewness, and kurtosis, are illustrated in Table 4.3. It could be concluded from the table that the mean and variance have distinguishable values among the six vehicle classes, and they increase with the vehicles' sizes. This conclusion is presented more intuitively in Figure 4.12, where the asterisk indicates the mean value, and the bar length on each side of the asterisk equals the standard deviation. Using the standard deviation instead of variance is to shorten the bar length and make the results more observable. In addition, the kurtosis also plays a potential role in vehicle classification. Consequently, three features will be evaluated in the non-averaged **T** or **C** matrix case: mean, standard deviation, and kurtosis of the first eigenvalues.

To evaluate these three features, they are extracted for each vehicle to form the feature spaces. Two feature spaces are plotted as shown in Figure 4.13 and Figure 4.14. Note that the mean and standard

Table 4.3: Moments of the first eigenvalues of non-averaged coherency/covariance matrices

	Sedan	Sedan with extended luggage bin	Sedan (with extended luggage bin)	Mini-van	Small truck	Large truck
Mean	1.52×10^4	1.68×10^4	2.11×10^4	3.37×10^4	1.13×10^5	2.67×10^5
Variance	2.64×10^8	4.08×10^8	4.95×10^8	1.98×10^9	1.92×10^{10}	1.28×10^{11}
Skewness	2.54	3.27	2.55	4.67	3.93	3.61
Kurtosis	13.46	20.69	13.90	33.66	27.22	19.17

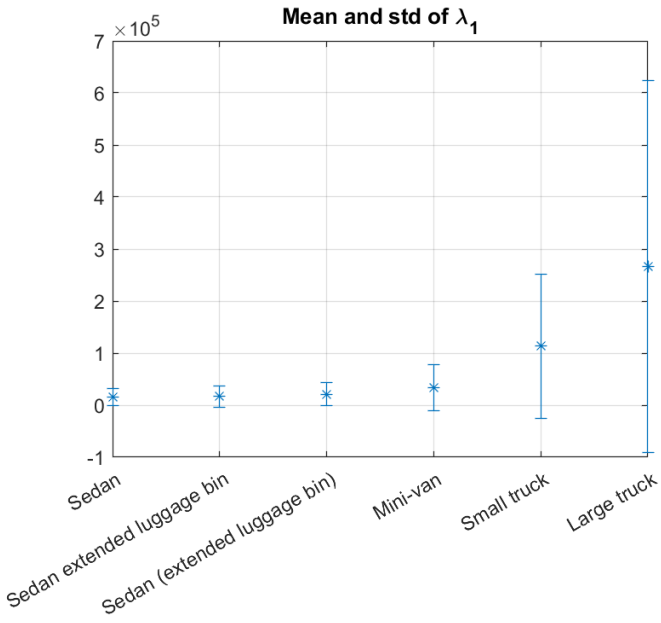

Figure 4.12: Obvious difference in mean (asterisk) and standard deviation (bar length on each side of the asterisk) of the first eigenvalues of the non-averaged coherency/covariance matrices between the six vehicle classes

deviations are plotted in log-scale to make the small vehicles more extended in the feature spaces. From the feature spaces, the capabilities of the first two features in distinguishing large vehicles from small vehicles are obvious, while the kurtosis does not contribute a lot.

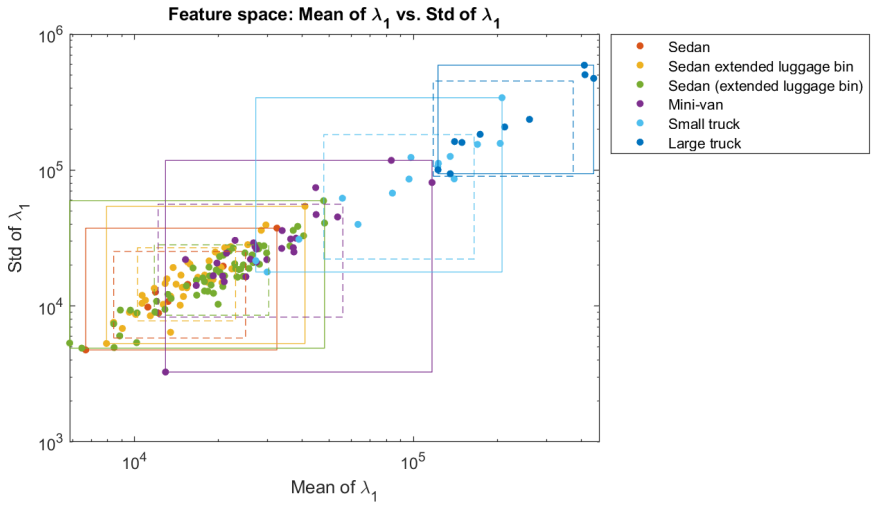

Figure 4.13: Feature space of mean of λ_1 vs. standard deviation of λ_1, where λ_1 is the first eigenvalue of the non-averaged coherency/covariance matrix

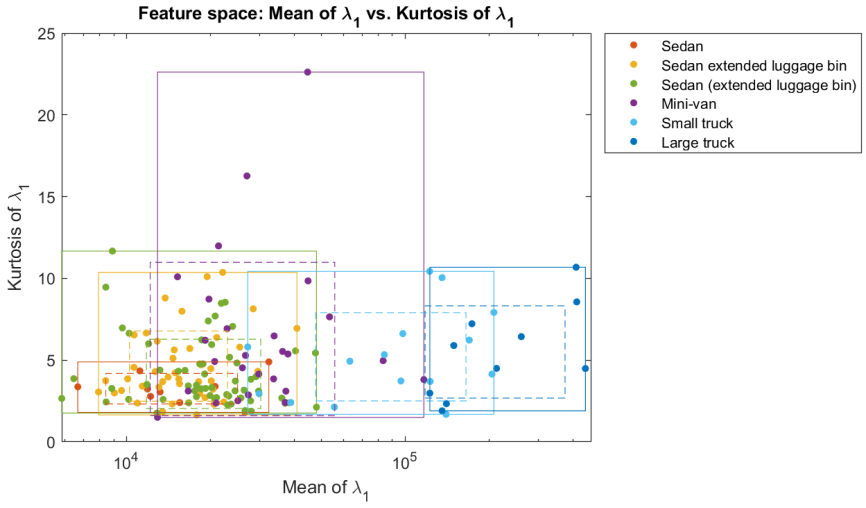

Figure 4.14: Feature space of mean of λ_1 vs. kurtosis of λ_1, where λ_1 is the first eigenvalue of the non-averaged coherency/covariance matrix

To further evaluate the clustering performances of these features, the Silhouette coefficient is calculated in this case as well. The definition of the Silhouette coefficient has been conducted in Sub-section 4.1.2. Figure 4.15 indicates the Silhouette coefficient of each feature among each class pair. The following conclusions are summarized from the Silhouette coefficients by sequentially analyzing the class pairs from top to bottom in Figure 4.15:

1. It is hard to classify multi-class sedans using these three features. The maximum Silhouette coefficient achieved in the class pairs of sedans is only 0.7259;
2. The kurtosis of λ_1 performs well in classifying sedans and mini-vans. The Silhouette coefficient is 0.9409;
3. For the classification of multi-class sedans and small/large trucks, the mean and std of λ_1 achieve high Silhouette coefficients (close to 1) in all possible class pairs. However, the kurtosis of λ_1 only provides potential classification capabilities in sedan vs. small/large truck pairs;
4. The sedans with extended luggage bins can be distinguished from mini-vans using the mean of λ_1. The Silhouette coefficient is 0.881;
5. None of the three features performs well in classifying the sedans (with extended luggage bins) and mini-vans. The same conclusion is drawn in the small truck vs. large truck pair;
6. Mini-vans can be easily distinguished from large trucks using the mean and std of λ_1. Classifying mini-vans and small trucks is also possible, with the Silhouette coefficient being 0.8513 and 0.8703.

Reasons for Not Analyzing Polarization Angles

As introduced in the eigenvector-based decomposition of **T** or **C** matrix (Sub-section 4.2.3), an equivalent PSM could be found for extracting polarization angles. However, the equivalent PSM of the non-averaged coherency or covariance matrix should be the centroid PSM, which has been analyzed in Section 4.1. Therefore, the polarization angles are not analyzed repeatedly here.

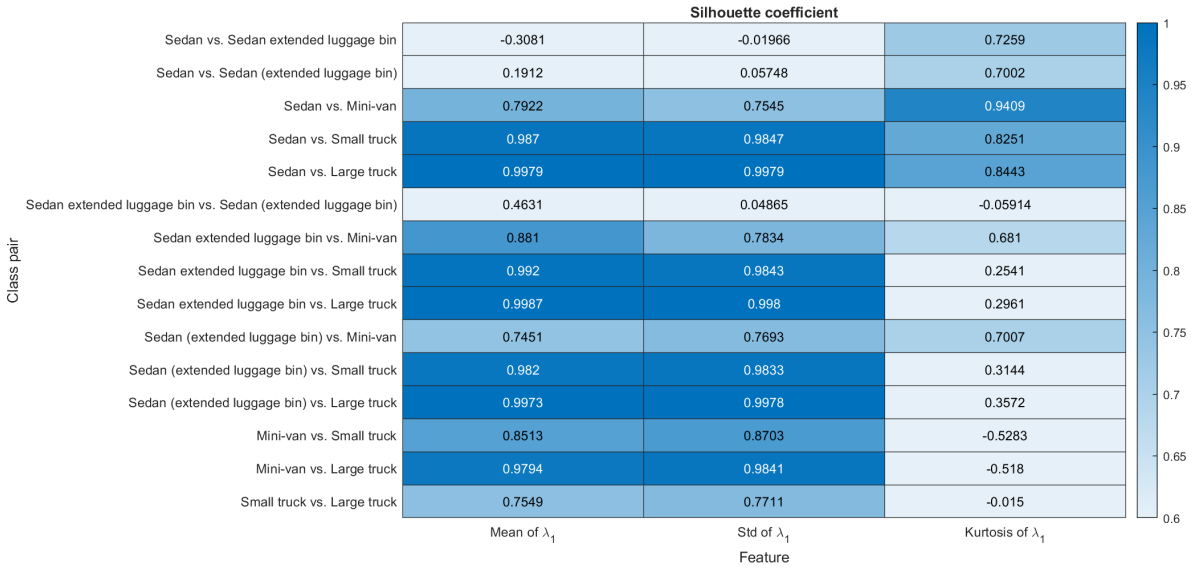

Figure 4.15: Silhouette coefficients achieved by mean, standard deviation, and kurtosis of the first eigenvalues of the non-averaged coherency/covariance matrices among each class pair

4.2.5. Analysis on Spatial-Averaged Coherency/Covariance Matrix

The previous analysis uses only the centroid PSMs, which means only the scattering of each vehicle's dominant mechanism is characterized. Nevertheless, the spatial-averaged **T** or **C** matrix utilizes the PSMs from the whole vehicle body at each time frame. The derivations follow the algorithms in Sub-section 4.2.1. Then the eigenvalues and eigenvectors are achieved through diagonalization of the spatial-averaged **T** or **C** matrices (Sub-section 4.2.2). The spatial-averaged **T** and **C** matrices analysis will reflect the scattering characteristics of the whole vehicle structure. The following content will present the detailed eigenvalues and polarization angles analysis.

Eigenvalues Analysis

Figure 4.16 presents the three eigenvalues of the spatial-averaged **T** matrices of the multi-class vehicles at all time frames. The spatial-averaged **C** matrices have the same results. The three eigenvalues are non-zero and real, as the theorem demonstrates (Sub-section 4.2.2). Besides, the three eigenvalues are non-equal, specifying the non-equal contributions of the three scattering mechanisms of the vehicles. In addition, the antenna pattern effect is obvious for all three eigenvalues, which need to be removed for further analysis. The antenna pattern compensation algorithm proposed in Section 3.3 is applied to obtain the compensated eigenvalues in Figure 4.17. The compensated eigenvalues have stable levels over varying ranges. Furthermore, the physical meanings of the eigenvalues are satisfied that large vehicles have large reflection power, resulting in large eigenvalues.

Then an eigenvalues analysis procedure similar to the non-averaged **T** or **C** matrix analysis is carried out. The distributions of the three eigenvalues are statistically characterized by their moments for different vehicle classes. The moments including mean, variance, skewness, and kurtosis, are illustrated in Table 4.4. The mean and variance of the three eigenvalues all have great potential in vehicle classification, which are also visualized by the asterisks (mean) and bar length on each side of the asterisk (standard deviation) in Figure 4.18. Note that the standard deviation is used instead of the variance to shorten the bar lengths and make the comparisons among classes more visible. Apart from the mean and variance that are increasing with the vehicles' sizes, the kurtosis of the three eigen-

values also has obvious differences among the vehicle classes, especially the kurtosis of the second eigenvalue. Thus, nine features will be evaluated in the following content: mean, standard deviation, and kurtosis of the three eigenvalues.

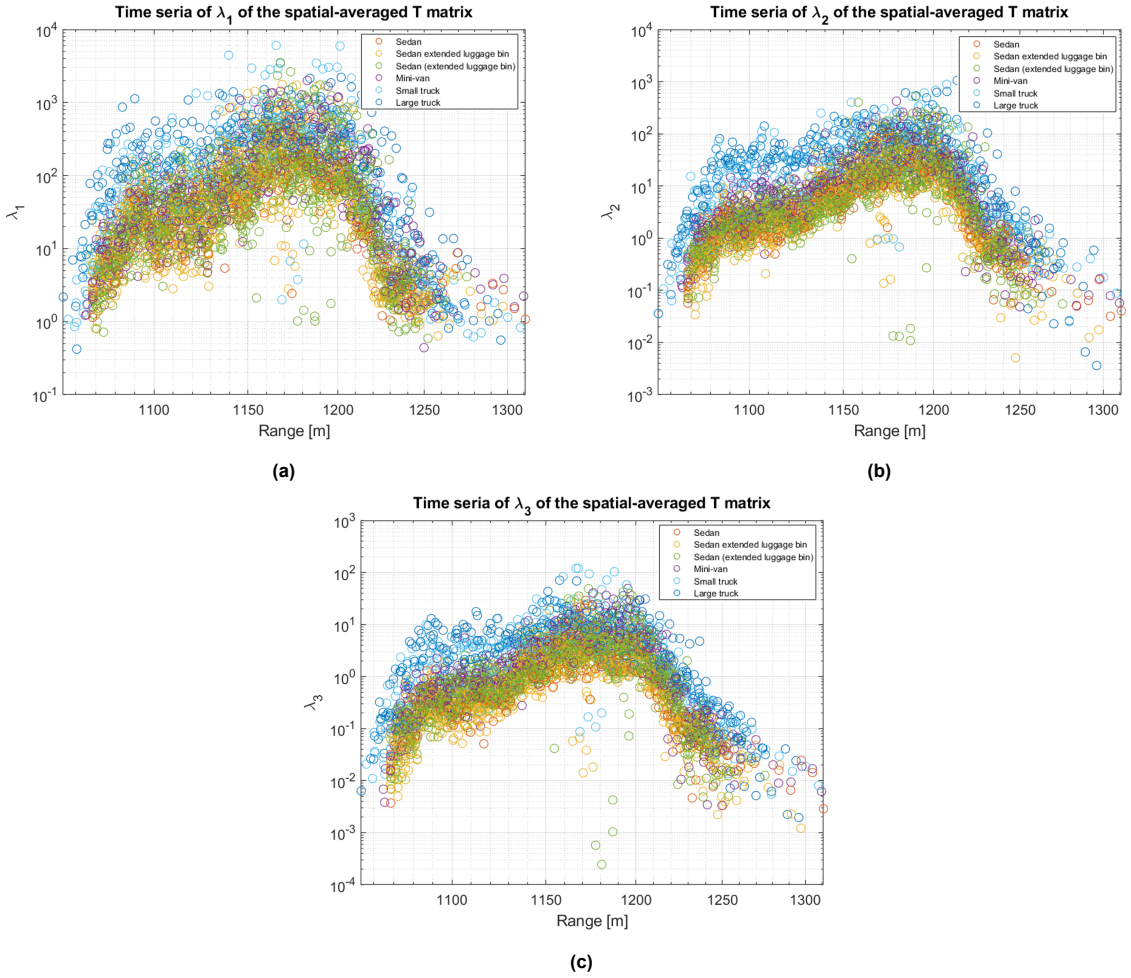

Figure 4.16: Three eigenvalues of the spatial-averaged coherency/covariance matrices of the multi-class vehicles at all time frames, where the antenna pattern effect needs to be removed before further analysis

Table 4.4: Moments of the three eigenvalues of spatial-averaged coherency/covariance matrix of the multi-class vehicles

			λ_1			
	Sedan	**Sedan with extended luggage bin**	**Sedan (with extended luggage bin)**	**Mini-van**	**Small truck**	**Large truck**
Mean	287.17	346.65	395.49	556.99	1.26×10^3	1.96×10^3
Variance	5.79×10^4	2.20×10^5	2.67×10^5	3.36×10^5	2.86×10^6	6.99×10^6
Skewness	1.59	5.25	5.35	2.45	4.28	5.48
Kurtosis	6.19	42.27	50.36	10.60	27.60	47.36
			λ_2			
	Sedan	**Sedan with extended luggage bin**	**Sedan (with extended luggage bin)**	**Mini-van**	**Small truck**	**Large truck**
Mean	45.44	51.03	64.36	105.16	277.70	456.78
Variance	2.17×10^3	3.68×10^3	1.05×10^4	1.11×10^4	1.19×10^5	4.60×10^5
Skewness	3.16	5.99	11.15	3.28	4.52	9.50
Kurtosis	15.84	67.80	199.23	20.70	33.24	126.33
			λ_3			
	Sedan	**Sedan with extended luggage bin**	**Sedan (with extended luggage bin)**	**Mini-van**	**Small truck**	**Large truck**
Mean	6.40	7.07	9.68	13.90	31.82	49.35
Variance	39.44	52.66	94.23	163.41	970.73	2.61×10^3
Skewness	3.76	3.96	4.42	3.39	2.47	3.74
Kurtosis	24.07	28.64	36.84	23.51	11.15	24.85

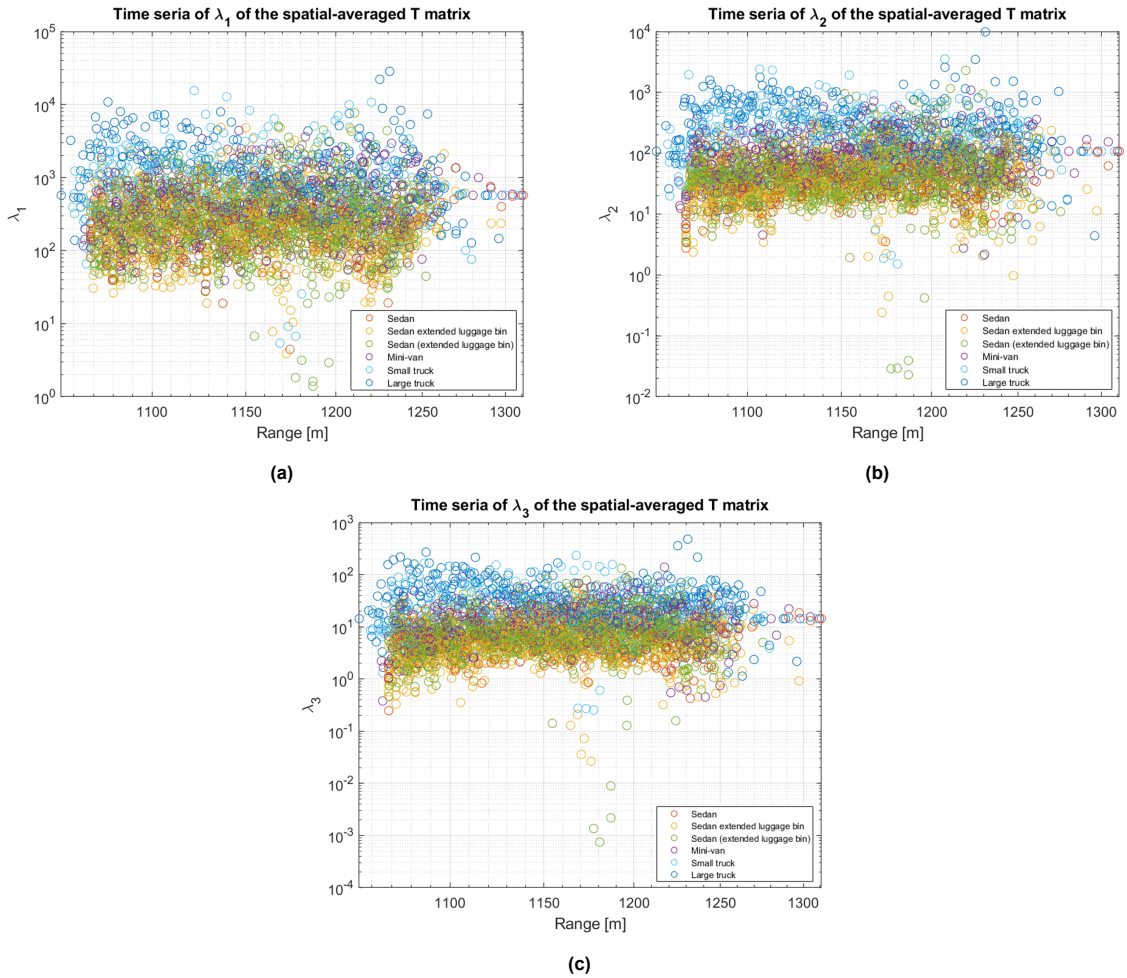

Figure 4.17: Three eigenvalues of the spatial-averaged coherency/covariance matrices of the multi-class vehicles at all time frames after antenna pattern compensation, which correspond to the reflection power of the vehicles' three deterministic scattering mechanisms

The nine features are extracted for each vehicle and form five feature spaces. Since the feature spaces look similar to the previous results in the non-averaged **T** or **C** matrix case (Figure 4.13 and Figure 4.14), the figures are not presented here, and they can be found in Appendix D.1. Furthermore, the Silhouette coefficients of the features are calculated for each class pair to evaluate these features' clustering performances, as shown in Figure 4.19. The definition of the Silhouette coefficient has been elaborated in Sub-section 4.1.2. Knowing a higher Silhouette coefficient corresponds to a better clustering performance, the following conclusions can be summarized from Figure 4.19:

1. Mean of λ_2 is found to be a new feature in classifying multi-class sedans. Standard deviation of λ_2 also contributes to classifying sedans and sedans (with extended luggage bins).
2. It is possible to classify sedans and mini-vans using standard deviation of λ_1 and mean of λ_2.
3. The multi-class sedans can be easily distinguished from small/large trucks using the mean, standard deviation, and kurtosis of λ_1 and λ_2, with most Silhouette coefficients close to 1. Even the smallest Silhouette coefficient achieves 0.8518.
4. Mean and standard deviation of λ_3 also help classify sedans and large trucks. The Silhouette coefficients are 0.9312 and 0.882, respectively.
5. Mean, standard deviation, and kurtosis of λ_1 and λ_2 contribute a lot to classifications of mini-vans

and small/large trucks as well.

6. None of the nine features performs well in classifying the sedans with extended luggage bins and mini-vans. The same conclusions are drawn in the sedan (with extended luggage bin) vs. mini-van pair and small truck vs. large truck pair.

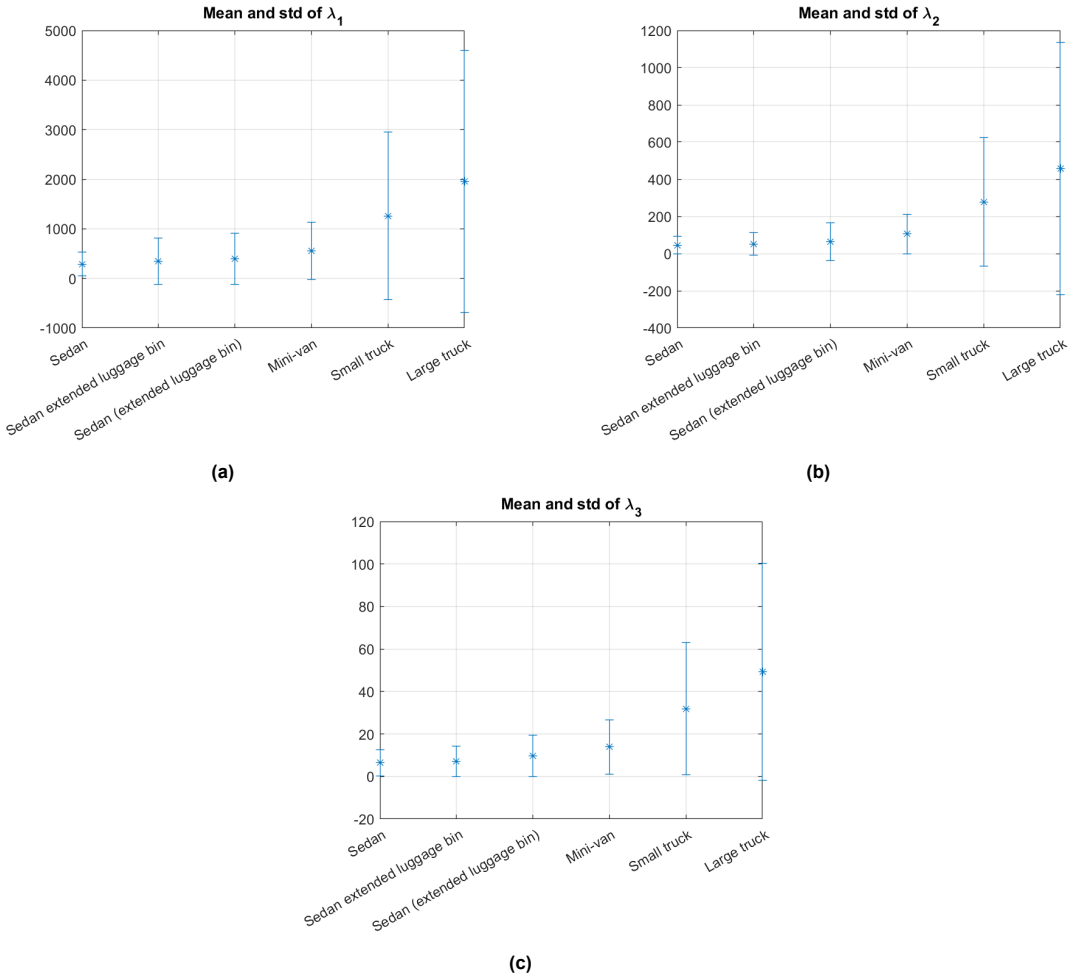

Figure 4.18: Obvious difference in mean (asterisk) and standard deviation (bar length on each side of the asterisk) of the three eigenvalues of the spatial-averaged coherency/covariance matrices between the six vehicle classes: (a) the first eigenvalues; (b) the second eigenvalues; (c) the third eigenvalues

Figure 4.19: Silhouette coefficients achieved by mean, standard deviation, and kurtosis of the three eigenvalues of the spatial-averaged coherency/covariance matrices among each class pair

Polarization Angles Analysis

Using the eigenvector-based decomposition method demonstrated in Sub-section 4.2.3, the six polarization angles are derived from the three equivalent PSMs ($\mathbf{S}_1$, $\mathbf{S}_2$, $\mathbf{S}_3$) for each vehicle in both coherency and covariance matrix case. It is found that both cases have the same sets of six polarization angles. The following content will analyze the polarization angles for different vehicle classes, which characterize the polarization basis of the vehicles' three deterministic scattering mechanisms.

The two-dimensional histograms of the polarization angles corresponding to $\mathbf{S}_1$ are plotted for each vehicle class, as shown in Figure 4.20. Note that the color bar of each sub-figure is normalized due to the different number of vehicles in each class. It could be observed that for every vehicle class, the orientation angles are concentrated around $0°$ and $\pm 90°$, corresponding to horizontal and vertical orientations. The ellipticity angles focus around $0°$, relating to linear polarizations. The same observations are carried out for the polarization angles of $\mathbf{S}_2$, which have the same concentration angles but have wider distributions. The 2D-histograms are presented in Appendix D.2. Actually, the conclusions on the polarization angles of $\mathbf{S}_1$ and $\mathbf{S}_2$ are similar to those of centroid PSMs analyzed in Sub-section 4.1.3. Since the centroid PSM represents the vehicle's central body, and $\mathbf{S}_1$ corresponds to the most dominant scattering mechanism of a vehicle, it is reasonable that these two PSMs conduct the same polarization basis. These scattering characteristics can be explained by the fact that all vehicle classes have flat planes as their dominant mechanisms. The second dominant mechanisms of the vehicles are also close to flat planes. Furthermore, from the vehicle classification perspective, the conclusion is that the polarization angles of $\mathbf{S}_1$ and $\mathbf{S}_2$ do not contribute to vehicle classification.

Different observations are found in the polarization angles of $\mathbf{S}_3$. Figure 4.21 presents the two-dimensional histograms of the polarization angles of $\mathbf{S}_3$ for all vehicle classes. For the least dominant scattering mechanisms, the orientation angles focus around $\pm 45°$, and the ellipticity angles have wide distributions within $\pm 45°$. Besides, for different vehicle classes, the ellipticity angles have different concentration angles. This preliminary observation could provide potential features in vehicle classification. However, further feature extractions are not performed in this thesis due to a time limitation.

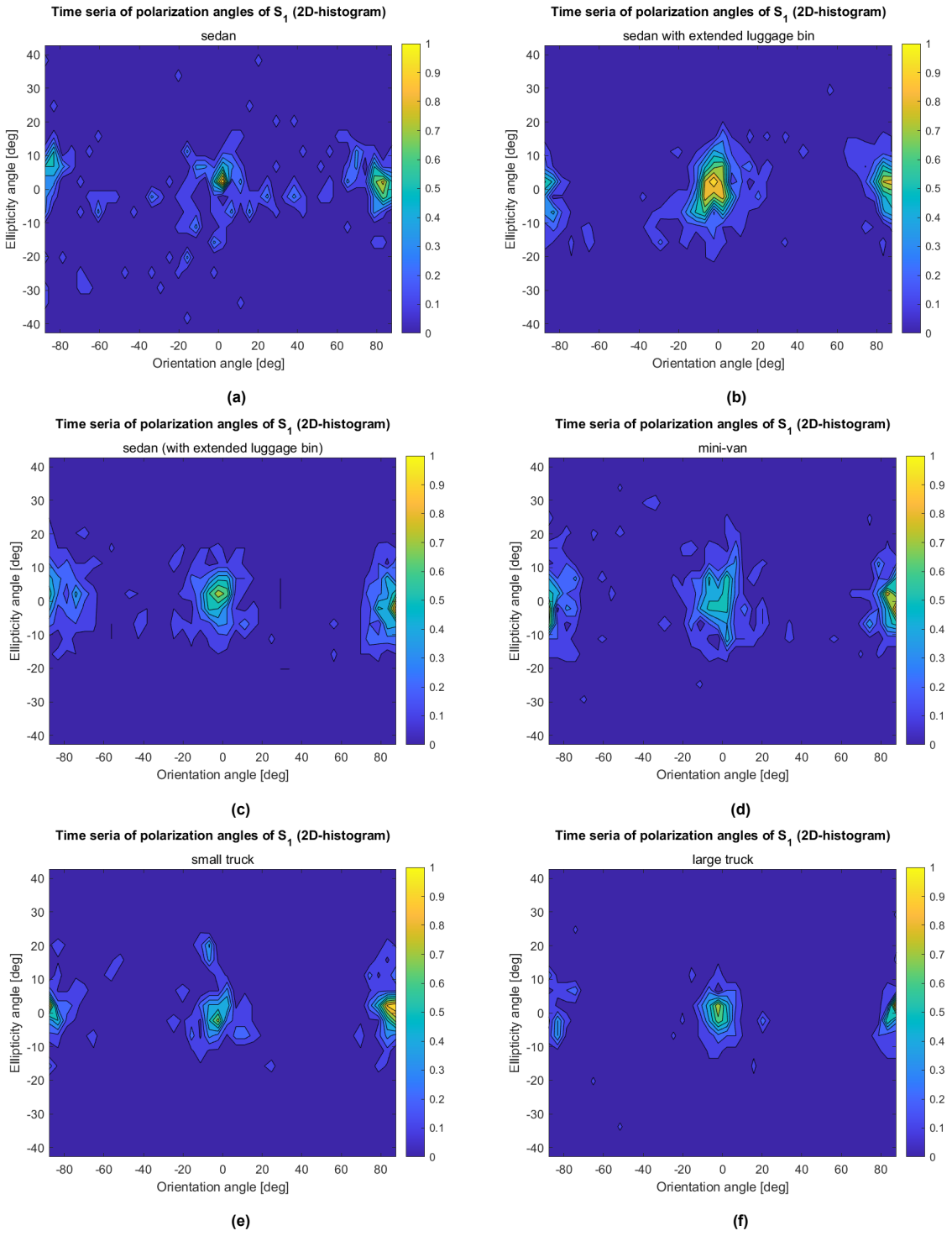

Figure 4.20: 2D-histograms of the polarization angles of the first equivalent PSMs ($\mathbf{S}_1$) of all vehicle classes at all time frames, indicating horizontal, vertical orientations and linear polarizations of the vehicles' most dominant scattering mechanisms

4.2.6. Reasons for Not Analyzing Temporal-Averaged Coherency/Covariance Matrix

The literature conducts that the **T** or **C** matrix can be averaged over space or time. In the previous sub-sections, the non-averaged and spatial-averaged **T** and **C** matrices have been analyzed over the

timeline. However, the temporal-averaged **T** or **C** matrix analysis requires averaging over the timeline, which means that each vehicle only has one temporal-averaged **T** or **C** matrix to be analyzed. The small number of vehicles (162) in the street-way database cannot provide meaningful distributions. Therefore, the temporal-averaged **T** or **C** matrix is not analyzed in this thesis.

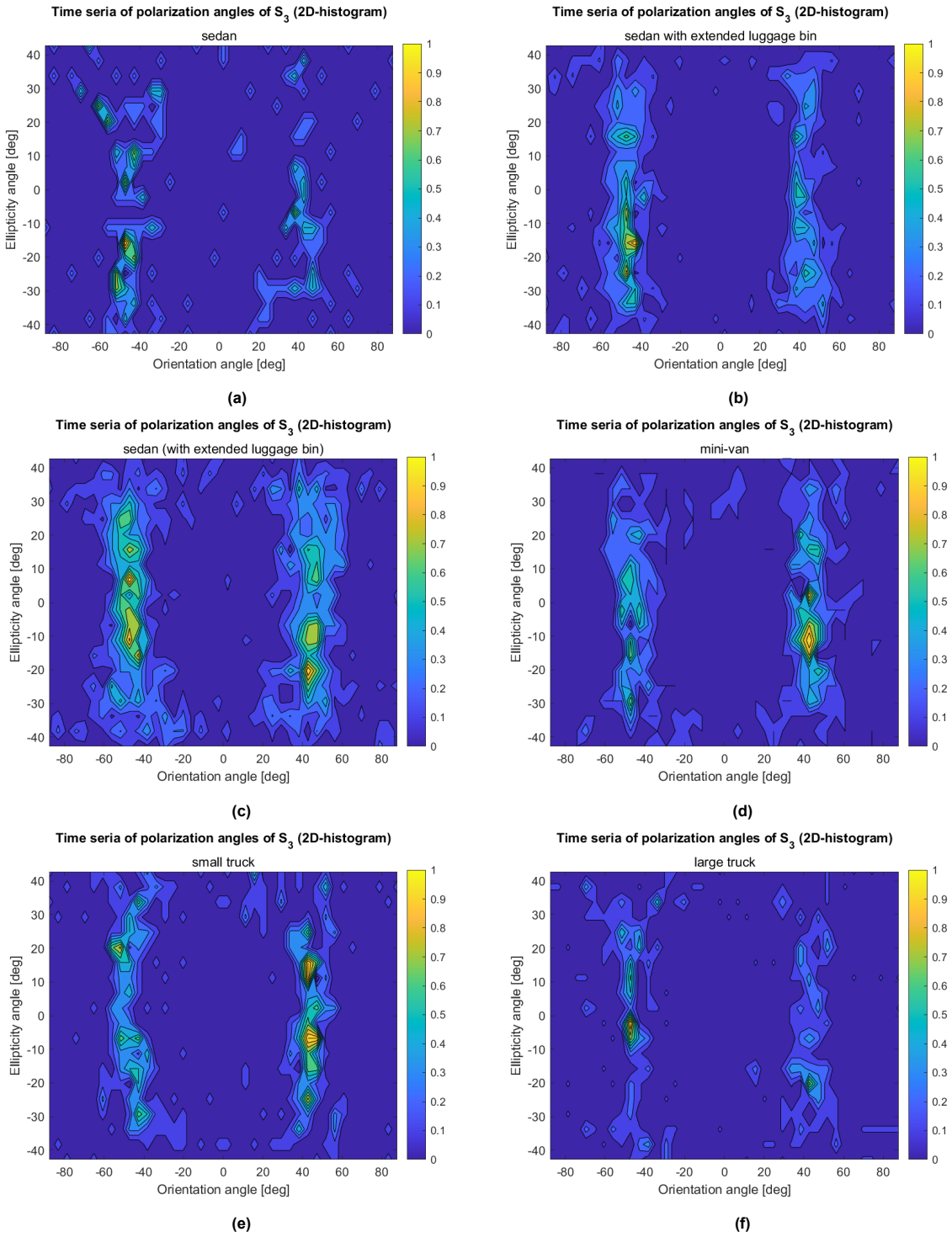

Figure 4.21: 2D-histograms of the polarization angles of the third equivalent PSMs ($\mathbf{S}_3$) of all vehicle classes at all time frames, indicating polarization basis of the least dominant scattering mechanism for each vehicle class

4.3. Target Length

The previous eigenvalues-related features have shown their great contributions to vehicle classification, and most of the eigenvalues-related features are correlated with the vehicles' sizes. In this section, the target length, which is directly related to the vehicle's size, will be extracted and evaluated for vehicle classification. The definition of the target length will be explained in Sub-section 4.3.1. Then the classification capability of the target length will be evaluated in Sub-section 4.3.2.

4.3.1. Feature Definition

Figure 4.22 presents the range-Doppler map at a time frame in target detection. The red blocks indicate the target's velocity and range boundaries. The target length of each vehicle at each time frame is then defined as the height (in meters) of the red blocks, as indicated by the yellow marks in Figure 4.22. To make the target length more representative for each vehicle, the target lengths at all time frames of each vehicle are averaged. As a result, each vehicle has an average target length, which is used in the feature evaluation in the following sub-section.

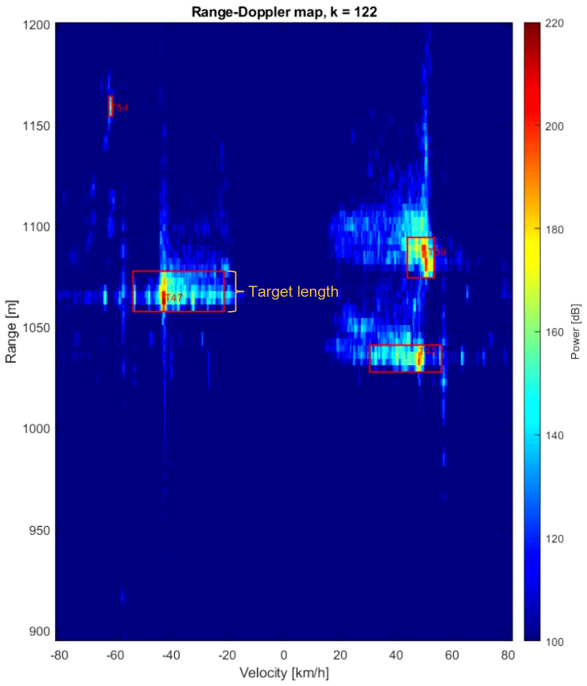

Figure 4.22: Target length extraction using target boundaries in Range-Doppler map

4.3.2. Feature Evaluation

Since there is only one feature in this section, the feature space is not plotted. The feature of target length is evaluated by calculating Silhouette coefficients among each vehicle class pair, as illustrated in Figure 4.23. The definition of the Silhouette coefficient has been elaborated in Sub-section 4.1.2. Knowing a higher Silhouette coefficient relates to a better clustering performance, the clustering performance of the target length can be concluded as follows:

1. The target length has good performance in classifying multi-class sedans or mini-vans from large trucks, with Silhouette coefficients higher than 0.85.
2. The target length also has a high Silhouette coefficient (0.8865) in the classification of sedans

with extended luggage bins and small trucks.

3. The target length does not contribute to the classifications of the other class pairs.

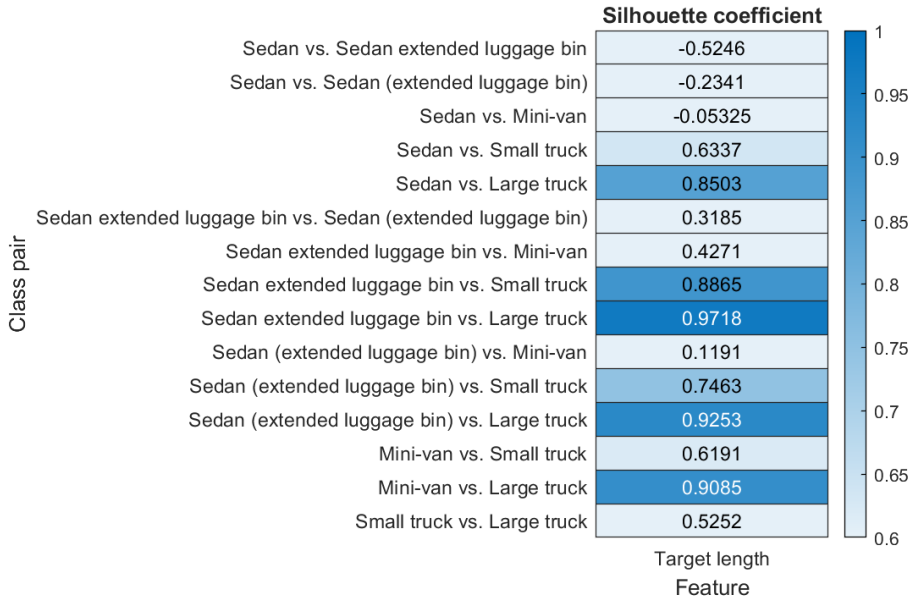

Figure 4.23: Silhouette coefficients achieved by target length among each class pair

4.4. Eigenvalues of Covariance Matrix of Detection Cells

In this section, two features proposed in [41] will be applied to the multi-class vehicles in this thesis, which are eigenvalues of the covariance matrix of detection cells. The first eigenvalue has been validated as the most important feature in road user classifications [5, 41]. In this thesis, the detection cells have different definitions. Therefore, the two eigenvalues will correspond to different physical meanings. The detailed definition will be elaborated in Sub-section 4.4.1. Then the classification capabilities of the two eigenvalues will be evaluated in Sub-section 4.4.2.

4.4.1. Feature Definition

In [41], the coordinates $(x,\ y)$ of the detection cells are defined as the horizontal and vertical distances of the targets relative to the radar. However, in this thesis, the targets are detected in the range-Doppler domain, as shown in Figure 4.24. Each red block indicates the boundary of a vehicle, and the black geometries inside the block are the clustered detection cells. The coordinates $(v,\ R)$ of the detection cells are then defined as the Doppler velocity and range information. For each target consisting of multiple detection cells, a 2×2 covariance matrix is calculated from the coordinates vectors $\vec{v}$ and $\vec{R}$. Then two eigenvalues λ_1, λ_2 are extracted from each covariance matrix. Due to the special coordinates defined in the range-Doppler domain, the resulting eigenvalues involve the target length information, target acceleration information as well as target range migration information. Note that to make the eigenvalues more representative for each vehicle, the eigenvalues at all time frames of each vehicle are averaged. As a result, each vehicle has two average eigenvalues, which are used in the feature evaluation in the following sub-section.

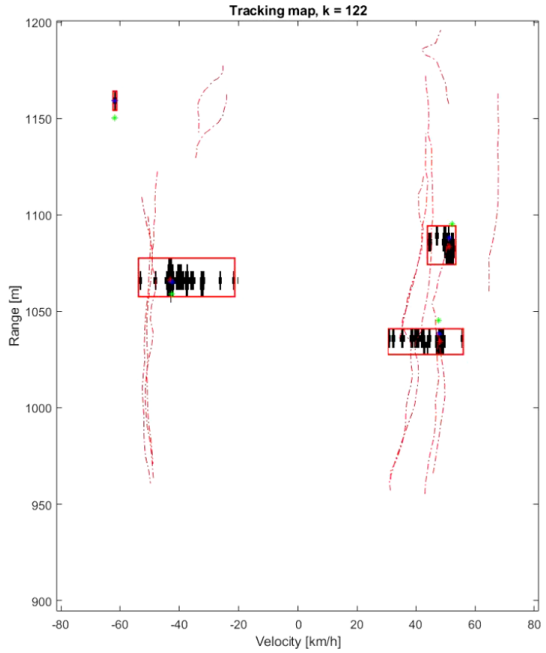

Figure 4.24: Target detection cells in range-Doppler domain, with coordinates of Doppler velocities and range information

4.4.2. Feature Evaluation

The feature space composed by the two eigenvalues is shown in Figure 4.25. The first eigenvalue λ_1 has potential vehicle classification capability, while the second eigenvalue λ_2 does not make a contribution.

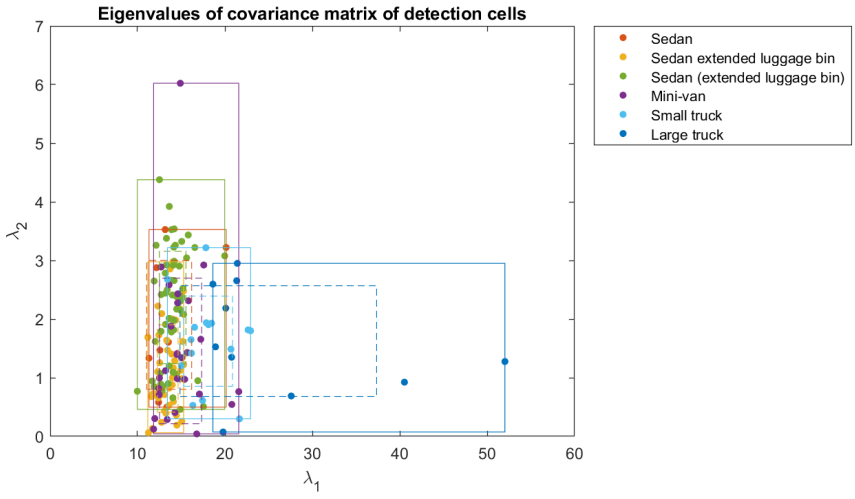

Figure 4.25: Feature space of λ_1 vs. λ_2 of covariance matrix of detection cells

To quantify the classification capabilities of the two eigenvalues, the Silhouette coefficients are calculated for each vehicle class pair, as presented in Figure 4.26. The following conclusions can be drawn on the classification performance of the two eigenvalues:

1. λ_1 makes an outstanding contribution in classifying large trucks with the other five vehicle classes. The Silhouette coefficients are higher than 0.9.

2. λ_1 can be used to classify the sedans with extended luggage bins and small trucks, with a Silhouette coefficient of 0.8919.
3. λ_2 makes no contribution to vehicle classification.

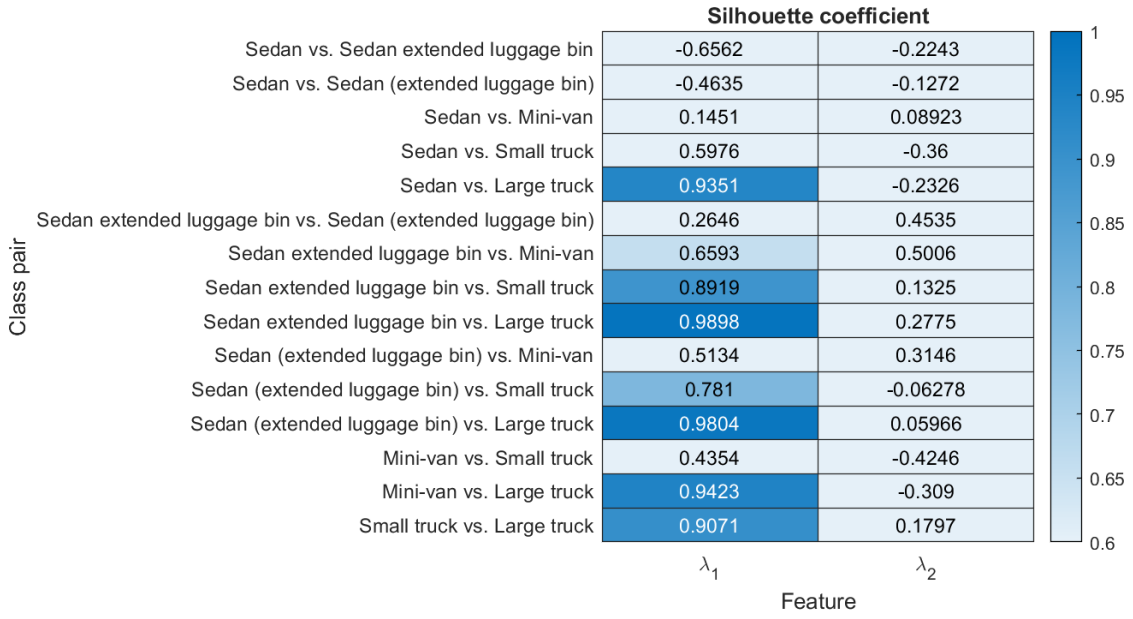

Figure 4.26: Silhouette coefficients achieved by the eigenvalues of the covariance matrix of detection cells among each class pair

4.5. Summary

This chapter focuses on feature extraction and analysis to investigate the multi-class vehicles' scattering characteristics and to identify features contributing to vehicle classification. The feature analysis starts with the centroid PSMs, which represent the polarimetric scattering characteristics of the vehicles' central bodies. The eigenvalues and eigenvectors are extracted by diagonalizing the PSMs using the Graves matrix. Then the polarization angles (orientation and ellipticity angles) are derived from the eigenvectors. The physical meanings of the eigenvalues and polarization angles are clear. The eigenvalues correspond to the vehicles' reflection amplitudes, and the polarization angles construct the polarization ellipse introduced in Sub-section 2.1.1. For the eigenvalues analysis of multi-class vehicles, the antenna pattern compensation algorithm proposed in Section 3.3 is applied first, which makes the eigenvalues more compact in further analysis. The compensated eigenvalues are dependent on the vehicles' sizes, which is consistent with the physical explanation that the central bodies of larger vehicles should have stronger reflection amplitudes. Then the distributions of the eigenvalues from different vehicle classes are demonstrated, where similar Gaussian-like distributions with a mean close to zero are found in all classes. The moments including mean, variance, skewness, and kurtosis, are calculated to statistically characterize the Gaussian-like distributions. The moments with obvious differences among the six vehicle classes are regarded as potential features for vehicle classification, which are the mean of absolute eigenvalues and the standard deviations of real, imaginary, and absolute eigenvalues. Afterward, these features are extracted from each vehicle and evaluated by the feature spaces and Silhouette coefficients. The feature spaces provide general clustering performances, and the Silhouette coefficients quantify the compactness and separability of every two vehicle classes classified by each feature. As a result, for most of the class pairs, multiple features have great classification

contributions. While for the vehicle classes with comparable sizes, these reflection amplitude-based features do not have satisfactory classification capabilities. As for the polarization angles analysis, the antenna pattern effect is checked as well. The results demonstrate that the polarization angles are not affected by the antenna pattern. Then the polarization angles are analyzed separately for the different vehicle classes. However, for all the vehicle classes, the orientation angles concentrate around 0° and $\pm 90^\circ$, and the ellipticity angles focus around 0°. The behaviors of the polarization angles of the centroid PSMs indicate the horizontal, vertical orientations and linear polarizations of the vehicles' central bodies. These scattering characteristics can be explained by the fact that all vehicle classes have flat planes as their central bodies. From the vehicle classification perspective, the polarization angles do not make contributions.

Then the analysis focuses on the coherency and covariance matrices, which are transferred from the PSM using different basis sets. The coherency and covariance matrices are defined in the monostatic backscattering case. Both matrices can be averaged over space or time to characterize the vehicle fluctuations in the dynamically changing environment. In this case, the eigenvalues and eigenvectors are derived using the standard eigen-decomposition procedure. The physical meaning of the eigenvalue corresponds to the vehicles' reflection power, and the eigenvectors are interpreted by extracting a set of six polarization angles using the eigenvector-based decomposition method. As a result, each vehicle is represented by three deterministic scattering mechanisms. The three eigenvalues specify the contributions of the three scattering mechanisms, and the six polarization angles determine the scattering types. The eigenvalues and polarization angles are analyzed for the non-averaged and spatial-averaged coherency and covariance matrices, which respectively represent the vehicles' central bodies and whole bodies. The temporal-averaged coherency and covariance matrices are not considered due to the limited number of vehicles in the database. In the non-averaged coherency/covariance matrix case, only the first eigenvalues are non-zero, and the analysis of the eigenvalues follows the same procedure as in the centroid PSM. Similar conclusions are drawn in this case: the mean and standard deviation of the first eigenvalues have great classification capabilities for most of the class pairs. However, these reflection power-related features do not contribute to classifying the vehicle classes with comparable sizes. In addition, the kurtosis of the first eigenvalues is also found to be contributed in some of the class pairs. The polarization angles are not analyzed in this case since they are the same as in the centroid PSM case. For the spatial-averaged coherency/covariance matrix case, three eigenvalues are non-zero and non-equal. A similar eigenvalues analysis procedure is performed, resulting in more features based on the mean, standard deviation, and kurtosis of the three eigenvalues. Similarly, these power-related features perform well in most of the class pairs, while classifying some of the class pairs with comparable sizes still remains an issue. As for the polarization angles, the analysis demonstrates that the most and second dominant scattering mechanisms of all vehicle classes have the same behavior as in the centroid PSM case, where horizontal, vertical orientations and linear polarizations are found. Nevertheless, the least dominant scattering mechanisms result in different distributions of the ellipticity angles, which might lead to potential features in vehicle classification.

Inspired by the previously found features that are closely related to the vehicles' reflection amplitude/power (i.e., actually the vehicles' sizes), the target length is extracted to be a new feature. The target length is defined as the range boundary of each vehicle in the range-Doppler map, averaged over the time frames. The Silhouette coefficients are calculated in this case as well for the feature evaluation. The target length achieves satisfactory Silhouette values in distinguishing small and large trucks from the other vehicle classes.

Finally, two more features that are also related to the vehicles' sizes are extracted and evaluated, which are the two eigenvalues of the covariance matrix of detection cells. The covariance matrix of each vehicle at every time frame is calculated from the coordinates vectors $\vec{v}$ and $\vec{R}$ of the detection

cells in the range-Doppler map. The eigenvalues derived from the covariance matrix are averaged over the vehicles' time frames. Both the feature space and the Silhouette coefficients indicate that the first eigenvalue has classification capabilities in some of the vehicle class pairs. However, the second eigenvalue makes no contribution to vehicle classification.

All the features that achieve Silhouette coefficients higher than 0.8 are summarized in a table in Appendix E.1. The features are listed for each class pair, and the Silhouette coefficients are presented in the brackets after the features to indicate their classification performances. It could be concluded that multiple features have been found for most of the vehicle class pairs. Only two class pairs cannot be classified using the proposed features, which are sedan with extended luggage bin vs. sedan (with extended luggage bin) and sedan (with extended luggage bin) vs. mini-van. These limitations are further discussed in the thesis recommendations in Section 5.2.

5

Conclusion and Recommendations

In this chapter, the conclusions of this thesis are drawn in Section 5.1. Then based on the results of this thesis, several recommendations are proposed in Section 5.2 for potential future research.

5.1. Conclusion

Accurate vehicle classification plays a critical role in traditional advanced driver assistant systems, rapidly developing autonomous driving systems, and vehicle traffic monitoring systems. Current research has revealed the benefits of utilizing additional polarimetric information captured by the automotive polarimetric radars in the road target classification. Potential features have been proposed in discriminating different vehicle segments and defining vehicle sub-classes. This thesis mainly investigates the polarimetric characteristics of multi-class vehicles (sedan, sedan with extended luggage bin, mini-van, small truck, and large truck) and explores new features contributing to vehicle classification. This research is supported by a labeled database extracted from over 150 vehicles driving on Schoemakerstraat near the TU Delft campus. The real-world measurements are captured by the PARSAX S-band Doppler polarimetric frequency modulated continuous wave radar.

This thesis starts with developing algorithms for calibrating the labeled street-way database to ensure feature quality. Three calibration algorithms are being proposed to deal with the issues caused by the PARSAX radar's hardware characteristics and measurement settings:

- **Channel calibration algorithm:** A novel noise-based polarimetric radar calibration algorithm is implemented to remove the channel-specific amplification factors and biases caused by the non-ideal and non-identical electronic devices in the four polarimetric channels of the PARSAX radar. The algorithm is validated on the noise data, and the calibrated noise data in the four channels present perfect independence and have the same distribution range. Then the equivalence of applying the calibration algorithm to the radar raw data and the Doppler processed data is proven, providing the feasibility of directly calibrating the labeled street-way database, significantly decreasing the workload of re-processing and re-labeling the street-way measurements.
- **Phase compensation algorithm:** Due to the time shift between the transmitted H- and V-polarized signals, a phase difference appears between the H- and V-polarized channels when measuring moving vehicles. The phase difference is linearly dependent on the target's velocity. A phase compensation algorithm is introduced and applied to the street-way database. The

elements S_{VH} and S_{VV} in the PSM are compensated. The compensation results meet the reciprocity theorem and indicate the removal of the linear dependence between the phase difference and the target's velocity. In addition, the algorithm is extended to the ambiguous velocity case for the potential future analysis of the highway database.

- **Antenna pattern compensation algorithm:** Considering the close observation ranges when measuring street-way vehicles, the azimuth angle range of the observed area is larger than the PARSAX antenna beam width, which leads to power degradation in the measurements. An antenna pattern compensation algorithm is proposed to be applied after further feature extractions, leading to more compact results in the feature analysis.

All the previously implemented calibration algorithms provide the possibility of analyzing the features extracted from the PSM, coherency matrix, and covariance matrix using the eigenvalues/eigenvectors decomposition methods. In addition, the target length and eigenvalues of the covariance matrix of detection cells are also identified as good feature candidates. The feature extractions and analysis results can be concluded as follows:

- **Eigenvalues/Eigenvectors decomposition of centroid PSM:** The centroid PSMs represent the polarimetric characteristics of the vehicles' central bodies. The eigenvalues and eigenvectors are extracted by diagonalizing the PSMs using the Graves matrix. The resulting eigenvalues are firstly calibrated using the proposed antenna pattern compensation algorithm. The compensated eigenvalues present larger values for larger vehicles, which indicate the vehicles' reflection amplitudes. Potential features are found from the moments of the eigenvalues distributions of the different vehicle classes, which are the mean of absolute eigenvalues and standard deviations of real, imaginary, and absolute eigenvalues. These features are extracted from each vehicle and evaluated by the feature spaces and Silhouette coefficients. As a result, these amplitude-based features achieve Silhouette coefficients higher than 0.8 for the vehicles with distinguishable sizes. As for the eigenvectors, polarization angles are calculated from the eigenvectors to characterize the polarization states. The antenna pattern effect is checked, and the polarization angles are unaffected. The polarization angles indicate that all the vehicle classes have horizontal, vertical orientations and linear polarizations, which can be explained by the fact that all vehicle classes have flat planes as their central bodies.
- **Eigenvalues/Eigenvectors decomposition of coherency and covariance matrices:** The eigenvalues and eigenvectors of the coherency/covariance matrix represent each vehicle as three deterministic scattering mechanisms. The eigenvalues specify the contributions of the three deterministic scattering mechanisms, and the six polarization angles determine the scattering types. The analysis is performed on the non-averaged and spatial-averaged coherency and covariance matrices, representing the vehicles' central bodies and whole bodies. In the non-averaged coherency/covariance matrix case, similar conclusions are found as in the centroid PSM case. The eigenvalues correspond to the reflection power of the vehicles. Multiple power-based features are found to be contributed to vehicle classification. The polarization angles follow the same conclusions. As for the spatial-averaged coherency/covariance matrix case, more power-based features are figured out in vehicle classification. The polarization angles analysis demonstrates that all vehicle classes' most and second dominant scattering mechanisms have horizontal, vertical orientations and linear polarizations. Nevertheless, the least dominant scattering mechanisms result in different distributions of the ellipticity angles for different vehicle classes. Due to a time limitation, further feature extraction is not performed on the ellipticity angles.
- **Target length:** Inspired by the previously found amplitude/power-based features, target length is extracted as a new feature. The target length is defined as the range boundary of each vehicle

in the range-Doppler map, averaged over the time frames. The Silhouette coefficients elaborate that the classes of small and large trucks can be easily distinguished from the other classes.

- **Eigenvalues of covariance matrix of detection cells:** The covariance matrix of each vehicle at every time frame is calculated from the coordinates vectors $\vec{v}$ and $\vec{R}$ of the detection cells in the range-Doppler map. The eigenvalues derived from the covariance matrix are averaged over the vehicles' time frames. The eigenvalues involve the target size, acceleration, and range migration information. The silhouette coefficients indicate that the first eigenvalue contributes to vehicle classification while the second eigenvalue does not.

5.2. Recommendations

Based on the results of this thesis, several recommendations could be conducted for potential future research. Firstly, as demonstrated in Figure 4.9, the orientation angle provides polarization information in the measurement setting, which can be useful for developing a polarization basis correction algorithm. Applying this algorithm to the database can further improve the feature quality in potential future research.

Furthermore, as summarized in Table E.1, most vehicle class pairs have multiple features with satisfactory classification capabilities. However, there are two class pairs not being able to be classified using the proposed features. These unclassified classes might belong to the same class, for example, the sedan with extended luggage bin and the sedan (with extended luggage bin). The discrimination of these two classes is due to the vague video records, which might be unnecessary.

Moreover, most of the proposed features are amplitude-related or power-related. Thus, correlations can be found among these features. Not all the proposed features are necessary to be applied in the same classifier. The features can be ranked and selected in future classifier development.

In addition, when analyzing the spatial-averaged coherency and covariance matrices, it has been concluded that the least dominant scattering mechanisms of different vehicle classes have different distributions in ellipticity angles. However, further feature explorations are not proceeded due to a time limitation. Thus, future analysis can be focused on the polarization basis of the least dominant scattering mechanisms.

Finally, this thesis does not analyze the time-averaged coherency and covariance matrices due to the small number of vehicles in the database. If the database includes massive vehicles in the future, the analysis can also be performed on the time-averaged coherency and covariance matrices to investigate the vehicles' temporal fluctuating polarimetric characteristics.

References

[1] Maria Antonia Maisto et al. “A Single-Snapshot MUSIC Algorithm for ADAS Radar Processing”. In: *2022 Microwave Mediterranean Symposium (MMS)*. 2022, pp. 1–6. DOI: 10.1109/MMS55062.2022.9825498.

[2] Rasheed Hussain and Sherali Zeadally. “Autonomous Cars: Research Results, Issues, and Future Challenges”. In: *IEEE Communications Surveys & Tutorials* 21.2 (2019), pp. 1275–1313. DOI: 10.1109/COMST.2018.2869360.

[3] Xiuzhang Cai, Michael Giallorenzo, and Kamal Sarabandi. “Machine Learning-Based Target Classification for MMW Radar in Autonomous Driving”. In: *IEEE Transactions on Intelligent Vehicles* 6.4 (2021), pp. 678–689. DOI: 10.1109/TIV.2020.3048944.

[4] Jianwen Wang et al. “Vehicle Classification via Multi-dimension Feature Extraction with Millimeter Wave Radar”. In: *2021 CIE International Conference on Radar (Radar)*. 2021, pp. 1336–1339. DOI: 10.1109/Radar53847.2021.10028469.

[5] Julius F. Tilly et al. “Road User Classification with Polarimetric Radars”. In: *2020 17th European Radar Conference (EuRAD)*. 2021, pp. 112–115. DOI: 10.1109/EuRAD48048.2021.00039.

[6] Oleg A. Krasnov et al. “PARSAX: High-resolution Doppler-polarimetric FMCW radar with dual-orthogonal signals”. In: *18-th INTERNATIONAL CONFERENCE ON MICROWAVES, RADAR AND WIRELESS COMMUNICATIONS*. 2010, pp. 1–5.

[7] D.A. Bosma. “Feature Extraction of Moving Automotive Vehicles using Multi-Target Tracking on Polarimetric Doppler Radar Data”. In: (2021). Delft University of Technology, Delft, the Netherlands.

[8] Q. Zhang. “Database Creation for Automotive Targets Classification using Polarimetric Radar Measurements”. In: (2022). Delft University of Technology, Delft, the Netherlands.

[9] G. Wanielik et al. “Polarimetric millimeter wave imaging radar and traffic scene interpretation”. In: *IEE Colloquium on Automotive Radar and Navigation Techniques (Ref. No. 1998/230)*. 1998, pp. 4/1–4/7. DOI: 10.1049/ic:19980190.

[10] Tom Schipper et al. “RCS measurement results for automotive related objects at 23-27 GHz”. In: *Proceedings of the 5th European Conference on Antennas and Propagation (EUCAP)*. 2011, pp. 683–686.

[11] Kevin Geary et al. “Characterization of automotive radar targets from 22 to 29 GHz”. In: *2012 IEEE Radar Conference*. 2012, pp. 0079–0084. DOI: 10.1109/RADAR.2012.6212115.

[12] Kevin Geary et al. “Automotive radar target characterization from 22 to 29 GHz and 76 to 81 GHz”. In: *2013 IEEE Radar Conference (RadarCon13)*. 2013, pp. 1–6. DOI: 10.1109/RADAR.2013.6586128.

[13] Tristan Visentin, Jürgen Hasch, and Thomas Zwick. “Polarimetric RCS Measurements of Selected Two-Wheeled Vehicles for Automotive Radar”. In: *2017 European Radar Conference (EURAD)*. 2017, pp. 53–56. DOI: 10.23919/EURAD.2017.8249145.

[14] Michael A. Saville, Julie A. Jackson, and Dane F. Fuller. “Rethinking vehicle classification with wide-angle polarimetric SAR”. In: *IEEE Aerospace and Electronic Systems Magazine* 29.1 (2014), pp. 41–49. DOI: 10.1109/MAES.2014.130057.

[15] Julius F. Tilly et al. “Polarimetric Signatures of a Passenger Car”. In: *2019 Kleinheubach Conference*. 2019, pp. 1–4.

[16] T.L. Ainsworth, S.R. Cloude, and J.S. Lee. “Eigenvector analysis of polarimetric SAR data”. In: *IEEE International Geoscience and Remote Sensing Symposium*. Vol. 1. 2002, 626–628 vol.1. DOI: 10.1109/IGARSS.2002.1025126.

[17] B. Zakeri, A. Ghorbani, and Michele Galletti. “Statistical distribution for scattering mechanism of targets based on eigenvector decomposition in polarimetric radars”. In: *2007 European Radar Conference*. 2007, pp. 433–435. DOI: 10.1109/EURAD.2007.4405030.

[18] Riccardo Paladini, Marco Martorella, and Fabrizio Berizzi. “Classification of Man-Made Targets via Invariant Coherency-Matrix Eigenvector Decomposition of Polarimetric SAR/ISAR Images”. In: *IEEE Transactions on Geoscience and Remote Sensing* 49.8 (2011), pp. 3022–3034. DOI: 10.1109/TGRS.2011.2116121.

[19] “Basic Principles of SAR Polarimetry”. In: *Synthetic Aperture Radar Polarimetry*. John Wiley and Sons, Ltd, 2011. Chap. 2, pp. 23–72. ISBN: 9781118116104. DOI: https://doi.org/10.1002/9781118116104.ch2. eprint: https://onlinelibrary.wiley.com/doi/pdf/10.1002/9781118116104.ch2. URL: https://onlinelibrary.wiley.com/doi/abs/10.1002/9781118116104.ch2.

[20] Oleg A. Krasnov et al. “The PARSAX - full polarimetric FMCW radar with dual-orthogonal signals”. In: *2008 European Radar Conference*. 2008, pp. 84–87.

[21] T. Visentin. *Polarimetric Radar for Automotive Applications*. Creative Media Partners, LLC, 2020. ISBN: 9781013283437. URL: https://books.google.nl/books?id=a%5C_30zQEACAAJ.

[22] J.-S. Lee and E. Pottier. *Polarimetric Radar Imaging: From Basics to Applications*. 1st ed. CRC Press, 2009. DOI: https://doi.org/10.1201/9781420054989.

[23] Galina Babur. “Processing of dual-orthogonal cw polarimetric radar signals”. In: 2009.

[24] Galina P. Babur, Oleg A. Krasnov, and Leo P. Ligthart. “Quasi-simultaneous measurements of scattering matrix elements in polarimetric radar with continuous waveforms providing high-level isolation in radar channels”. In: *2009 European Radar Conference (EuRAD)*. 2009, pp. 1–4.

[25] Zhijian Li et al. “Design considerations of the RF front-end for high dynamic range digital radar receivers”. In: *MIKON 2008 - 17th International Conference on Microwaves, Radar and Wireless Communications*. 2008, pp. 1–4.

[26] D. Giuli et al. “Simultaneous scattering matrix measurement through signal coding”. In: *IEEE International Conference on Radar*. 1990, pp. 258–262. DOI: 10.1109/RADAR.1990.201173.

[27] Dino Giuli, Mario Fossi, and Luca Facheris. “Radar target scattering matrix measurement through orthogonal signals”. In: 1993.

[28] Yong Liu et al. “Instantaneous polarization measurement method based on frequency-shift-pulse-vector waveform”. In: *2009 IET International Radar Conference*. 2009, pp. 1–4. DOI: 10.1049/cp.2009.0379.

[29] Zhijian Li et al. “Optimizing two-tone spurious-free dynamic range for polarimetric agile radar receivers”. In: *2008 European Radar Conference*. 2008, pp. 336–339.

[30] Oleg A. Krasnov and Alexander Yarovoy. “Model-Based Polarimetric Radar Calibration using the Rotated Dihedral Reflector”. In: (2022). Delft University of Technology, Delft, the Netherlands.

[31] M.A. Pinsky. *Introduction to Fourier Analysis and Wavelets*. Graduate studies in mathematics. American Mathematical Society, 2008. ISBN: 9780821847978. URL: https://books.google.nl/books?id=PyISCgAAQBAJ.

[32] Fabio Weishaupt et al. “Calibration and Signal Processing of Polarimetric Radar Data in Automotive Applications”. In: *2022 Microwave Mediterranean Symposium (MMS)*. 2022, pp. 1–6. DOI: 10.1109/MMS55062.2022.9825584.

[33] NATO Advanced Research Workshop on Inverse Methods in Electromagnetic Imaging, Wolfgang M. Boerner, and North Atlantic Treaty Organization. *Inverse methods in electromagnetic imaging / edited by Wolfgang M. Boerner ... [et al.]* English. D. Reidel ; Sold, distributed in U.S.A., and Canada by Kluwer Academic Publishers Dordrecht, Holland ; Boston : Hingham, MA, U.S.A, 1985, 2 v. (xxxii, 1347 p.) : ISBN: 9027718903 9027718857 9027718881.

[34] Inverse Methods in Radar Polarimetry and Wolfgang M. Boerner. “Direct and inverse methods in radar polarimetry”. In: 1992. URL: https://api.semanticscholar.org/CorpusID:127432671.

[35] C. D. Graves. “Radar Polarization Power Scattering Matrix”. In: *Proceedings of the IRE* 44.2 (1956), pp. 248–252. DOI: 10.1109/JRPROC.1956.274912.

[36] J.R. Huynen. *Phenomenological Theory of Radar Targets*. Drukkerij Bronder-Offset N.V., 1970. URL: https://books.google.nl/books?id=LL02AQAAIAAJ.

[37] Jürgen Bernard et al. “ProSeCo: Visual analysis of class separation measures and dataset characteristics”. In: *Computers and Graphics* 96 (2021), pp. 48–60. ISSN: 0097-8493. DOI: https://doi.org/10.1016/j.cag.2021.03.004. URL: https://www.sciencedirect.com/science/article/pii/S0097849321000406.

[38] Jiawei Han, Micheline Kamber, and Jian Pei. “10 - Cluster Analysis: Basic Concepts and Methods”. In: Dec. 2012, pp. 443–495. ISBN: 9780123814791. DOI: 10.1016/B978-0-12-381479-1.00010-1.

[39] Inc. 1994-2023 The MathWorks. *eig: Eigenvalues and eigenvectors*. 2021. URL: https://www.mathworks.com/help/matlab/ref/eig.html#btg0gsa-5.

[40] S.R. Cloude and E. Pottier. “A review of target decomposition theorems in radar polarimetry”. In: *IEEE Transactions on Geoscience and Remote Sensing* 34.2 (1996), pp. 498–518. DOI: 10.1109/36.485127.

[41] Ole Schumann et al. “Comparison of random forest and long short-term memory network performances in classification tasks using radar”. In: *2017 Sensor Data Fusion: Trends, Solutions, Applications (SDF)*. 2017, pp. 1–6. DOI: 10.1109/SDF.2017.8126350.

A

Channel Calibration

A.1. Histograms of Non-Calibrated and Calibrated Noise Signals (Imaginary Part)

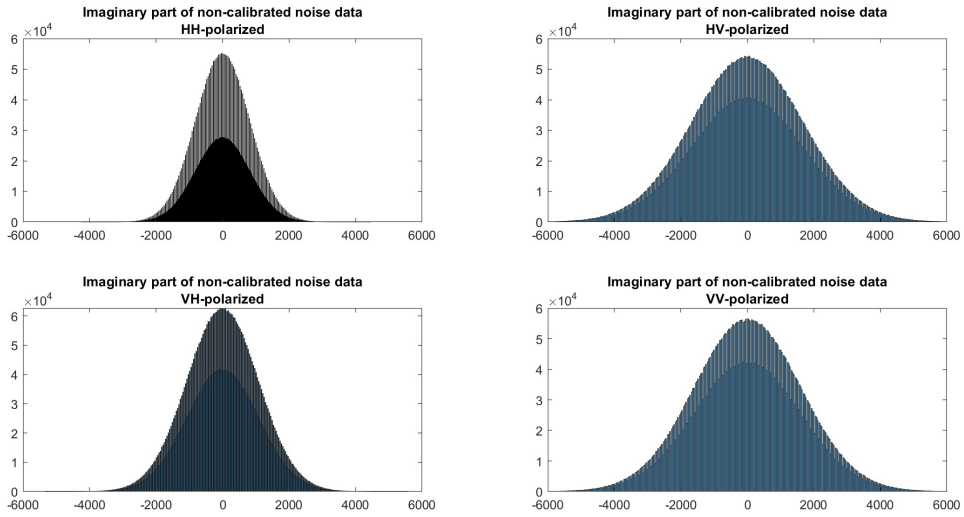

(a)

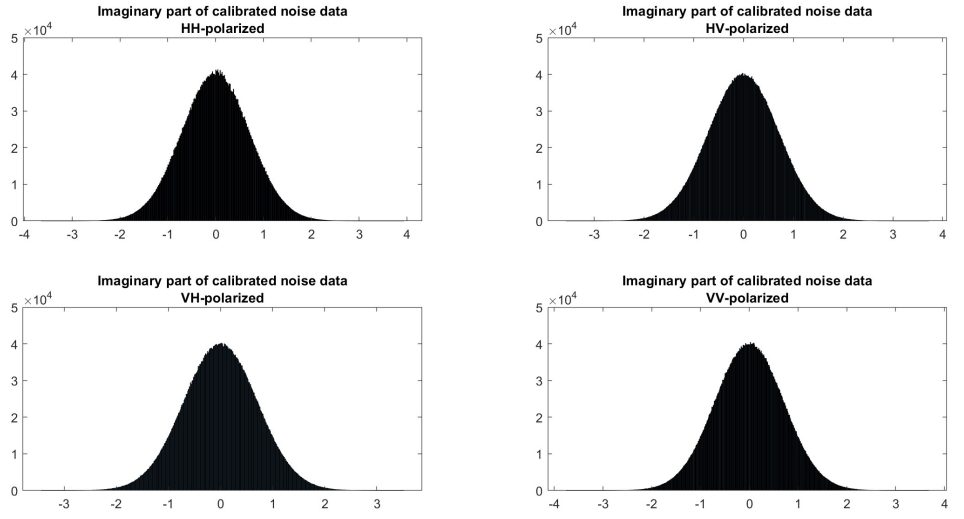

(b)

Figure A.1: Histograms of (a) non-calibrated noise data (imaginary part) and (b) calibrated noise data (imaginary part) of the four polarimetric channels, indicating that the channel-specific amplification factors are removed

B

Phase Compensation

B.1. Phase Compensation Results on S_{VV} in the Street-Way Measurements

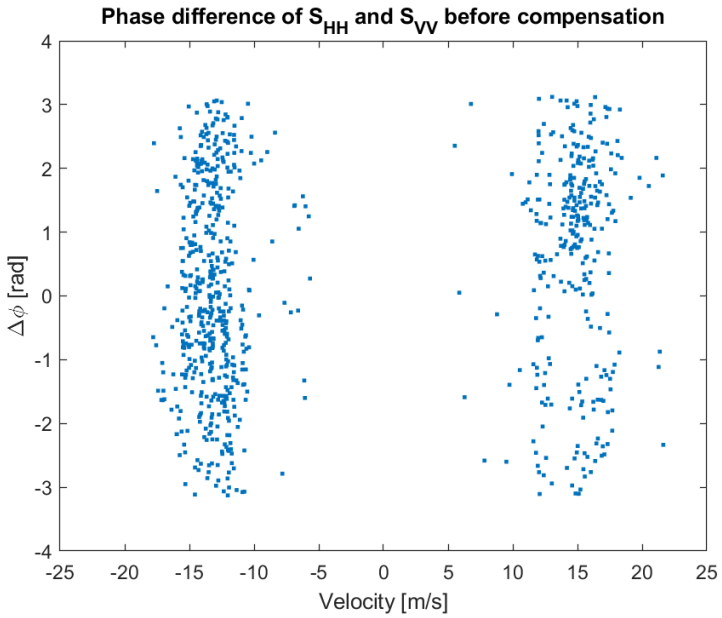

Figure B.1: Phase difference of S_{HH} and S_{VV} in the street-way case

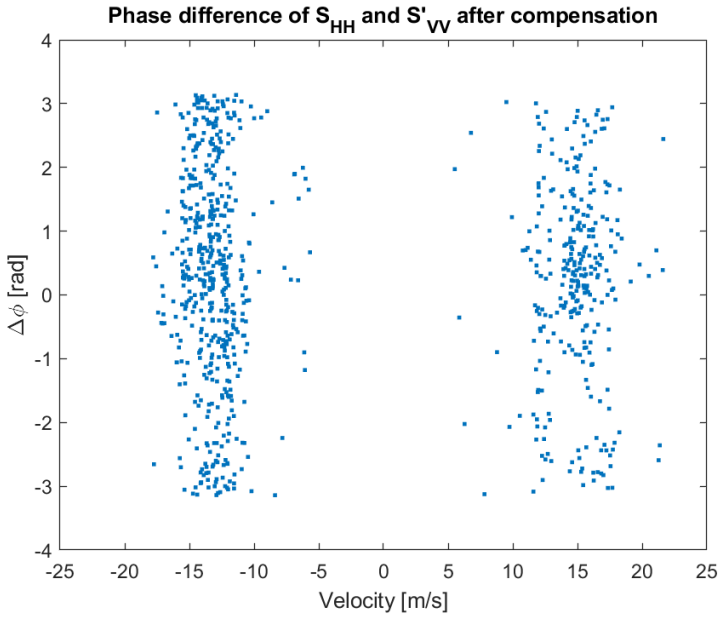

Figure B.2: Compensated phase difference of S_{HH} and S'_{VV} in the street-way case

B.2. Phase Compensation Results on S_{VV} in the Highway Measurements

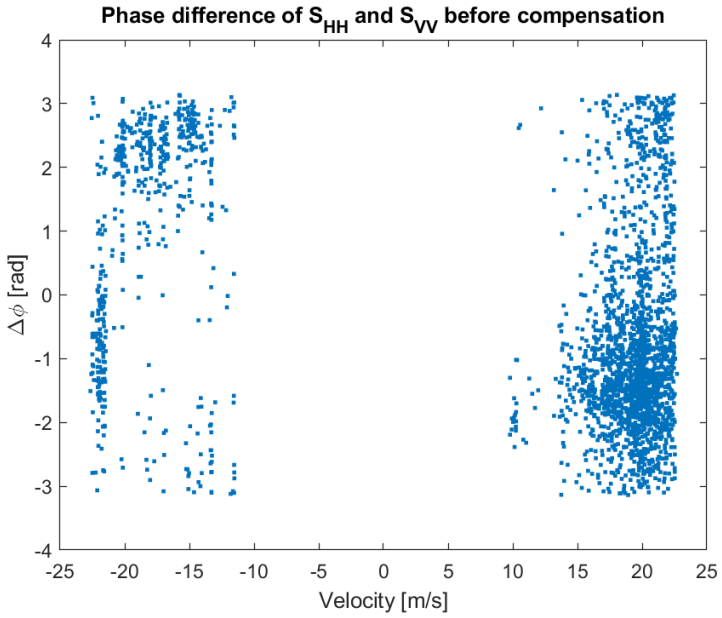

Figure B.3: Phase difference of S_{HH} and S_{VV} in the highway case

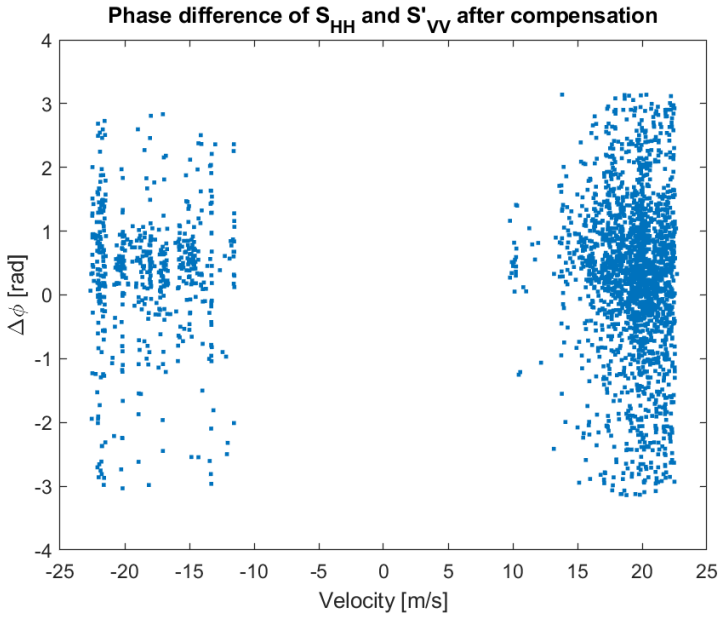

Figure B.4: Compensated phase difference of S_{HH} and S'_{VV} in the highway case

C

Eigenvalues/Eigenvectors of Centroid PSM

C.1. Eigenvalues of the Centroid PSMs of the Six Classes of Vehicles

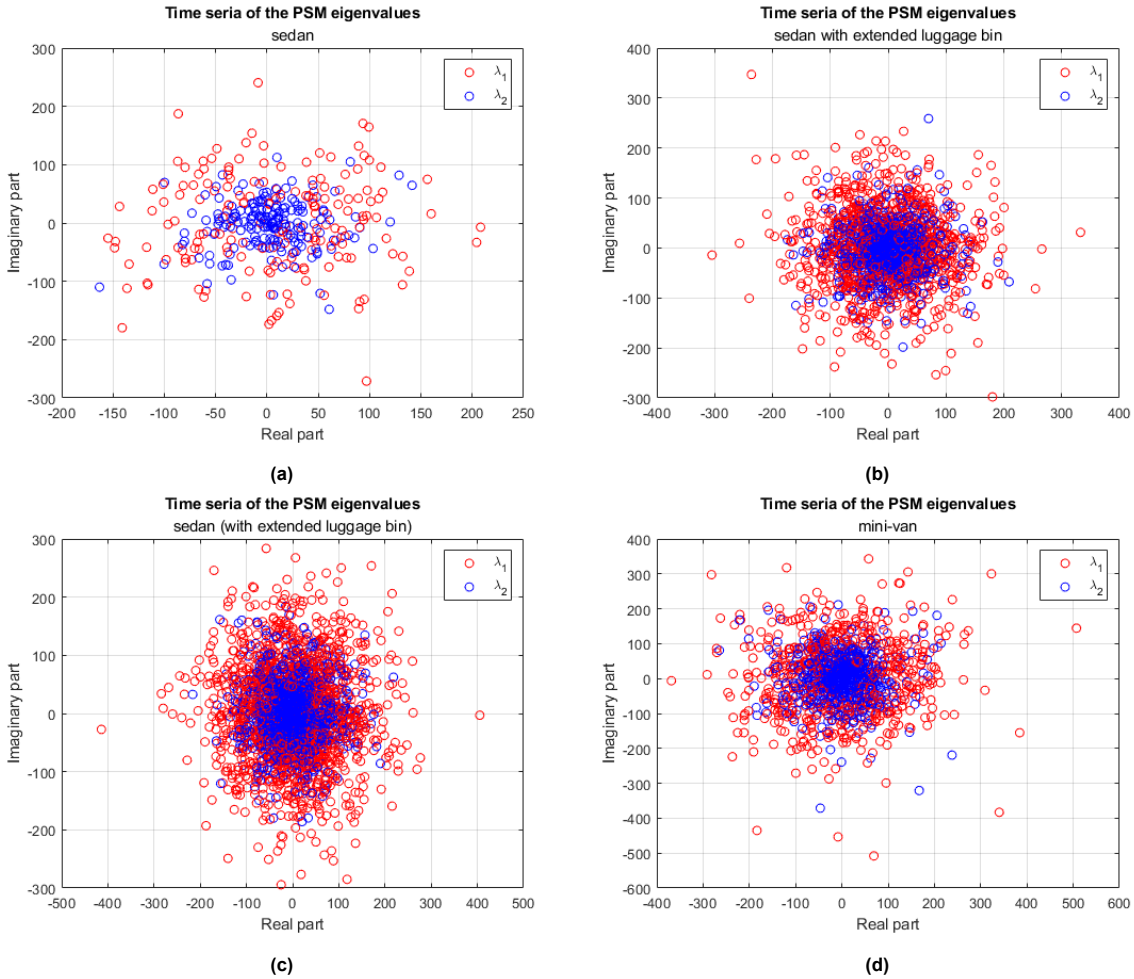

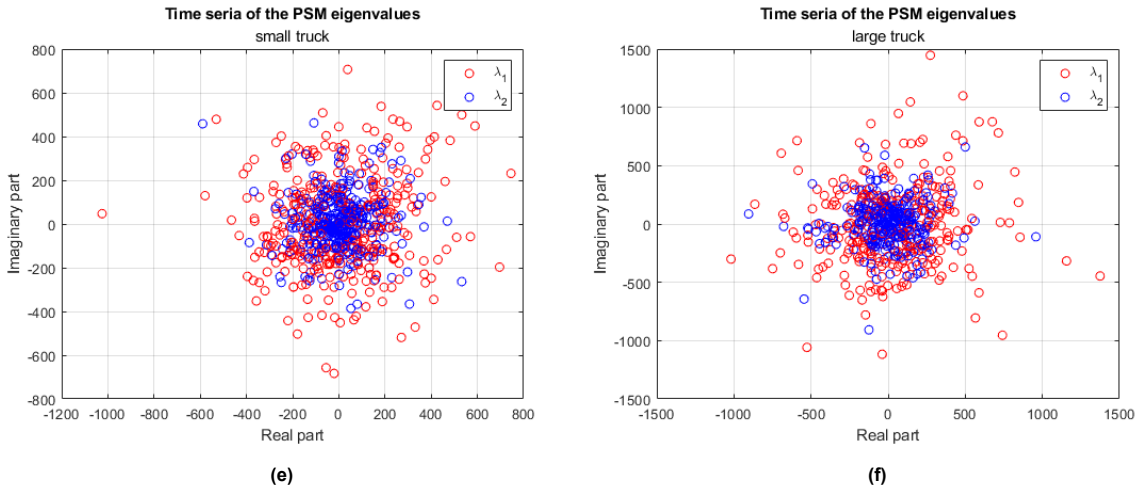

(e) (f)

Figure C.1: Eigenvalues (real and imaginary parts) of the centroid PSMs of the six classes of vehicles at all time frames, which form Gaussian-like distributions with mean close to zero: (a) sedan; (b) sedan with extended luggage bin; (c) sedan (with extended luggage bin); (d) mini-van; (e) small truck; (f) large truck

C.2. Feature Spaces of Mean and Standard Deviation of the Eigenvalues of the Centroid PSMs

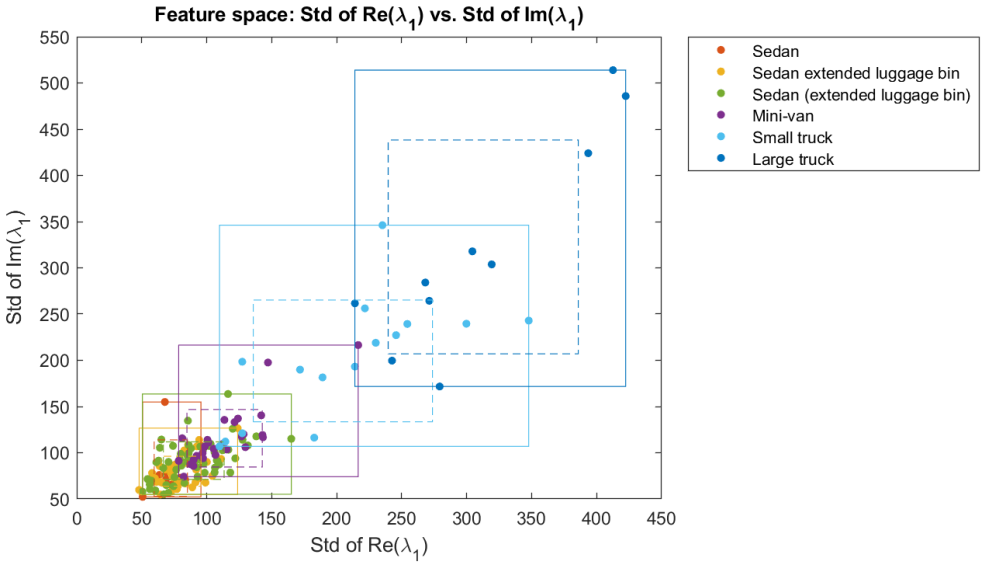

Figure C.2: Feature space of standard deviation of λ_1 (real part) vs. standard deviation of λ_1 (imaginary part), where λ_1 is the first eigenvalue of the centroid PSM

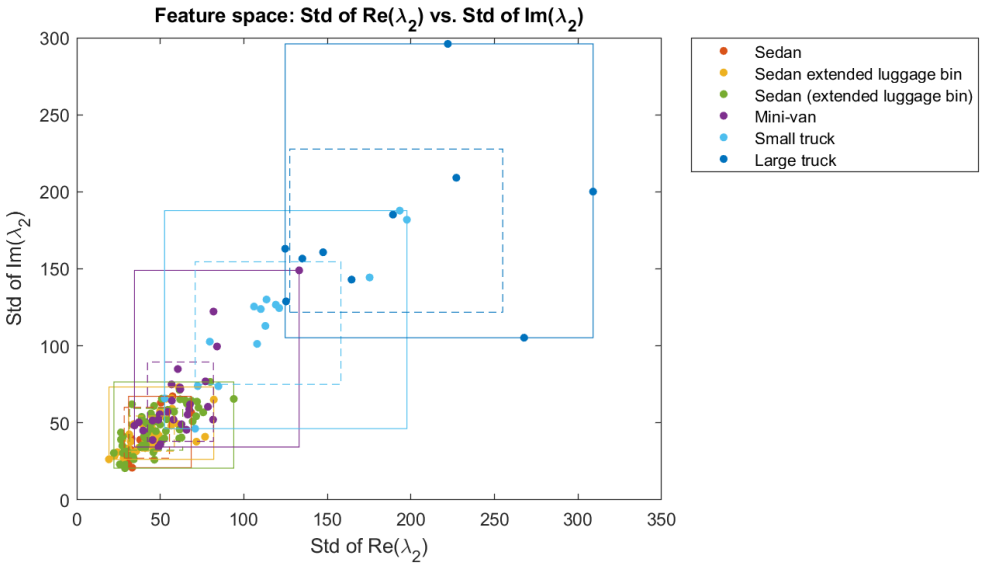

Figure C.3: Feature space of standard deviation of λ_2 (real part) vs. standard deviation of λ_2 (imaginary part), where λ_2 is the second eigenvalue of the centroid PSM

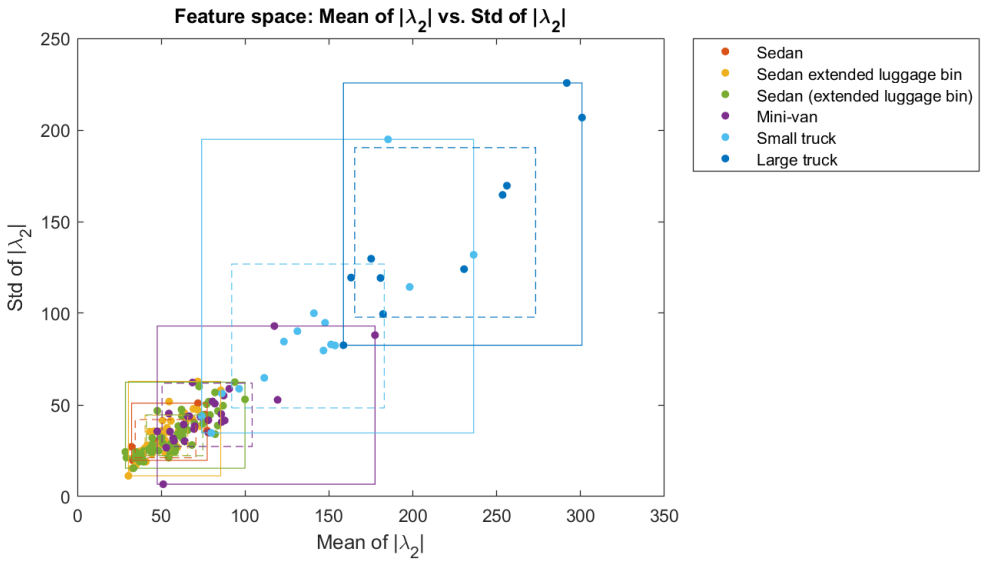

Figure C.4: Feature space of mean of λ_2 (absolute) vs. standard deviation of λ_2 (absolute), where λ_2 is the second eigenvalue of the centroid PSM

C.3. Polarization Angles of the Second Eigenvectors of the Centroid PSMs

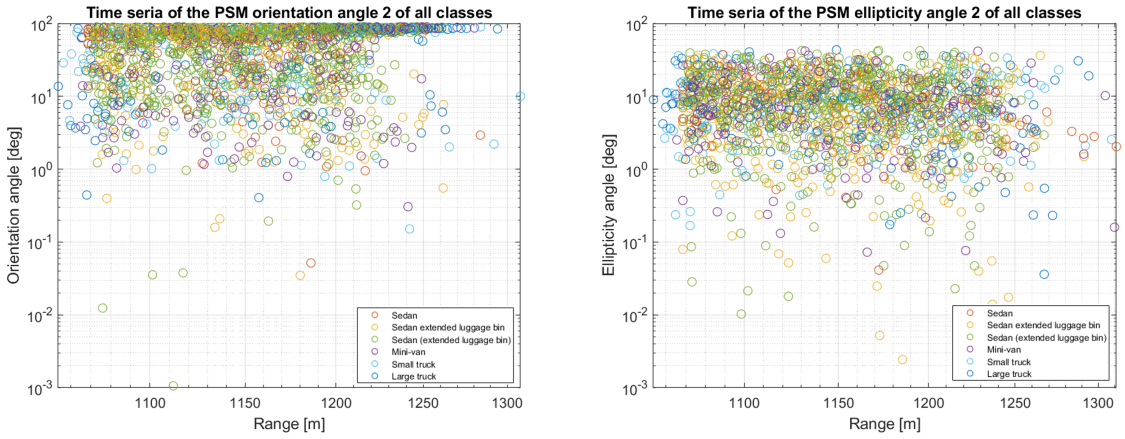

Figure C.5: Polarization angles: (a) orientation angles of the second eigenvectors; (b) ellipticity angles of the second eigenvectors of the centroid PSMs of the multi-class vehicles at all time frames, which are not affected by the antenna pattern

C.4. Polarization Angles of the First Eigenvectors of the Centroid PSMs of the Six Classes of Vehicles

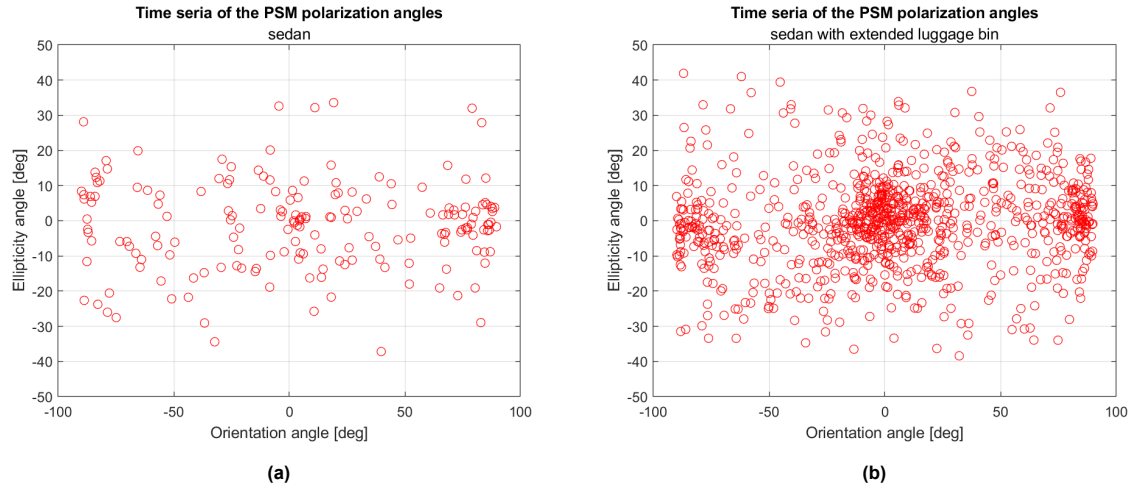

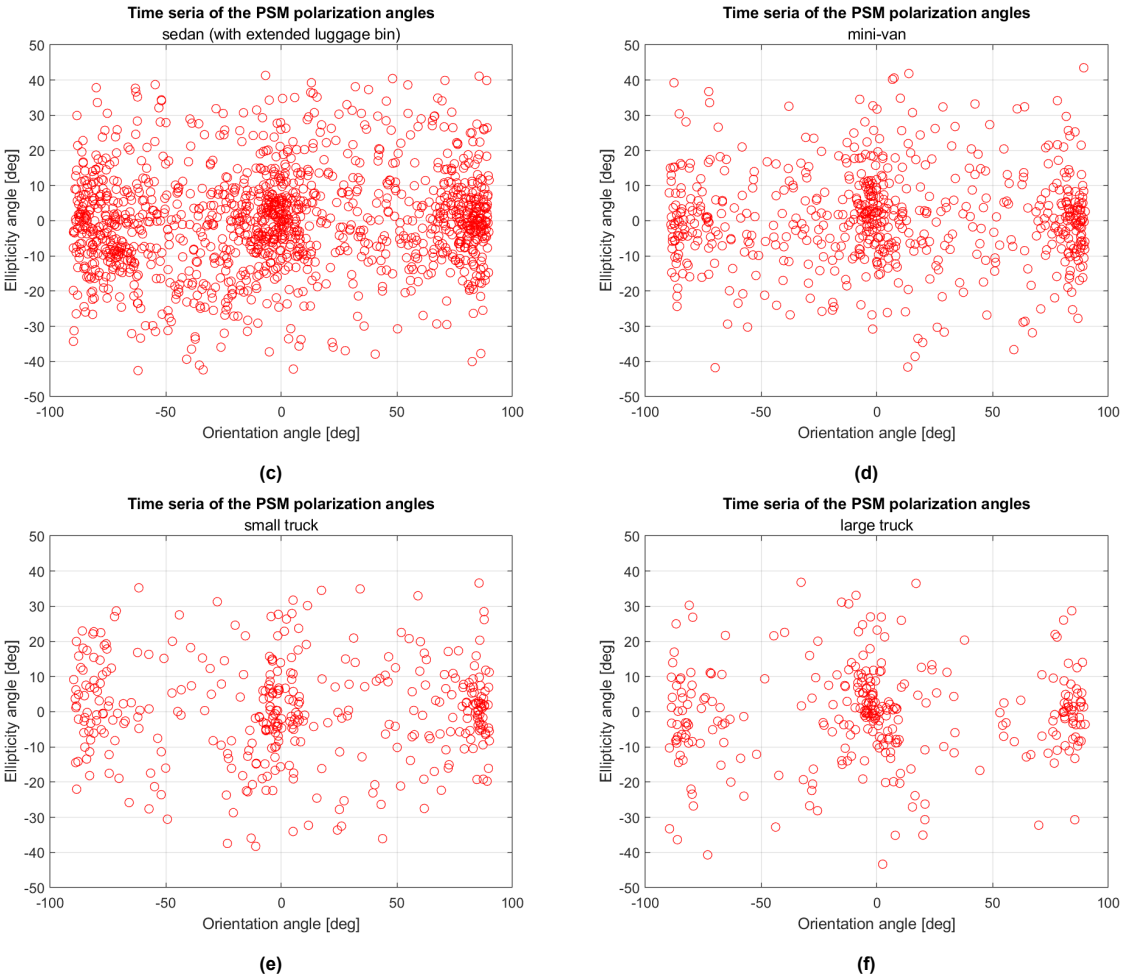

Figure C.6: Polarization angles of the first eigenvectors of the centroid PSMs of the six classes of vehicles at all time frames: (a) sedan; (b) sedan with extended luggage bin; (c) sedan (with extended luggage bin); (d) mini-van; (e) small truck; (f) large truck

D

Eigenvalues/Eigenvectors of Coherency/Covariance Matrix

D.1. Feature Spaces of Mean, Standard Deviation, and Kurtosis of the Three Eigenvalues of the Spatial-Averaged Coherency/Covariance Matrices

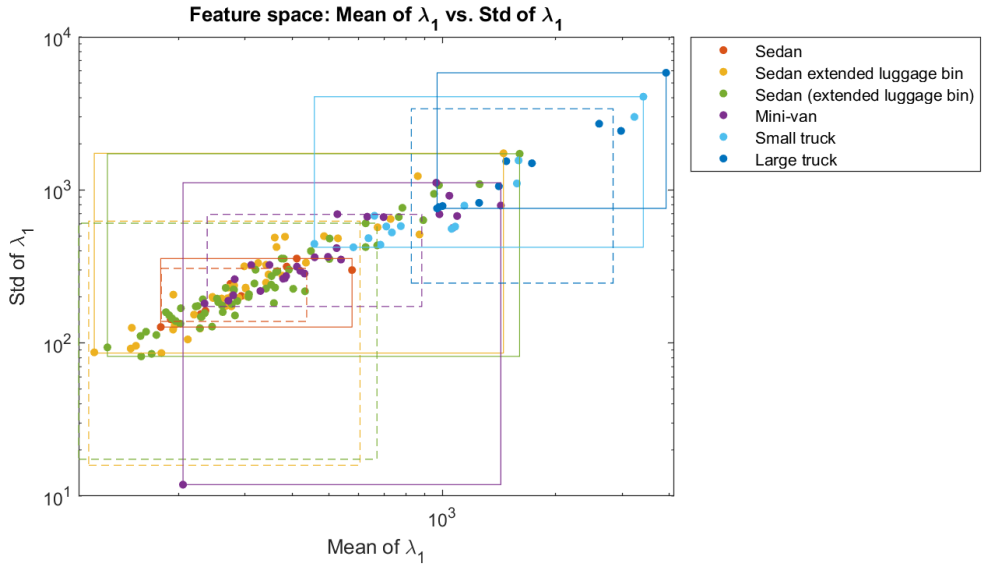

Figure D.1: Feature space of mean of λ_1 vs. standard deviation of λ_1, where λ_1 is the first eigenvalue of the spatial-averaged coherency/covariance matrix

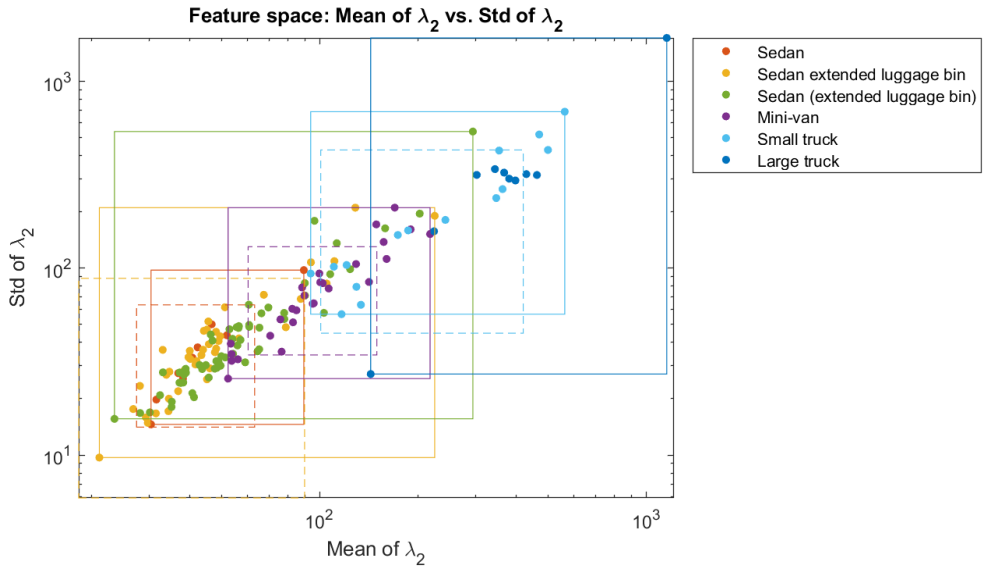

Figure D.2: Feature space of mean of λ_2 vs. standard deviation of λ_2, where λ_2 is the second eigenvalue of the spatial-averaged coherency/covariance matrix

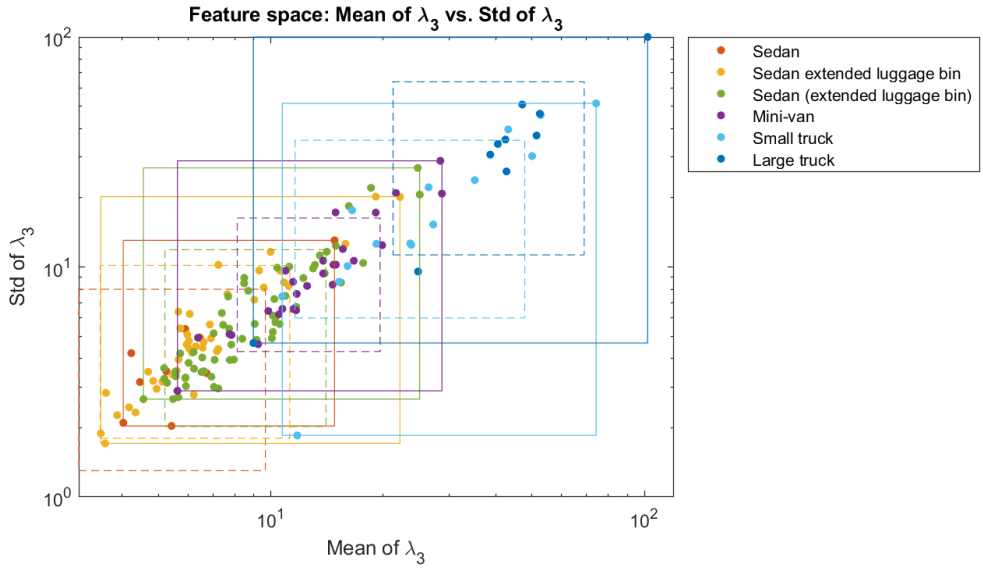

Figure D.3: Feature space of mean of λ_3 vs. standard deviation of λ_3, where λ_3 is the third eigenvalue of the spatial-averaged coherency/covariance matrix

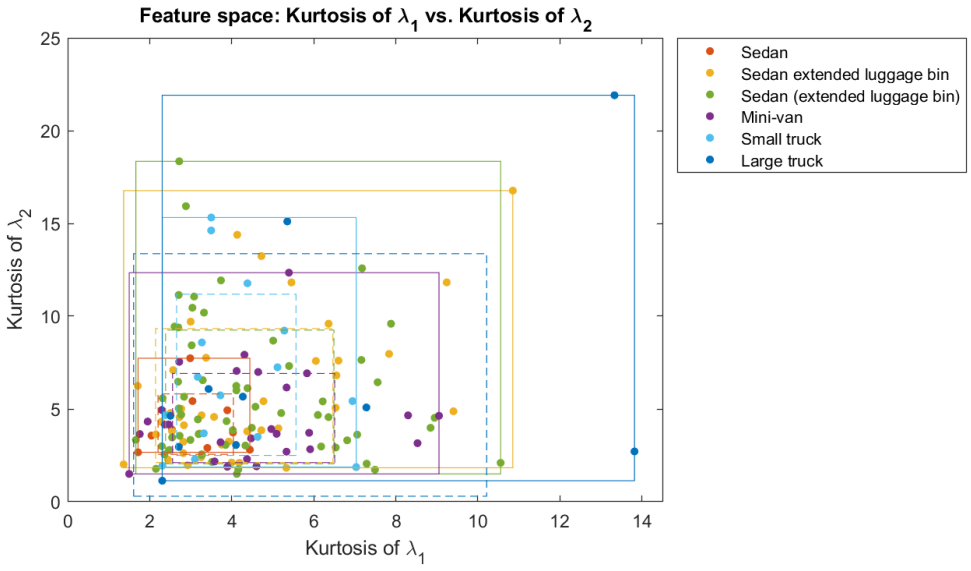

Figure D.4: Feature space of kurtosis of λ_1 vs. kurtosis of λ_2, where λ_1 and λ_2 are the first and second eigenvalues of the spatial-averaged coherency/covariance matrix

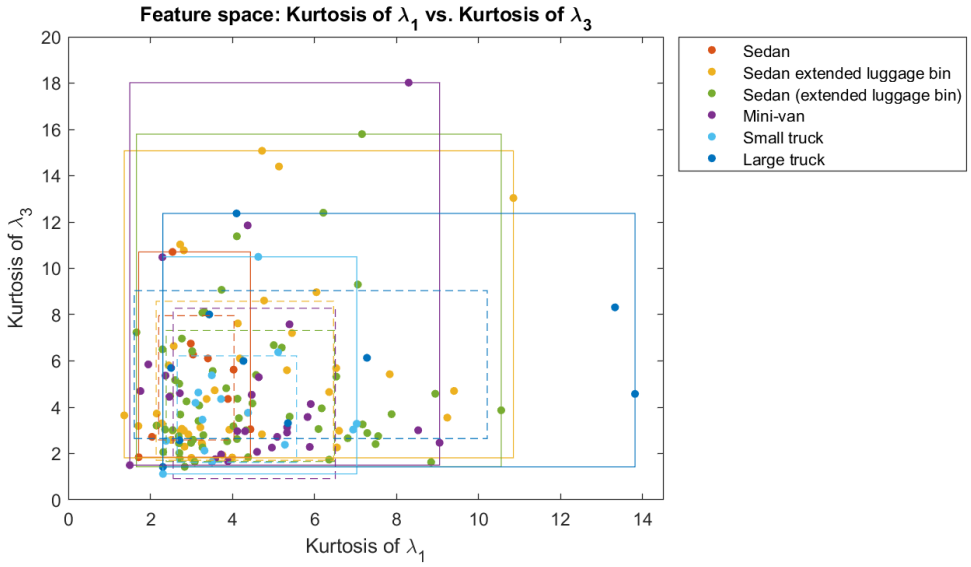

Figure D.5: Feature space of kurtosis of λ_1 vs. kurtosis of λ_3, where λ_1 and λ_3 are the first and third eigenvalues of the spatial-averaged coherency/covariance matrix

D.2. Polarization Angles of the Second Equivalent PSMs of the Spatial-Averaged Coherency Matrices

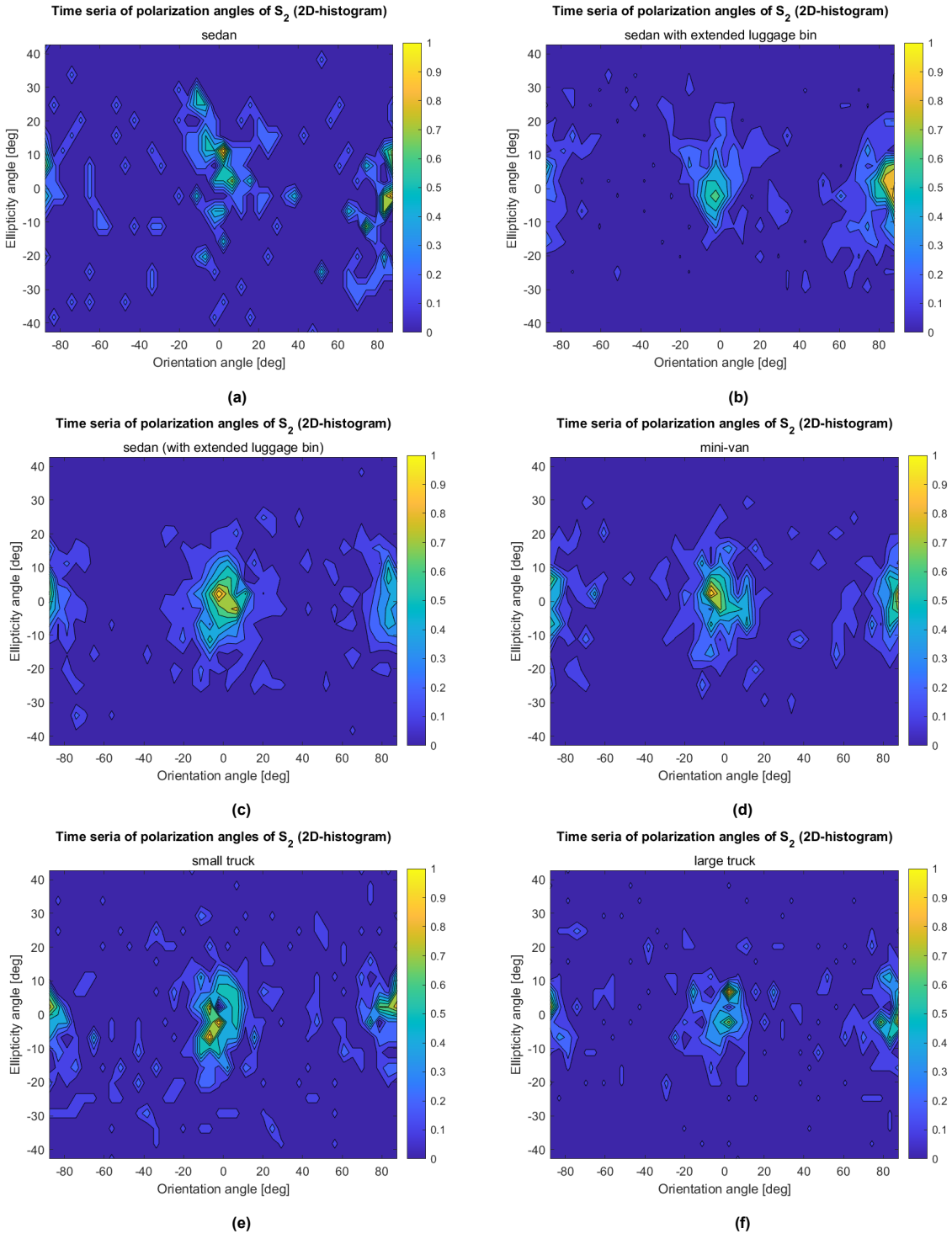

Figure D.6: 2D-histograms of the polarization angles of the second equivalent PSMs ($\mathbf{S}_2$) of all vehicle classes at all time frames, indicating horizontal, vertical orientations and linear polarizations of the vehicles' second dominant scattering mechanisms

E

Feature Summary

E.1. Feature Summary for All Vehicle Class Pairs

Table E.1: Feature summary for all vehicle class pairs, with the Silhouette coefficients in the brackets after the features

Class pair	Features
Sedan vs. Sedan extended luggage bin	Mean of λ_2 of spatial-averaged coherency/covariance matrix (0.8623)
Sedan vs. Sedan (extended luggage bin)	Mean of λ_2 of spatial-averaged coherency/covariance matrix (0.8532)
	Standard deviation of λ_2 of spatial-averaged coherency/covariance matrix (0.8132)
Sedan vs. Mini-van	Standard deviation of Re(λ_1) of centroid PSM (0.8405)
	Kurtosis of λ_1 of non-averaged coherency/covariance matrix (0.9409)
	Standard deviation of λ_1 of spatial-averaged coherency/covariance matrix (0.8159)
	Mean of λ_2 of spatial-averaged coherency/covariance matrix (0.8581)
Sedan vs. Small truck	Mean of $\lvert\lambda_1\rvert$ of centroid PSM (0.9587)
	Mean of $\lvert\lambda_2\rvert$ of centroid PSM (0.9172)
	Standard deviation of Re(λ_1) of centroid PSM (0.9845)
	Standard deviation of Im(λ_1) of centroid PSM (0.8188)
	Standard deviation of $\lvert\lambda_1\rvert$ of centroid PSM (0.9634)
	Standard deviation of Re(λ_2) of centroid PSM (0.9358)
	Standard deviation of Im(λ_2) of centroid PSM (0.9063)
	Standard deviation of $\lvert\lambda_2\rvert$ of centroid PSM (0.9447)
	Mean of λ_1 of non-averaged coherency/covariance matrix (0.987)
	Standard deviation of λ_1 of non-averaged coherency/covariance matrix (0.9847)
	Kurtosis of λ_1 of non-averaged coherency/covariance matrix (0.8251)
	Mean of λ_1 of spatial-averaged coherency/covariance matrix (0.9779)
	Standard deviation of λ_1 of spatial-averaged coherency/covariance matrix (0.9898)
	Kurtosis of λ_1 of spatial-averaged coherency/covariance matrix (0.968)
	Mean of λ_2 of spatial-averaged coherency/covariance matrix (0.9918)
	Standard deviation of λ_2 of spatial-averaged coherency/covariance matrix (0.9813)
	Kurtosis of λ_2 of spatial-averaged coherency/covariance matrix (0.9373)
Sedan vs. Large truck	Mean of $\lvert\lambda_1\rvert$ of centroid PSM (0.9883)
	Mean of $\lvert\lambda_2\rvert$ of centroid PSM (0.977)
	Standard deviation of Re(λ_1) of centroid PSM (0.9947)
	Standard deviation of Im(λ_1) of centroid PSM (0.9661)

	Standard deviation of $\|\lambda_1\|$ of centroid PSM (0.991)
	Standard deviation of Re(λ_2) of centroid PSM (0.9844)
	Standard deviation of Im(λ_2) of centroid PSM (0.971)
	Standard deviation of $\|\lambda_2\|$ of centroid PSM (0.9838)
	Mean of λ_1 of non-averaged coherency/covariance matrix (0.9979)
	Standard deviation of λ_1 of non-averaged coherency/covariance matrix (0.9979)
	Kurtosis of λ_1 of non-averaged coherency/covariance matrix (0.8443)
	Mean of λ_1 of spatial-averaged coherency/covariance matrix (0.989)
	Standard deviation of λ_1 of spatial-averaged coherency/covariance matrix (0.9968)
	Kurtosis of λ_1 of spatial-averaged coherency/covariance matrix (0.9874)
	Mean of λ_2 of spatial-averaged coherency/covariance matrix (0.997)
	Standard deviation of λ_2 of spatial-averaged coherency/covariance matrix (0.9962)
	Kurtosis of λ_2 of spatial-averaged coherency/covariance matrix (0.9848)
	Mean of λ_3 of spatial-averaged coherency/covariance matrix (0.9312)
	Standard deviation of λ_3 of spatial-averaged coherency/covariance matrix (0.882)
	Target length (0.8503)
	λ_1 of covariance matrix of detection cells (0.9351)
Sedan extended luggage bin vs. Sedan (extended luggage bin)	None
Sedan extended luggage bin vs. Mini-van	Mean of $\|\lambda_1\|$ of centroid PSM (0.829)
	Mean of λ_1 of non-averaged coherency/covariance matrix (0.881)
Sedan extended luggage bin vs. Small truck	Mean of $\|\lambda_1\|$ of centroid PSM (0.9823)
	Mean of $\|\lambda_2\|$ of centroid PSM (0.9597)
	Standard deviation of Re(λ_1) of centroid PSM (0.9739)
	Standard deviation of Im(λ_1) of centroid PSM (0.9669)
	Standard deviation of $\|\lambda_1\|$ of centroid PSM (0.9363)
	Standard deviation of Re(λ_2) of centroid PSM (0.9314)
	Standard deviation of Im(λ_2) of centroid PSM (0.9527)
	Standard deviation of $\|\lambda_2\|$ of centroid PSM (0.9355)
	Mean of λ_1 of non-averaged coherency/covariance matrix (0.992)
	Standard deviation of λ_1 of non-averaged coherency/covariance matrix (0.9843)
	Mean of λ_1 of spatial-averaged coherency/covariance matrix (0.9041)
	Standard deviation of λ_1 of spatial-averaged coherency/covariance matrix (0.9421)
	Kurtosis of λ_1 of spatial-averaged coherency/covariance matrix (0.9494)
	Mean of λ_2 of spatial-averaged coherency/covariance matrix (0.8822)
	Standard deviation of λ_2 of spatial-averaged coherency/covariance matrix (0.935)
	Kurtosis of λ_2 of spatial-averaged coherency/covariance matrix (0.8907)
	Target length (0.8865)
	λ_1 of covariance matrix of detection cells (0.8919)
Sedan extended luggage bin vs. Large truck	Mean of $\|\lambda_1\|$ of centroid PSM (0.9948)
	Mean of $\|\lambda_2\|$ of centroid PSM (0.9887)
	Standard deviation of Re(λ_1) of centroid PSM (0.9916)
	Standard deviation of Im(λ_1) of centroid PSM (0.9922)
	Standard deviation of $\|\lambda_1\|$ of centroid PSM (0.9857)
	Standard deviation of Re(λ_2) of centroid PSM (0.9838)
	Standard deviation of Im(λ_2) of centroid PSM (0.9856)
	Standard deviation of $\|\lambda_2\|$ of centroid PSM (0.9814)
	Mean of λ_1 of non-averaged coherency/covariance matrix (0.9987)
	Standard deviation of λ_1 of non-averaged coherency/covariance matrix (0.998)
	Mean of λ_1 of spatial-averaged coherency/covariance matrix (0.94)
	Standard deviation of λ_1 of spatial-averaged coherency/covariance matrix (0.9837)
	Kurtosis of λ_1 of spatial-averaged coherency/covariance matrix (0.9806)
	Mean of λ_2 of spatial-averaged coherency/covariance matrix (0.9442)
	Standard deviation of λ_2 of spatial-averaged coherency/covariance matrix (0.9883)
	Kurtosis of λ_2 of spatial-averaged coherency/covariance matrix (0.9735)
	Target length (0.9718)
	λ_1 of covariance matrix of detection cells (0.9898)
Sedan (extended luggage bin) vs. Mini-van	None

Sedan (extended luggage bin) vs. Small truck	Mean of $\lvert\lambda_1\rvert$ of centroid PSM (0.9479)
	Mean of $\lvert\lambda_2\rvert$ of centroid PSM (0.918)
	Standard deviation of Re(λ_1) of centroid PSM (0.9218)
	Standard deviation of Im(λ_1) of centroid PSM (0.9341)
	Standard deviation of $\lvert\lambda_1\rvert$ of centroid PSM (0.9192)
	Standard deviation of Re(λ_2) of centroid PSM (0.8973)
	Standard deviation of Im(λ_2) of centroid PSM (0.9335)
	Standard deviation of $\lvert\lambda_2\rvert$ of centroid PSM (0.9317)
	Mean of λ_1 of non-averaged coherency/covariance matrix (0.982)
	Standard deviation of λ_1 of non-averaged coherency/covariance matrix (0.9833)
	Mean of λ_1 of spatial-averaged coherency/covariance matrix (0.872)
	Standard deviation of λ_1 of spatial-averaged coherency/covariance matrix (0.9179)
	Kurtosis of λ_1 of spatial-averaged coherency/covariance matrix (0.9289)
	Mean of λ_2 of spatial-averaged coherency/covariance matrix (0.8852)
	Standard deviation of λ_2 of spatial-averaged coherency/covariance matrix (0.8652)
	Kurtosis of λ_2 of spatial-averaged coherency/covariance matrix (0.8518)
Sedan (extended luggage bin) vs. Large truck	Mean of $\lvert\lambda_1\rvert$ of centroid PSM (0.9862)
	Mean of $\lvert\lambda_2\rvert$ of centroid PSM (0.9786)
	Standard deviation of Re(λ_1) of centroid PSM (0.9773)
	Standard deviation of Im(λ_1) of centroid PSM (0.9863)
	Standard deviation of $\lvert\lambda_1\rvert$ of centroid PSM (0.9813)
	Standard deviation of Re(λ_2) of centroid PSM (0.9768)
	Standard deviation of Im(λ_2) of centroid PSM (0.9798)
	Standard deviation of $\lvert\lambda_2\rvert$ of centroid PSM (0.9805)
	Mean of λ_1 of non-averaged coherency/covariance matrix (0.9973)
	Standard deviation of λ_1 of non-averaged coherency/covariance matrix (0.9978)
	Mean of λ_1 of spatial-averaged coherency/covariance matrix (0.9217)
	Standard deviation of λ_1 of spatial-averaged coherency/covariance matrix (0.9724)
	Kurtosis of λ_1 of spatial-averaged coherency/covariance matrix (0.9729)
	Mean of λ_2 of spatial-averaged coherency/covariance matrix (0.9497)
	Standard deviation of λ_2 of spatial-averaged coherency/covariance matrix (0.959)
	Kurtosis of λ_2 of spatial-averaged coherency/covariance matrix (0.9593)
	Target length (0.9253)
	λ_1 of covariance matrix of detection cells (0.9804)
Mini-van vs. Small truck	Mean of $\lvert\lambda_1\rvert$ of centroid PSM (0.8187)
	Standard deviation of Re(λ_1) of centroid PSM (0.8423)
	Standard deviation of $\lvert\lambda_1\rvert$ of centroid PSM (0.836)
	Standard deviation of Re(λ_2) of centroid PSM (0.8158)
	Mean of λ_1 of non-averaged coherency/covariance matrix (0.8513)
	Standard deviation of λ_1 of non-averaged coherency/covariance matrix (0.8703)
	Mean of λ_1 of spatial-averaged coherency/covariance matrix (0.8091)
	Standard deviation of λ_1 of spatial-averaged coherency/covariance matrix (0.9018)
	Kurtosis of λ_1 of spatial-averaged coherency/covariance matrix (0.8583)
	Mean of λ_2 of spatial-averaged coherency/covariance matrix (0.9018)
	Standard deviation of λ_2 of spatial-averaged coherency/covariance matrix (0.9094)
Mini-van vs. Large truck	Mean of $\lvert\lambda_1\rvert$ of centroid PSM (0.9447)
	Mean of $\lvert\lambda_2\rvert$ of centroid PSM (0.8927)
	Standard deviation of Re(λ_1) of centroid PSM (0.9412)
	Standard deviation of Im(λ_1) of centroid PSM (0.9502)
	Standard deviation of $\lvert\lambda_1\rvert$ of centroid PSM (0.9527)
	Standard deviation of Re(λ_2) of centroid PSM (0.943)
	Standard deviation of Im(λ_2) of centroid PSM (0.8539)
	Standard deviation of $\lvert\lambda_2\rvert$ of centroid PSM (0.9293)
	Mean of λ_1 of non-averaged coherency/covariance matrix (0.9794)
	Standard deviation of λ_1 of non-averaged coherency/covariance matrix (0.9841)
	Mean of λ_1 of spatial-averaged coherency/covariance matrix (0.8913)
	Standard deviation of λ_1 of spatial-averaged coherency/covariance matrix (0.9738)
	Kurtosis of λ_1 of spatial-averaged coherency/covariance matrix (0.9454)

	Mean of λ_2 of spatial-averaged coherency/covariance matrix (0.9643)
	Standard deviation of λ_2 of spatial-averaged coherency/covariance matrix (0.9839)
	Kurtosis of λ_2 of spatial-averaged coherency/covariance matrix (0.9341)
	Target length (0.9085)
	λ_1 of covariance matrix of detection cells (0.9423)
Small truck vs. Large truck	λ_1 of covariance matrix of detection cells (0.9071)